Western Graduate&PostdoctoralStudies

Western University
Scholarship@Western

Electronic Thesis and Dissertation Repository

3-22-2017 12:00 AM

Experimental Studies of Electrical Resistivity Behavior of Cu, Zn and Co Along Their Melting Boundaries: Implications for Heat Flux at Earth's Inner Core Boundary

Innocent Chinweikpe Ezenwa, *The University of Western Ontario*

Supervisor: Richard A. Secco, *The University of Western Ontario*

A thesis submitted in partial fulfillment of the requirements for the Doctor of Philosophy degree in Geophysics

© Innocent Chinweikpe Ezenwa 2017

Follow this and additional works at: https://ir.lib.uwo.ca/etd

 Part of the Condensed Matter Physics Commons, and the Mineral Physics Commons

Recommended Citation

Ezenwa, Innocent Chinweikpe, "Experimental Studies of Electrical Resistivity Behavior of Cu, Zn and Co Along Their Melting Boundaries: Implications for Heat Flux at Earth's Inner Core Boundary" (2017). *Electronic Thesis and Dissertation Repository*. 4428.
https://ir.lib.uwo.ca/etd/4428

This Dissertation/Thesis is brought to you for free and open access by Scholarship@Western. It has been accepted for inclusion in Electronic Thesis and Dissertation Repository by an authorized administrator of Scholarship@Western. For more information, please contact wlswadmin@uwo.ca.

Abstract

The electrical resistivity of high purity Cu, Zn and Co has been measured at pressures (P) up to 5GPa and at temperatures (T) in the liquid phase. The electrical resistivity of solid state Nb was also measured up to 5GPa and ~1900K. All measurements were made in a large volume cubic anvil press. Using two thermocouples placed at opposite ends of the sample wire, serving as temperature probes as well as resistance leads, a four-wire technique resistivity measurement was employed along with a polarity switch. Post-experiment compositional analyses were carried out on an electron microprobe.

The expected resistivity decrease with P and increase with T were found in all metals in the solid state and comparisons with 1atm data are in very good agreement. The melting temperature data were obtained from the large resistivity jumps at the solid-liquid transition and these agree with other experimental studies.

The main results of this work are that resistivity of Cu decreases along its P,T-dependent melting boundary, while the resistivity of Zn and Co remain constant along their P,T-dependent melting boundaries. These findings are interpreted in terms of the competing effects of P and T on the electronic structure of filled and unfilled *d*-band liquid transition metals.

For Nb, an electronic transition was observed in the T-dependence of electrical resistivity at high P, T. The transition is discussed in terms of the effects of P and T on the electronic band structure of Nb causing a change in resistivity from behavior characterizing the ‘minus group’ to the ‘plus group’.

The electronic thermal conductivity is calculated from resistivity data using the Wiedemann-Franz law and is shown to increase with P in both the solid and liquid states for Cu, Zn and Co but upon T increase, it decreases in the solid and increases in the liquid state. For Nb,

above the transition T, the T-dependence of electronic thermal conductivity of Nb remains constant at 2GPa and exhibits an increasingly negative slope at higher P. The electronic thermal conductivity of Nb increased with increasing pressure at any given isotherm.

The implications for heat flow and thermal evolution in Earth's and other terrestrial planetary cores are based on the similarity of electronic structure of Co and Fe. The invariance of resistivity along the melting boundary of Co suggests thermal conductivity at the inner core boundary of an Fe dominated core may be similar to the value of Fe at its 1 atm melting temperature.

Keywords: Electrical resistivity, thermal conductivity, electron scattering, filled and unfilled d-bands, transition metals, pressure, temperature, melting boundary, inner-core boundary, core thermal convection, core thermal evolution.

Co- Authorship Statement

Chapter 1 is a general discussion of the geophysical motivation for this study, the background physics, and objectives. Chapters 2, 3, 4 and 5 are research studies that either have been, or are to be, submitted for publication. The individual contributions of the authors of each journal article are stated. Chapter 6 is a conclusion chapter with comparative analysis of the results contained in all the previous chapters.

Chapter 2

Chapter Title: Electrical Resistivity Measurements of Solid and Liquid Cu up to 5GPa: Decrease Along the Melting Boundary

Authors: Innocent C. Ezenwa, Richard A. Secco and Wenjun Yong.

Status: To be *submitted to Journal of Condensed Matter Physics.*

Innocent Ezenwa conducted all experimental work and performed all data analysis. The manuscript was jointly written and revised by Innocent C. Ezenwa and Richard A. Secco. Guidance for the work was provided by Richard A. Secco and Wenjun Yong.

Chapter 3

Chapter Title: Constant Electrical Resistivity of Zn on the Pressure Dependent Melting Boundary

Authors: Innocent C. Ezenwa and Richard A. Secco.

Status: *To be submitted to Journal of Applied Physics*

Innocent C. Ezenwa conducted all experimental work and performed all data analysis. The manuscript was jointly written and revised by Innocent C. Ezenwa and Richard A. Secco. Guidance for the work was provided by Richard Secco.

Chapter 4

Chapter Title: Invariance of the Electrical Resistivity of Co along the Pressure Dependent Melting Boundary

Authors: Innocent C. Ezenwa, Richard A. Secco and Wenjun Yong

Status: *To be submitted to Earth and Planetary Science Letters*

Innocent C. Ezenwa conducted all experimental work and performed all data analysis. The manuscript was jointly written and revised by Innocent C. Ezenwa and Richard A. Secco. Guidance for the work was provided by Richard A. Secco and Wenjun Yong.

Chapter 5

Chapter Title Electronic Transition in Solid Nb at High Pressure and Temperature

Authors: Innocent C. Ezenwa and Richard A. Secco.

Status: *To be submitted to Journal of Applied Physics*

Innocent C. Ezenwa conducted all experimental work and performed all data analysis. The manuscript was jointly written and revised by Innocent C. Ezenwa and Richard A. Secco. Guidance for the work was provided by Richard Secco.

Acknowledgements

I sincerely wish to thank my supervisor Prof. Richard Secco for the opportunity he gave me to pursue my academic interest. He supervised my accelerated master's project and accepted me as his Ph.D student a year later. I would not forget that moment that I indicated interest in pursuing a Ph.D degree, and he responded 'Innocent I am willing to supervise your Ph.D thesis, if you demonstrate that you have what it takes'. That moment meant a whole lot to me as I had the opportunity at my hand to be what I have always dreamed of, and it was up to me. Your teachings and guidance on how to approach academic challenges will forever be part of me and I wish I could have the opportunity to pass unto the next generation what I have learned from you. I also wish to thank Dr. Wenjun Yong and Jonathan Jacobs for all the support with the experimental challenges, design, making parts and carrying out the experiments. Thanks to my supervisory committee members Prof. Sean Shieh and Prof. Robert Shcherbakov for all their advice and suggestions. Thanks to my co–students Timothy Officer, Reynold Sukara, Joshua Littleton and Ryan Sawyer for useful interactions.

I cannot thank enough the love of my life, Nkemdilim Cynthia Ezenwa and my daughter, Solumtochi Nicole Ezenwa for all their love, financial, emotional and psychological support. Without you both, there will be no me. You are my world. I sincerely wish to thank my parents Chief. Augustine (Snr) Ezenwa and Lolo Mrs. Cecilia Nneka Ezenwa who raised me with a love of science and supported me in all my pursuit. I would also like to thank my parent in-law Chief. Prof. David Nwoye Eze and Lolo Dr. (Mrs) Virginia Obioma Eze for all the love and encouragement.

Last but most special, I would like to thank my siblings, amongst Hillary Chika Ezenwa. Your charitable and sacrificial character which you have demonstrated towards me and my siblings

is a source of inspiration to me. Your unconditional love is unquestionable and you set the stage for me and my younger ones to get the best possible education.

Table of Contents

List of Figures

List of appendix

List of symbols

A – Area

BZ – Brillouin Zone

I – Current

CMB – Core-mantle boundary

dHvA – de Hass van Alphen effect

ρ - Electrical resistivity

k_e - Electronic thermal conductivity

fcc – Face centered cubic

E_f - Fermi energy

γ - Gruneisen parameter

Q – Heat flux

hcp – hexagonal close packed

ICB – Inner-core boundary

K_T – Isothermal bulk modulus

l – length

L – Lorenz function

MNFE – Modified nearly free electron theory

NFE – Nearly free electron theory

k_p - Phonon thermal conductivity

P – Pressure

R – Resistance

E_{fd} - Separation of d-band position relative to Fermi level

I – Stoner parameter

S – Thermoelectric power

T - Temperature

k_{total} – Total thermal conductivity

V – Voltage Drop

Chapter 1: Introduction

1.0 General Introduction

Earth's internal heat powers most geological processes that shape the physical make-up of the planet [1, 2]. Primordial heat and continuing decay of radionuclides are the two main sources of heat energy in the Earth's interior. Generally, conduction is a slow and less effective means of heat transport than convection. In the rigid crust and lithosphere where convection cannot take place, conduction is the dominant mode of heat transport. On the other hand, convection dominates in the fluid outer core, and also plays a dominant role in the heat flow through the mantle. However, conduction cannot be completely neglected in the outer core since it is metallic in composition and hence a good conductor [3]. A significant amount of heat is conducted from the outer core, of composition predominantly Fe with light elements, to the overlying mantle along the adiabatic temperature (T) gradient. Solidification and growth of the inner core separates the mainly Fe from the outer core liquid Fe alloy leaving behind a less dense Fe alloy in the outer core. The exsolution of light elements by these processes generates a compositionally driven convection. Thermal and compositional convection in the outer core provide the energy to drive the geomagnetic field, with compositional convection thought to be the more dominant contribution [4].

The electrical and thermal conductivity of the Earth's core are both material properties and the fundamental understanding of these properties is paramount in the modelling of Earth's thermal history as well as, generation and sustainability of the Earth's magnetic field. The inner core boundary (ICB) is the solidification point of dominantly Fe composition, thus knowledge of the electrical resistivity and thermal conductivity of Fe on its melting boundary could provide an anchoring point for the Earth's core.

1.1 Core Heat Flow: Geodynamo and Inner Core Age

The understanding of the origin of the Earth's magnetic field was for a long time a major problem in planetary physics. Although the morphology of Earth's magnetic field resembles that of a permanent bar magnet, the fluid motion in the outer core, which is at T of 4000-5000 K [1, 5, 6] and pressure (P) of 135-330 GPa [7] is not conducive to produce and support a permanent magnetization [3]. In addition, field polarity reversals through time do not support a permanent magnetism. The flow of conducting metal in a magnetic field was first suggested by Larmor [8] to be responsible for the self-exciting dynamo of the solar magnetic field. Over decades of attempting to establish a working model of a geodynamo, Bullard and Gellman [9] showed the possibility of a homogenous fluid acting as a self-exciting dynamo, based on solutions of Maxwell's equations for a sphere of electrically conducting fluid with specified velocities. Simulations in this model driven by thermal buoyancy showed chaotic behavior and field flipping, as is the case in the geological record, leading to the suggestion that it can account for the origin of the Earth's magnetic field. However, later studies [10, 11] demonstrated that a three-dimensional magnetic field driven with a prescribed three-dimensional velocity profile would not give a self-consistent convective solution with nonlinear feedback. The magneto-convection simulations in three-dimensions, which are closer to self-consistency due to the time dependent thermodynamics, velocity and magnetic fields, were solved in three-dimensions with nonlinear feedback [10]. With this approach, a fully self-consistent three-dimensional numerical simulation of a convective strong-field dynamo in a spherical shell with a finitely conducting inner core [10] produced the first self-consistent dynamo solution which undergoes several polarity excursions and a dipole moment reversal with features similar to real reversals of the geomagnetic field of the Earth.

A prevalent model of core formation is known as the 'deep magma ocean' model [12]. According to the model, accretion processes and decay of short-lived radionuclides acted as sources of heat which were sufficient to create an extensive molten outer layer; a magma ocean. The metallic components arriving from accreting bodies separated and sank through the magma ocean as small droplets approximately 1cm in diameter. The droplets descended through a completely molten, or low-viscous state silicates and oxides which formed a thick shell called the mantle. Molten metallic droplets accumulated forming a 'metal pond'. The dense metal-pond layer accumulated until it reached a sufficient thickness that was gravitationally unstable which resulted in large metal diapirs, approximately 100km in diameter, descending and segregating to form the core [12-14]. Then as P increased along with the radius of the growing Earth, the inner core began to solidify radially outwards from the center of the Earth due to the P-dependence of this phase change in a cooling core. The exsolution of lighter elements due to solidification and growth of the inner core releases latent heat that provides energy to power the dynamo. The freezing of nearly-pure Fe onto the growing inner core leaves behind a less dense fluid of Fe plus light alloying elements in the outer core. Chemical buoyancy driven by the exsolution brings about chemical convection that exceeds thermal convection in generating and sustaining the Earth's magnetic field [15].

Experimental analysis of the cooling of the Earth's interior materials suggested core thermal conductivity values of $63 Wm^{-1}K^{-1}$ at the ICB and $46 Wm^{-1}K^{-1}$ at the underside of the core mantle boundary (CMB) [16]. Later experimental analysis suggested a lower value of 28-29$Wm^{-1}K^{-1}$ for the core, almost uniform throughout the core [17]. However, more recent studies [18, 19] have suggested much higher values of about $90 Wm^{-1}K^{-1}$. Solidification and growth of the inner core relates to core heat flow through time-dependent reduction in the P at which the geotherm of

the core intercepts the melting curve of the outer core composition. If too little heat flows from the core to the mantle, the geodynamo does not operate. Higher thermal conductivity means that the inner core formed much later than was thought. Global thermodynamic calculations [20, 21] suggested that the inner core is relatively young, around 1Ga. A young inner core poses a challenge due to the general consensus that freezing of the core powers the geodynamo [22] via compositional convection. If there is no inner core, then no magnetic field should be produced. Yet there is evidence from paleomagnetic studies that show the magnetic field has been around for most of the Earth's history ~3.5Ga [23].

Without the contribution of compositional convection, a core-mantle boundary heat flow of ~10TW is needed for the whole of Earth's magnetic history to produce a comparable dynamo of the present field via thermal convection alone [18]. Radioactive heating could provide this greater heat flow if radionuclides (U, Th, K) are present in the outer core in sufficient amounts. Nonetheless, such a high heat flow would also affect the mantle, melting it earlier in the Earth's history with consequences for mantle geochemistry and possibly for the heat budget of the Earth as a whole [24]. Understanding how the geodynamo worked before the inner core formed is now a priority [25] which makes mapping of heat flux from the inner core boundary to the core-mantle mantle boundary and accurate determination of the age of the inner core highly important.

1.2 Thermal Conductivity

There exist only few data on the direct measurement of total thermal conductivity (k_{total}) of metals at high P and T conditions and these are very recent measurements on liquid Pt by McWilliams et al. [26] and on solid Fe by Konôpková et al. [27]. This is primarily due to the challenges of maintaining a small T gradient (dT/dr) at high T required in the measurement of k_{total} as described in the heat conduction equation, $Q = k_{total}\,(dT/dr)$, where Q is the total heat flux. The

measurement of k_{total} becomes more challenging in the case of liquid metals where chemical convection and possible chemical contamination by a sample container is highly possible. At high pressures, the challenges are compounded. Hence, indirect measurement and/or other methods of determination of the thermal conductivity at these conditions are desirable. The two components of k_{total} in a metal are the electrons and phonons. Electrons in a metal are not bound to the atoms and are thus free to move. As the delocalized electrons propagate, they carry along heat energy. Thus, metals are generally good electrical and heat conductors. At high T, phonons are not effective in transporting heat, as atomic vibration increases with increasing T, the transfer of heat energy between adjacent neighbouring atoms become less effective due to scattering from lattice vibrations (phonon scattering). Electronic thermal conductivity (k_e) contribution to the k_{total} dominates over the contribution by the phonons at high T above Debye T. Fortunately, the electrical resistivity is related to k_e through the Wiedemann-Franz law [28], $k_e = \frac{LT}{\rho}$ where L is the Lorenz number, and ρ is electrical resistivity. Therefore, by measuring the electrical resistivity of a pure metal at any P and T conditions, to the extent that the electronic thermal conductivity is the dominant component of the total thermal conductivity, k_e can be calculated using a selected value of L.

1.3 Electron Scattering in Liquid Metals

The scattering of conduction electrons in liquid transition metals largely depend on the extent to which their *d*-bands are filled. Two parallel models by Mott and Ziman provide the theoretical explanation for the liquid resistivity of transition metals.

1.3.1 Mott's Theory

An approach to the theory of liquid resistivity of transition metals by Mott [29] considered that on melting of a crystalline solid, the arrangement of the atoms relative to one another would not change much on melting. The atoms of liquid transition metals were assumed to vibrate about their mean position which remained fixed, as in the crystal. Suggestion was made that in normal metals (metals with filled *d*-band), the change in resistivity on melting is due mainly to the change in frequency of atomic vibration. A later electron scattering theory in a crystal was developed by Mott which was considered valid for both solid and liquid metals [30, 31]. In this model, the mobile conduction *s* electrons can undergo both *s*-*s* and *s*-*d* scattering processes depending of the occupancy of the *d*-band. For the filled *d*-band metals, the only scattering processes present is *s*-*s* while conduction electrons in unfilled *d*-band metals can be scattered by *s*-*s* and *s*-*d* processes. Due to the high density of states of the *d*-band and owing to the lower mobility (because of higher effective mass) of the *d* electrons relative to the *s* electrons, unfilled *d*-band metals are generally more resistive than filled *d*-band metals. In this model, both the *s* and *d* electrons contribute to conduction but with higher mobility and longer mean free path, the *s* electron contribution is dominant. This model was successful in explaining the resistivity of solid state transition metals and their increment from left to the right of the period table which correlates with the increasing occupancy of electrons in *d*-band.

However, Ziman [32] argued that neglecting the contribution of atomic disorder in the liquid resistivity on melting will lead to resistivity which would be proportional to T which is not found. He demonstrated that Mott's theory is not valid for metals with a large pseudo-potential on melting.

1.3.2 Ziman's Theory

In Ziman's model, the liquid electrical resistivity was studied on the basis that each ion acts upon the conduction electrons through a localized pseudo-potential. For the filled *d*-band metals, only the *s* electrons contribute to conduction. The conduction electrons are nearly "free" and the total effect of the assembly of ions in the liquid can be evaluated through perturbation theory by taking the integral effects of all the localized ions. Ziman's model is usually called the nearly free electron (NFE) model. The relative change in the electrical resistivity during melting is caused by the change in the radial distribution function of the ions. The differences in the resistivity at the solid-liquid transition of metals are caused by the differences in the scattering cross sections of their ions, especially their differences in the ion core. T variation of resistivity in the liquid state follows from the T-dependent Fourier transform of the radial distribution function of the liquid ions. The NFE model has accounted very well for the electrical resistivity of a filled *d*-band liquid transition metal like Cu and even in the case of Zn with a complicated electronic structure.

However, the NFE model could not on its own account for the liquid electrical resistivity of unfilled *d*-band metals. The electrical resistivity of the unfilled *d*-band metals in the liquid state was accounted for by the modified nearly free electron (MNFE) [33-35] which took into account an additional scattering to the conduction *s*-electrons through *d*-resonance scattering. Although the conduction electrons are *s*-electrons, the *d*-electrons influence the *s*-electrons because of the presence of the *d*-resonance site. An *s*-conduction electron in the neighbourhood of the *d*-resonance site experiences a delay in its movement [34, 35], thus increase resistivity. The MNFE model of describing electrical resistivity of liquid transition metals with un-filled *d*-bands is accepted today.

1.4 Stacey and Anderson (2001) Hypothesis

Stacey and Anderson [16] postulated that the scattering of conduction electrons in a metal by the thermal vibration of atoms varies with P and T in such a way that the electrical resistivity remains constant along the P,T-dependent melting boundary. Their discussion was based on the compensating effects of P and T on the electrical resistivity of filled *d*-band simple metals, such as Cu and Zn, but they extended it to include unfilled *d*-band metals, such as Fe, Co, and Ni. This theory indicated that in the ferromagnetic state of Fe, conduction electrons is due to both *4s* and *3d* electrons but the *4s* electrons dominate over the *3d* electrons because of their higher mobility. However, above the Curie T, the spontaneous disappearance of the alignments of *3d* electron spins, suggests that the relative mobility of *3d* and *4s* electrons do not change significantly and hence the electrical resistivity of Fe behave as if only *4s* electrons contribute to conductivity, as is the case in metals with a filled *3d*-band. Using the sparse high P,T experimental data available on electrical resistivity, from Bridgman [36] and Matassov [37], Stacey and Anderson tested and found their postulate valid on solid Fe.

1.4.1 P, T Effect on the Electrical Resistivity on the Melting Boundary: Stacey and Anderson Perspective.

Stacey and Anderson considered that in a filled *d*-band metal where the entire conduction electron states (i.e. those states whose energy range is within the order *kT* of the Fermi level) are of the same kind, a P-induced increase in resistivity caused by a decrease in available density states of conduction electrons with increasing P, is counteracted by a decrease in resistivity due to a decrease in amplitude of lattice induced scattering. While a T-induced decrease in resistivity caused by thermal excitation of more *s* electrons into the conduction band states, is compensated by increase in resistivity due to increase in lattice induced scattering on melting. These antagonistic

effects on resistivity result in an overall effect of constant electrical resistivity along the P, T-dependent melting boundary. This cancelling effect of P and T on the electrical resistivity was considered valid for both filled and unfilled *d*-band metals since *d* and *s* electron mobilities are unchanged above the Curie T as discussed previously.

1.5 Stacey and Loper (2007) Revised-Hypothesis

Stacey and Loper [17] was prompted to re-examine Stacey and Anderson's [16] theory, following the high pressure shock-wave experimental investigation by Bi et al. [38] using a single crystal sapphire cell in the encapsulation of Fe in the electrical resistivity measurement. The measured electrical resistivity value reported by Bi and co-workers was much higher than the value measured by Matassov [37] due to the shunting of Fe sample by epoxy capsule used by Matassov. In this revised theory, Stacey and Loper argued that the invariance in electrical resistivity along the melting boundary can only be applied to electronically simple metals: those metals that have filled *3d*-bands such as Cu and Zn, but not valid for metals with an unfilled *3d*- band (e.g. Fe, Co and Ni).

1.5.1 P, T Effect on the Electrical Resistivity of Unfilled d-band Metals on the Melting Boundary: Stacey and Loper Perspective.

Stacey and Loper considered in this new theory that even above the Curie T, for the case of unfilled *d*-band metals whose conduction electrons are in two types of states (*3d* and *4s* in the case of Fe) at the Fermi level, both states contribute to conduction with different mobilities. Because the *d* electrons are less mobile than the *s* electrons and the *d* band is unfilled, the phonon-induced excitation of *4s* electrons has the probability of being scattered into less mobile unfilled *d* band states and thus increases resistivity. From the analysis made by Stacey and Loper, the number of electrons contributing to conduction is proportional to the density of *4s* states but the probability

of scattering is proportional to the higher density of *3d* states. With increasing P, the changes in density of states of *3d* and *4s* bands are different. Because of less overlap of *3d* bands, their density decreases much less than the *4s* bands with increasing P. They considered this uncompensated effect of P to result in higher resistivity not accounted for in Stacey and Anderson theory. Thus, the implication of this additional resistivity is that the resistivity of Fe will not be constant along the P, T-dependent melting boundary.

1.6 Critical Role of *d*-Band in Transition Metal Melting Behavior

Interestingly, experimental investigations of the systematism of the melting behavior of transition metal groups [39, 40] have also highlighted the roles played by the filled and unfilled states of the *d*-band electrons. Results showed that the slope of the melting T with P of polyvalent metals without *d*-electrons is higher than transition metals, owing to the role of *d*-electrons. The melting experiments investigated by Japel et al. [41] showed that Cu and Ni exhibit different melting slopes over a large P range, up to 97GPa, owing to the filled and unfilled *d*-band states respectively. Their measurements showed the melting slope of Cu was ~2.5 times steeper than that of Ni. From these results, they suggested that testing the validity of ab-initio results on melting of Fe should be made with another transition metal and not with a metal such as Al which does not have *d* states. Clearly, the state of occupancy of the *d*-band in metals has important effects on basic physical behavior, such as melting, and on basic physical properties, such as electrical resistivity.

1.7 Objective of this Study

The objective of this study is to test the validity of the proposed invariance and variance of electrical resistivity along the P and T-dependent melting boundary, of filled and unfilled *d*-band metals respectively. Cu and Zn both have filled *3d*-band states in their electronic configuration and

were selected to test for the case of invariance. Co has an unfilled *3d*-band and was selected as a contrast.

1.7.1 Filled *d*-band Metals: Cu [Ar]$3d^{10}4s^1$ and Zn [Ar]$3d^{10}4s^2$

The electronic structures of Cu and Zn have been extensively studied. While Cu and Zn have in common a filled *3d* band, their Fermi surfaces are considerably different. The Fermi surface of Cu is contained within the first Brillouin Zone (BZ) with neck features making contact with the BZ boundary. On the other hand, the Fermi surface of Zn spans across the first BZ and extends up to third to fourth BZ. The expansion of the Fermi surface of Zn beyond the first BZ, while that of Cu is within the first BZ makes for an interesting feature to explore in the investigation of the P-dependent electrical resistivity of these filled *3d*-band metals. In addition, Cu melts from a face centered cubic (fcc) phase while Zn melts from an hexagonal closed packed (hcp) phase.

1.7.2 Unfilled *d*-band Metal: Co [Ar]$3d^7 4s^2$

The electronic structure of Co is described differently than that of Cu and Zn due to spin-orbit splitting effects. The unfilled *3d*-band state of Co thus provides a good contrast to the filled *3d*-band states of Cu and Zn since the upper sub-band of Co is Cu like. In addition, Co is a close analog to Fe and Ni with a similar band structure. The upper spin band of Fe, Co and Ni are similar to those of the noble metals while the lower spin bands are Mo-like for Fe, Re-like for Co and W-like for Ni. The understanding of the electrical resistivity of Co along its melting boundary should give insight to the behavior of Fe which possesses greater experimental challenges due to its higher melting T. The behavior of Fe has significant geophysical implication due to its dominant composition in the core.

1.7.3 Nb [Kr]$4d^4 5s^1$

The understanding of the electrical behaviour of the paramagnetic metals is also important in this study because of their unfilled *d*-band states and because they exhibit magnetic characteristics though lower in strength than Fe, Co and Ni. However, their study in the liquid state has been hampered by the very high melting T of these metals. The study of the electrical resistivity of these metals at high P and T conditions is important in understanding the individual contribution or participation of the sub-bands in ferromagnetic metals. Each chapter in this thesis is a discussion on the individual elements of Cu, Zn, Co and Nb.

1.8 References

[1] Buffett, B. A. (2007). Taking Earth's temperature. *Science*, *315*(5820), 1801-1802.

[2] Turcotte, D. L., and Schubert, G. (2002). Geodynamics. *Cambridge University Press*, New York.

[3] Lowrie, W. (2007) Fundamentals of geophysics. *Cambridge University Pres*s, New York.

[4] Buffett, B. A. (2000). Earth's core and the geodynamo. *Science*, *288*(5473), 2007-2012.

[5] Gilvarry, J. J. (1957). Temperatures in the Earth's interior. *Journal of Atmospheric and Terrestrial Physics*, *10*(2), 84-95.

[6] Boehler, R. (1996). Melting temperature of the Earth's mantle and core: Earth's thermal structure. *Annual Review of Earth and Planetary Sciences*, *24*(1), 15-40.

[7] Jeanloz, R. (1990). The nature of the Earth's core. *Annual Review of Earth and Planetary Sciences*, 18, 357-386.

[8] Larmor, J. (1919). How could a rotating body such as the Sun become a magnet. *Rep. Brit. Assoc. Adv. Sci*, 159, 412.

[9] Bullard, E., and Gellman, H. (1954). Homogeneous dynamos and terrestrial magnetism. *Philosophical Transactions of the Royal Society of London A: Mathematical, Physical and Engineering Sciences*, 247(928), 213-278.

[10] Glatzmaier, G. A., and Roberts, P. H. (1995). A three-dimensional self-consistent computer simulation of a geomagnetic field reversal. *Nature* Vol 377, 203-209.

[11] Kageyama, A., Miyagoshi, T., and Sato, T. (2008). Formation of current coils in geodynamo simulations. *Nature*, *454*(7208), 1106-1109.

[12] Wood, B. (2011). The formation and differentiation of Earth. *Physics Today*, *64*(12), 40-45.

[13] Halliday, A. N., and Wood, B. J. (2010). The composition and major reservoirs of the Earth around the time of the Moon-forming giant impact. *Treatise on geophysics*, *9*, 13-50.

[14] Rudge, J. F., Kleine, T., and Bourdon, B. (2010). Broad bounds on Earth's accretion and core formation constrained by geochemical models. *Nature Geoscience*, *3*(6), 439-443.

[15] Pozzo, M., Davies, C., Gubbins, D. and Alfè, D. (2013). Transport properties for liquid silicon-oxygen-iron mixtures at Earth's core conditions. *Physical Review B, **87**: 014110.*

[16] Stacey, F. D., and Anderson, O. L. (2001). Electrical and thermal conductivities of Fe–Ni–Si alloy under core conditions. *Physics of the Earth and Planetary Interiors*, *124*(3), 153-162.

[17] Stacey, F. D., and Loper, D. E. (2007). A revised estimate of the conductivity of iron alloy at high pressure and implications for the core energy balance. *Physics of the Earth and Planetary Interiors*, *161*(1), 13-18.

[18] Gomi, H., Ohta, K., Hirose, K., Labrosse, S., Caracas, R., Verstraete, M. J., and Hernlund, J. W. (2013). The high conductivity of iron and thermal evolution of the Earth's core. *Physics of the Earth and Planetary Interiors*, *224*, 88-103.

[19] Pozzo, M., Davies, C., Gubbins, D., and Alfè, D. (2014). Thermal and electrical conductivity of solid iron and iron–silicon mixtures at Earth's core conditions. *Earth and Planetary Science Letters*, *393*, 159-164.

[20] Labrosse, S., Poirier, J. P., and Le Mouël, J. L. (2001). The age of the inner core. *Earth and Planetary Science Letters*, *190*(3), 111-123.

[21] Labrosse, S. (2003). Thermal and magnetic evolution of the Earth's core. *Physics of the Earth and Planetary Interiors*, *140*(1), 127-143.

[22] Davies, C. (2015). The inner core conundrum. *High-Energy Astrophysics*, 36.

[23] Biggin, A. J., de Wit, M. J., Langereis, C. G., Zegers, T. E., Voûte, S., Dekkers, M. J., and Drost, K. (2011). Palaeomagnetism of Archaean rocks of the Onverwacht Group, Barberton Greenstone Belt (southern Africa): Evidence for a stable and potentially

reversing geomagnetic field at ca. 3.5 Ga. *Earth and Planetary Science Letters*, *302*(3), 314-328.

[24] Labrosse, S., Hernlund, J. W., and Coltice, N. (2007). A crystallizing dense magma ocean at the base of the Earth's mantle. *Nature*, *450*(7171), 866-869.

[25] Constable, C.G, T.G. Masters, B. Buffett, J.M.D. Day, M. Hirschmann, S-I. Karato, L. Kellogg, M. Long, and W. Mao, (2016) Cooperative Studies of the Earth's Deep Interior: Understanding the origin and evolution of our planet through interdisciplinary research, available from csedi.org/2016_Report.

[26] McWilliams, R. S., Konôpková, Z., and Goncharov, A. F. (2015). A flash heating method for measuring thermal conductivity at high pressure and temperature: Application to Pt. *Physics of the Earth and Planetary Interiors*, *247*, 17-26.

[27] Konôpková, Z., McWilliams, R. S., Gómez-Pérez, N., and Goncharov, A. F. (2016). Direct measurement of thermal conductivity in solid iron at planetary core conditions. *Nature*, *534*(7605), 99-101.

[28] Franz, R., and Wiedemann, G. (1853). Ueber die wärme-leitungsfähigkeit der metalle. *Annalen Der Physik*, *165*(8), 497-531.

[29] Mott, N. F. (1934). The resistance of liquid metals. *Proceedings of the Royal Society of London. Series A, Containing Papers of a Mathematical and Physical Character*, *146*(857), 465-472.

[30] Mott, N. F. (1936). The electrical conductivity of transition metals. In *Proceedings of the Royal Society of London A: Mathematical, Physical and Engineering Sciences* (Vol. 153, No. 880, pp. 699-717).

[31] Mott, N. F. (1972). The electrical resistivity of liquid transition metals. *Philosophical Magazine*, 26(6), 1249-1261.

[32] Ziman, J. M. (1961). A theory of the electrical properties of liquid metals. I: The monovalent metals. *Philosophical Magazine*, *6*(68), 1013-1034.

[33] Evans, R., Greenwood, D. A., and Lloyd, P. (1971). Calculations of the transport properties of liquid transition metals. *Physics Letters A*, 35(2), 57-58.

[34] Gaspari, G. D., and Gyorffy, B. L. (1972). Electron-phonon interactions, d resonances, and superconductivity in transition metals. *Physical Review Letters*, 28(13), 801.

[35] Shvets, V. T. (1982). Influence of sd hybridization of the electrical conductivity of liquid transition metals. *Theoretical and Mathematical Physics*, 53(1), 1040-1046.

[36] Bridgman, P. W. (1957). Effects of Pressure on Binary Alloys V Fifteen Alloys of Metals of Moderately High Melting Point. In *Proceedings of the American Academy of Arts and Sciences* (Vol. 84, No. 2, pp. 131-177). American Academy of Arts and Sciences.

[37] Matassov, G. (1977). The electrical conductivity of iron-silicon alloys at high pressures and the earth's core *(Doctoral dissertation, University of California, Davis.).*

[38] Bi, Y., Tan, H., and Jing, F. (2002). Electrical conductivity of iron under shock compression up to 200 GPa. *Journal of Physics: Condensed Matter*, *14*(44), 10849.

[39] Ross, M., Yang, L. H., and Boehler, R. (2004). Melting of aluminum, molybdenum, and the light actinides. *Physical Review B*, *70*(18), 184112.

[40] Errandonea, D., Schwager, B., Ditz, R., Gessmann, C., Boehler, R., and Ross, M. (2001). Systematics of transition-metal melting. *Physical Review B*, *63*(13), 132104.

[41] Japel, S., Schwager, B., Boehler, R., and Ross, M. (2005). Melting of copper and nickel at high pressure: The role of d electrons. *Physical Review Letters*, *95*(16), 167801.

Chapter 2: Electrical Resistivity Measurements of Solid and Liquid Cu up to 5GPa: Decrease Along the Melting Boundary

2.0 Introduction

Electrical resistivity and thermal conductivity of metals characterize the nature of electron-phonon and electron-electron interaction as well as the phase state of a system. The effects of pressure (P) and temperature (T) on the electrical resistivity of a metal are usually antagonistic – resistivity decreases with P and increases with T. Combinations of P and T that offset each other to maintain constant resistivity can be found if the P- and T-coefficients of resistivity are known. A thermodynamically-based treatment of the effects of P and T on simple and other metals proposes that the electrical resistivity is constant on the P, T-dependent melting boundary [1, 2]. If validated experimentally for the case of Fe, it would provide an elegant route to evaluating the electrical resistivity of a metal at very high P,T on its melting boundary by measuring the resistivity on the melting boundary at lower P,T. The present study provides an experimental assessment of this proposal using Cu as a test simple metal.

The theory of electrical resistivity of transition metals in the solid state is generally understood in the context of *s-d* scattering [3]. In metals, valence electrons are delocalised and are distributed over a range of energy bands. At T above 0K, thermal vibrations of the lattice reduce the mean free path of an electron by increasing the probability of phonon-electron scattering. Although the resistivity of a metal is approximately proportional to the absolute T above the Debye T, as predicted by Bloch theory, there are deviations at very high T due to thermal expansion. With

increasing P, the amplitude of lattice vibration and thus phonon scattering is reduced, as a consequence of volume reduction, hence causing an increase in the mean free path of the electrons and lower resistivity.

The nearly free electron (NFE) model of Ziman's theory [4] has accounted very well for the electrical resistivity of a simple liquid metal like Cu. The transport coefficients in this theory depend on two main factors, namely, the electron ion pseudopotential matrix element, which describes electron-ion core scattering, and the dynamical structural factor of the ion system. Provided an appropriate electron-ion pseudopotential is used in the NFE model, the electrical resistivity of liquid transition metals can be well described. However, Mott [5] suggested that for pure liquid transition metals, a different model that is similar to the *s*-*d* transition model used in his solid state theory is appropriate but with different mean free paths for the *s*-*p* and *d* electrons. Other theoretical studies of electron scattering in liquid transition metals [6-10] have focused on a transition-matrix term in addition to the electron ion pseudopotential in the Ziman formula [4].

For Cu with filled *3d*-band states and with an electronic configuration of $[Ar]3d^{10}4s^{1}$, the only electron-electron scattering present is *s*-*s* scattering, while the conduction *s* electrons of those metals with an unfilled *d*-band can undergo both *s*-*s* and *s*-*d* scattering processes. Electron mobility in the *s*-band is greater than in the *d*-band, thus, metals with filled *d*-bands are generally more conductive than those with unfilled *d*-bands. In a solid crystal, the wave function of the electrons outside the ion core is not a single plane wave but it is rather tailored to the lattice by coherent diffraction. The electron density within the lattice forms a pattern having the same period as that of the lattice. The delocalised conduction electrons in a metal are subjected to this periodic electron density and hence encounter scattering from it similar to that caused by the pseudopotential of the ion cores [11]. However, in the liquid state, the electron gas is best described outside the ion cores

by simple plane waves that are randomly phased and isotropically propagated in a short range ordered structure [11]. In Cu, the filled *d*-band overlaps the bottom of the *s*-band and hence influences the conduction *s* electrons by shielding them from the influence of the nucleus [12, 13] and simultaneously contributes to the periodic electron density of the crystal system.

The interpretation of P effects on the electronic transport of metals generally requires an understanding of the way in which P affects the Fermi surface. The notion that the Fermi surface of solid Cu may touch the Brillouin Zone (BZ) boundary was confirmed by a study of the anomalous skin effect [14]. The energy function changes near the zone boundaries and thus, the Fermi velocity of the conduction electrons are expected to be lower than its free electron value at the zone boundaries [12]. When a metal is compressed, the volume of the BZ in reciprocal space, and with it the volume enclosed by the Fermi surface, increases. A change in the dimensions of the BZ causes size and topological changes in the Fermi surface of a metal with a non-isotropic compressible crystal structure. Nonetheless, for a cubic crystal like Cu which should compress isotropically, a change in the size of the BZ ideally should cause no topological change in the Fermi surface [15]. The effect of low hydrostatic P on the Fermi surface of solid Cu has been experimentally studied [15, 16] by observing the phase change in de Haas van Alphen (dHvA) oscillations in the P range of 0.0001 – 0.0025 GPa at 1K and theoretically [17] using ab initio linear muffin-tin orbital method in the atomic sphere approximation. From the rigid-sphere model of liquid metals [18, 19], the Fermi surface of many liquid metals is spherical and of volume sufficient to accommodate all the valence electrons. A study on the change of separation of the *d*-band (upper and lower d-bands) position relative to the Fermi level (E_{Fd}) of Cu up to 1.2GPa at room T, by observing the P-dependent shift in the reflectivity edge [20], demonstrated an increasing E_{Fd} with increasing P. Since the upper *d*-band is radially symmetric [13], the onset of

separation occurs simultaneously over the entire Fermi surface. However, T-dependent investigation of the optical properties of liquid Cu at 1 atm by the polarimetric method [21] demonstrated that the *d*-band is unbroadened and unshifted relative to the Fermi level by the process of melting. This suggests that the null effect of T on E_{Fd} at the melting boundary may not compensate for the P-induced increase of E_{Fd} in Cu.

The T-dependence of electrical resistivity of solid and liquid Cu at 1atm as reported by many different authors has been compiled by Matula [22]. The P-dependence of electrical resistivity of solid Cu has been studied by both shock wave [23-26] and static [27] P techniques. In order to investigate further the effects of P and T on the electrical resistivity of Cu, particularly in the liquid state, and to test experimentally the thermodynamics-based prediction of constant resistivity on the P-dependent melting boundary [1,2], the electrical resistivity of solid and liquid Cu up to 5GPa and ~300K into the liquid was measured in this study.

2.1 Experimental Details

Experiments were performed in a 1000-ton cubic anvil press as described elsewhere [28] as shown in Figure 2.1.

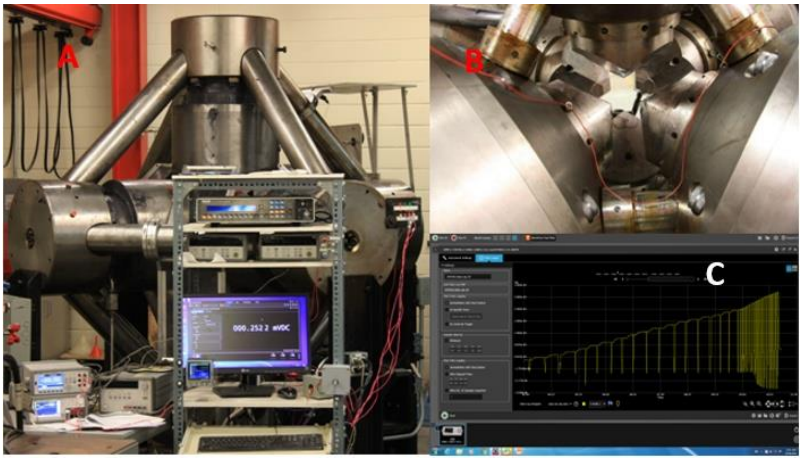

Figure 2.1 (A): 1000 ton cubic anvil press, along with power supply, digital multimeter connected to a PC. (B) Photo showing the anvils with the hydraulic rams and (C) Software system displaying real-time data acquired by the digital multimeter.

The four-wire resistivity measurement technique and the cubic pressure cell design are illustrated in Figure 2.2. Pyrophyllite was used as the P-transmitting medium and the sample pressure was determined from hydraulic oil pressure using prior unpublished calibrations similar to those previously described [28, 29]. The dimensions of the Cu wire (99.99% purity, Alfa Aesar) were 0.51mm in diameter and 1.78mm in length. The junctions of two W5%Re-W26%Re thermocouples, which also served as 4-wire electrodes, were in direct contact with the ends of the wire sample which was contained in boron nitride (BN). Boron nitride was also used to contain the thermocouples and provided a tight seal at the metal–ceramic interface which helped in containing the liquid above the melting T. The sample length was 0.05mm longer than the BN sample container which provided good thermocouple/electrode-sample contact. A cylindrical graphite sleeve surrounding the sample container acted as a heat source when a high alternating current was passed through it. A cylindrical zirconia (ZrO_2) sleeve and two ZrO_2 disks placed on top and bottom of the sample container provided thermal insulation. The softening of the sample and the electrodes at high T provided good sample-electrode contact thereby minimizing the effect of contact resistance. To ensure good contact was made prior to recording data, a pre-heating and cooling cycle was carried out up to T of ~1000K at the run P. The resistivity data reported here were then acquired on second heating.

Ideally, two pairs of opposite faces of a cubic P-cell are needed to make a 4-wire resistivity measurement. With one pair of cube faces dedicated to the heater, and another pair needed for T measurement, a straightforward 4-wire electrode system was not possible. The adopted solution was to use the thermocouples as T sensors in one mode of measurement and 4-wire electrodes in

another mode. A switched circuit passed a constant direct current of 0.2A (Keysight B2961A power source) through the W5%Re leads and sample and measurement of the voltage drop was made using the W26%Re leads while the switch was in resistance mode (Figure 2.2A). In T mode, the thermocouple EMF's at the top and bottom of the sample were used to measure T (Figure 2.2B). During data processing, the corresponding EMF value for room T for a W-Re thermocouple was added to all EMF data to replace the standard "cold ice junction" reference of the thermocouple. The duration of the heating lasted for ~30mins which is not long enough to have changed the temperature of the back end of the anvil from its room T value.

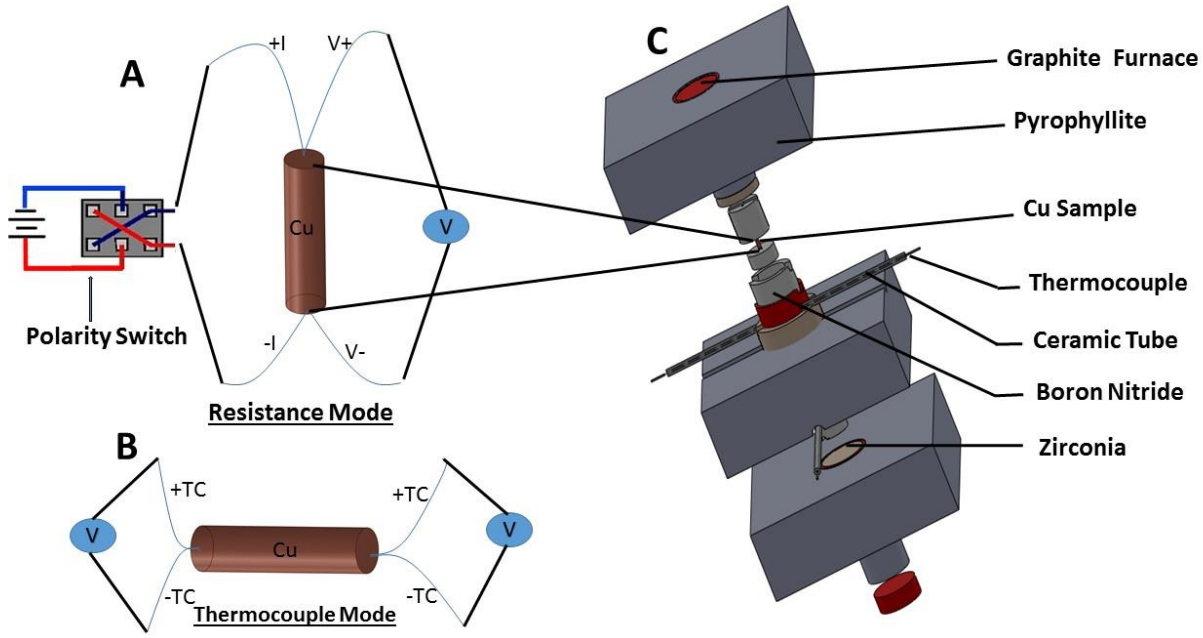

Figure 2.2. Schematic drawing of two modes (resistance (A) and temperature (B)) of measurement. (A) Four–wire probe design, showing the current polarity switch and the voltmeter for measuring the voltage drop across the sample. (B) Thermocouples measuring the temperature on top and bottom of the sample. (C) SolidWorks^{TM} design of the high-pressure cubic cell (1 inch edge length) with the components parts.

In resistance mode, systematic errors in the voltage drop across the sample from the thermoelectric voltage between the sample and the electrodes were corrected by reversing the

current direction with the use of a polarity switch. The mean value of the measured voltages in both current directions was computed at each T. A Keysight 34470A data acquisition meter, operating at a frequency of 20Hz with 1μV resolution, was used to make measurements at 50K intervals in the solid state and at 20K intervals in the liquid state. The decrease in measurement interval in the liquid state was aimed at getting enough data to define a T-dependence of resistivity before the sample geometry could change caused by liquid movement. The acquired data were processed to calculate sample resistivity in the usual manner using Ohm's law, $R = \frac{V}{I}$, where R is resistance, V is voltage drop and I is current. The sample resistivity (ρ) was calculated by incorporating the recovered sample geometry into Pouillet's law $\rho = \frac{RA}{l}$, where l and A are sample length and cross-sectional area, respectively. After each run, the recovered P cell was ground in a direction parallel to the radial axis of the cylindrical graphite heater to expose the middle section of the sample. The length and diameter of the exposed sample were carefully measured at several locations using a Nikon SMZ2800 microscope. The chemical composition of the recovered sample and electrodes was determined by wavelength dispersive X-ray spectroscopy using a JEOL JXA-8530F field-emission electron microprobe. An accelerating voltage of 20kV, a probe current of 50nA, and a spot size (~100nm) beam were used for all analyses.

2.2. Results and Discussion

Measurements of the T-dependence of the electrical resistivity of Cu at P of 2-5 GPa and at T up to 300K above the melting point are shown in Figure 2.3. In comparison with the recommended 1 atm data by Matula [22], the high P data in obtained in this study show very good agreement both in the solid and liquid states and they demonstrate the expected T- and P-effects on resistivity. The abrupt increase in resistivity marks the solid-liquid transition in Cu as shown in Figure 2.3.

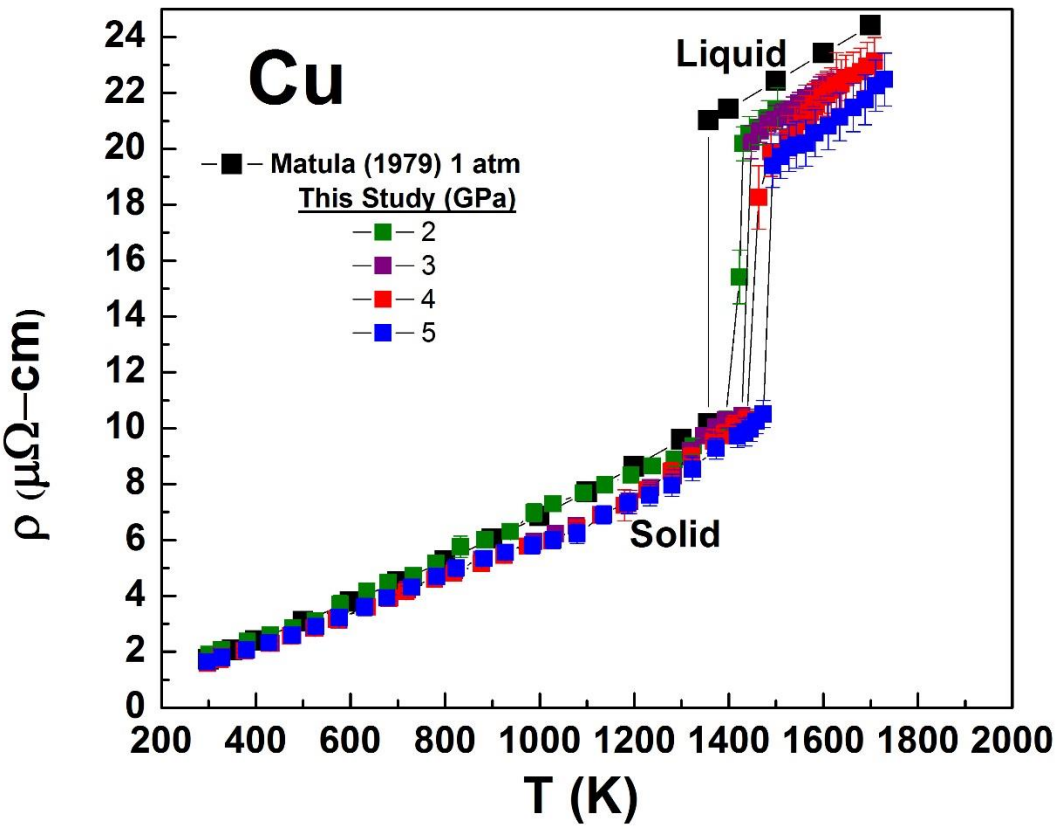

Figure 2.3. Temperature dependence of electrical resistivity of Cu at fixed pressures compared with 1atm data from several studies as recommended by Matula [22].

The melting T at a fixed P was determined by taking the average of the T measured at the start and completion of melting. The melting T determined at 2GPa in this way agrees with previous experimental studies carried out in large volume presses and in diamond anvil cells [29-32] as shown in Figure 2.4, but shows an average deviation of ~1.8% over the P range 2-5 GPa. The results of the melting temperature calculation by Vocadlo et al. [33] are lower than all experimental results. The melting point differences between measured results in this study and the other experimental studies are probably caused by the high rate of heating, polarity switching rate

of ~1s and the positions of the thermocouples which are ~0.7mm away from the hottest (i.e. central) part of the sample in these experiments.

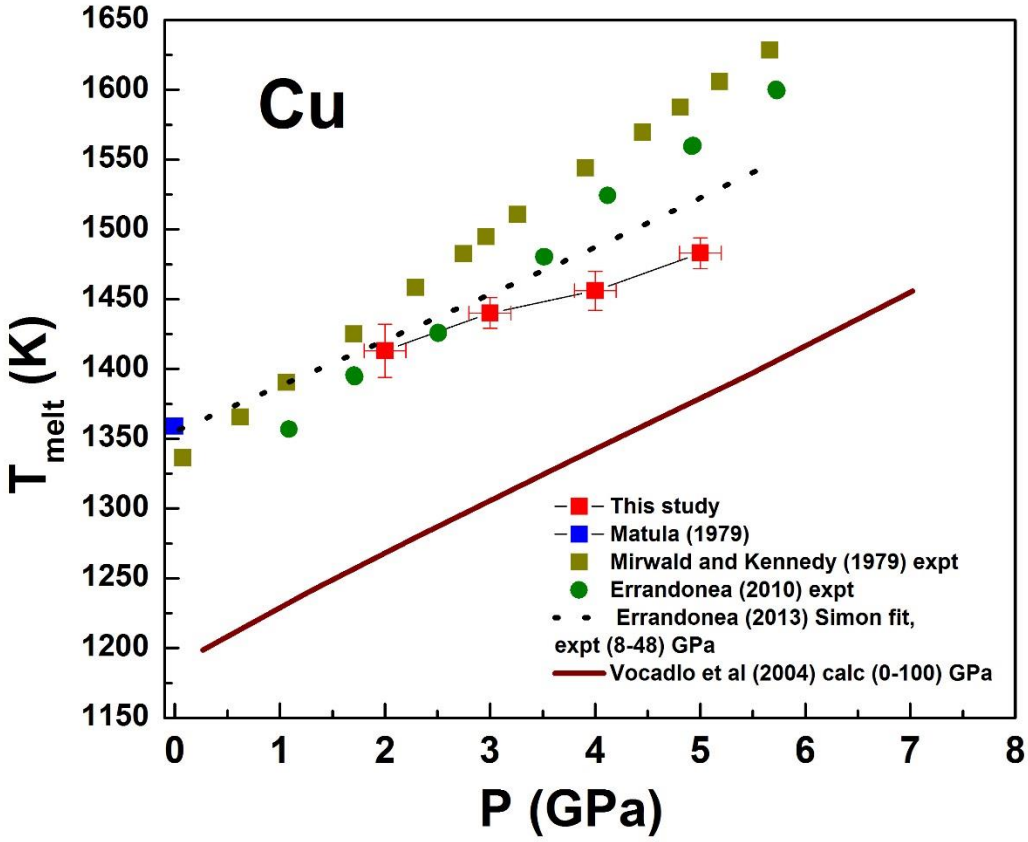

Figure 2.4. Melting curve of Cu up to 5GPa, determined by the jump in resistivity in this study, compared with previous studies.

Though measurements were made with one P-cell design and strict adherence to one experimental procedure, there were typically slight but significant differences in the geometry between successive sample assemblies after high P and T exposure. These require correction by careful inspection of the recovered sample and measurement of the geometry under microscope as shown in Figure 2.5A. These geometry values were used as input into the calculation of the resistivity. It is evident from microprobe analyses of the recovered sample, an example of which

is shown Figure 2.5B, there was no contamination of the sample either by the electrode/thermocouple or container material. These microprobe results are consistent with the phase diagram of the Cu-W binary system [34] and the absence of any interaction of liquid Cu and Re [35].

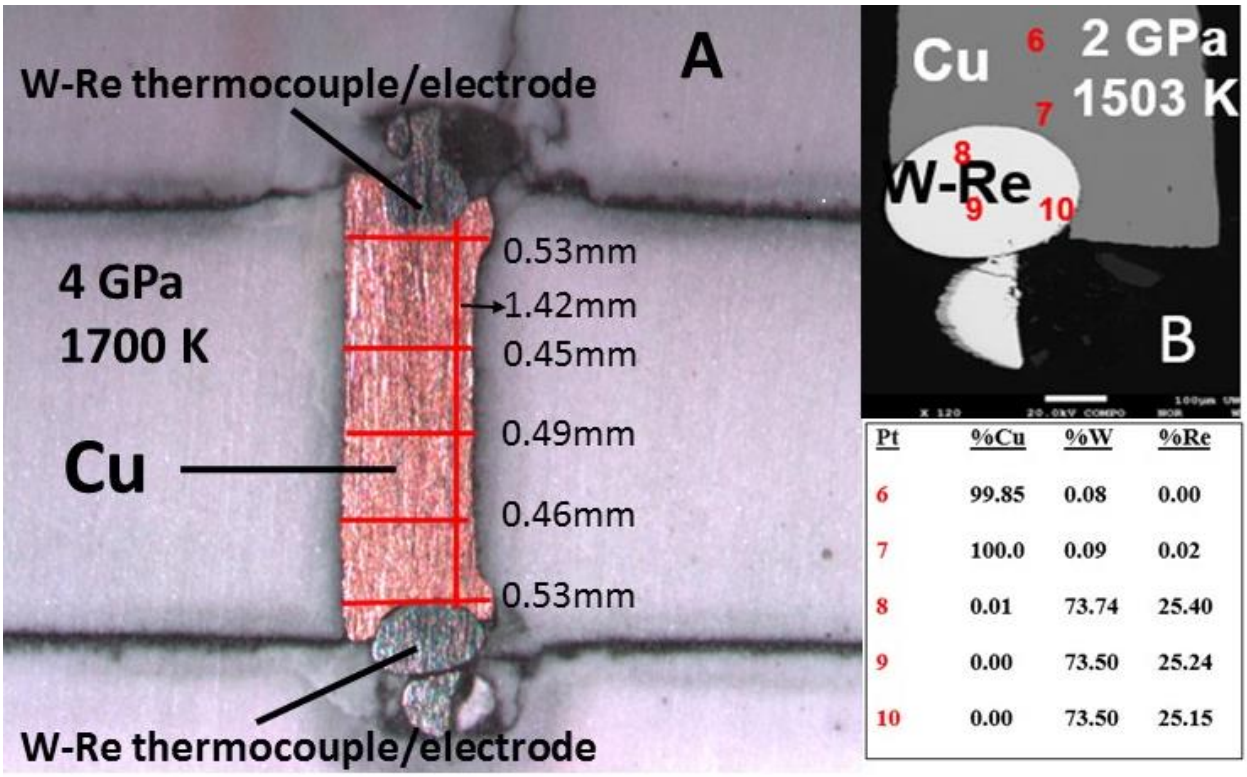

Pt	%Cu	%W	%Re
6	99.85	0.08	0.00
7	100.0	0.09	0.02
8	0.01	73.74	25.40
9	0.00	73.50	25.24
10	0.00	73.50	25.15

Figure 2.5. (A) Post-mortem view of a sectioned pressure cell recovered from 4 GPa and 1700 K. Thermocouple/electrodes were W5%Re and W26%Re. Measurements of the length and width at several locations of the ground Cu sample are labelled. (B) Back scattered electron image of a sample recovered from 2GPa, 1503K along with tabulated electron microprobe results of probe points 6-10. The white scale bar is 100μm.

As expected, the resistivity of Cu decreases with increasing P in the solid state as shown by the isothermal resistivity behavior at 1350K in Figure 2.6. The electronic structure of Cu has been very well investigated both experimentally and theoretically [36-43]. Studies have shown that the interaction between the high-lying *3d*-band and the *s* conduction band lead to appreciable

distortion of the Fermi surface of Cu from a perfect sphere [13, 44]. Experiments probing the dHvA oscillations of the magnetic susceptibility and theoretical studies on the effect of P on the Fermi surface of Cu have shown that the neck section increases relative to the bellies [15-17]. The increased distortion of the Fermi surface with P promotes zone boundary scattering which diminishes the velocity of the Fermi electrons and enhances the electrical resistivity. However on any given isotherm, the effect of P-induced increase of E_{Fd} [20], which decreases the scattering caused by the reduced influence of the periodic electron density on the conduction *s* electrons as well as the P-induced reduction of the phonon amplitude, causes a net decrease in resistivity in the solid state.

The resistivity at the solid-liquid phase transition doubles in value as shown in the resistivity ratio plotted versus P in Figure 2.6. Other metals similar to Cu in crystal and electronic structure, such as Ag and Au, show similar doubling of the resistivity on melting at 1atm [22]. The change in resistivity upon melting correlates with the Lennard-Jones and Devonshire [45] order-disorder melting theory. In this model, the adjustable parameter *W*, which is a measure of the energy change required to transfer an atom from its position to a nearest neighbour position on the same lattice, is controlled by interatomic forces. Melting occurs as a result of a decrease in the interatomic forces which translate to a change in atomic structure from an ordered to disordered state. The interatomic forces on melting control the dynamics of the ions which influence electron scattering and hence resistivity.

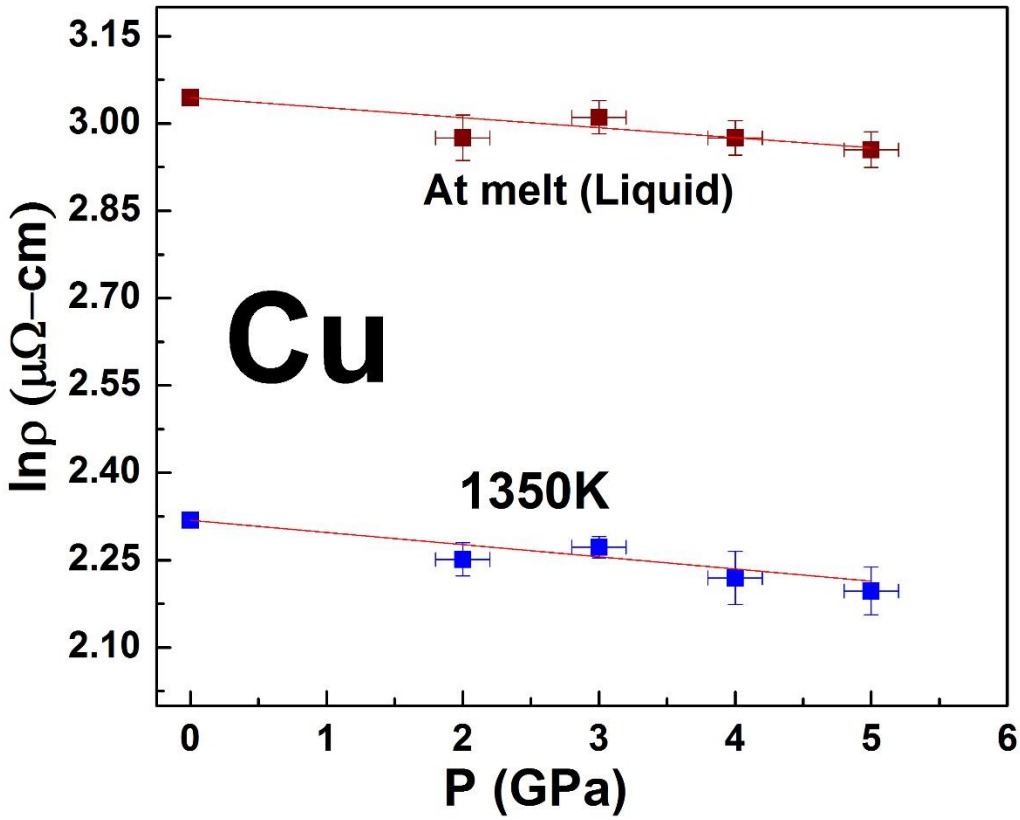

Figure 2.6. P-dependence of electrical resistivity of Cu in the solid state along the 1350K isotherm and in the liquid state along the melting boundary. The calculated slopes for the pressure coefficient of resistivity of the fitted lines are $(d\ln\rho/dP)_{1350K}$ = -0.021 $\pm$ 0.003 GPa^{-1} and $(d\ln\rho/dP)_{melt\ boundary}$ = -0.017 $\pm$ 0.003 GPa^{-1}. Data at 1 atm are from Matula [22].

From the NFE model [4], the relative change in electrical resistivity during melting is caused by the change in the radial distribution function of the ions which results in larger ion scattering cross-sections. T-variation of resistivity in the liquid state follows from the T-dependent Fourier transform of the radial distribution function, or structure factor, of the ions in the liquid state. The spherical nature of the Fermi surface of most liquid metals [18, 19] demonstrates that thermal expansion could very well compensate for the distortion effects of P on the Fermi surface of Cu on melting. If these effects were cancelling, they would cause the resistivity of Cu at the

melting boundary to be constant. However, the effect of P-induced increase of E_{Fd} and the P-induced decrease of phonon amplitudes appear to dominate over effects of T as shown in the decreasing behavior of resistivity at the melting boundary in Figure 2.7.

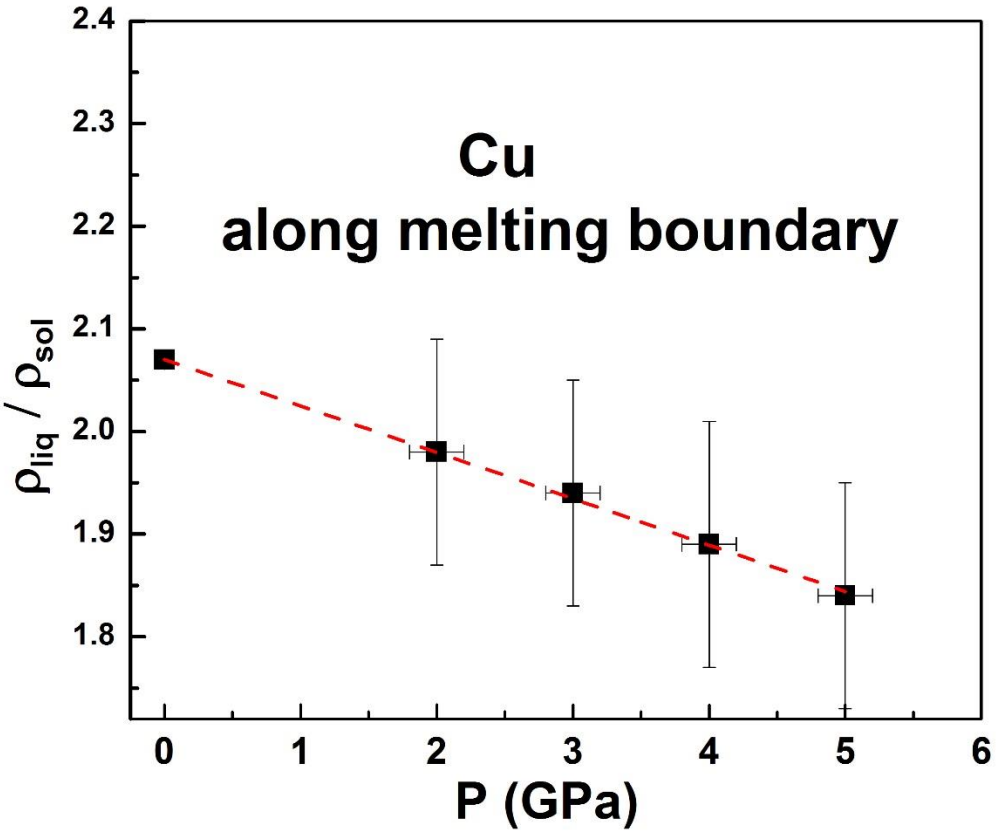

Figure 2.7. P-dependence of the resistivity ratio of liquid to solid at the melting point. Least squares fit (r^2 = 0.998) yields ρ_{liq}/ρ_{sol} = 2.072 - 0.0457 (0.0006) P GPa^{-1}.

The T-coefficient of resistivity $(d\ ln\ \rho\ /d\ T)_P$ in the liquid state and at three temperature ranges in the solid state obtained in this study are plotted versus P in Figure 2.8 and are compared with 1atm studies. Measured values in this study are in general agreement with 1atm values, however, there does not appear to be a P-dependent trend in any of the temperature data sets. There is no indication in the T-coefficient of resistivity behaviour that would suggest a P-induced change

in structure of Cu in either the solid or liquid state, in agreement with the phase diagram of Cu reported up to 6GPa [46].

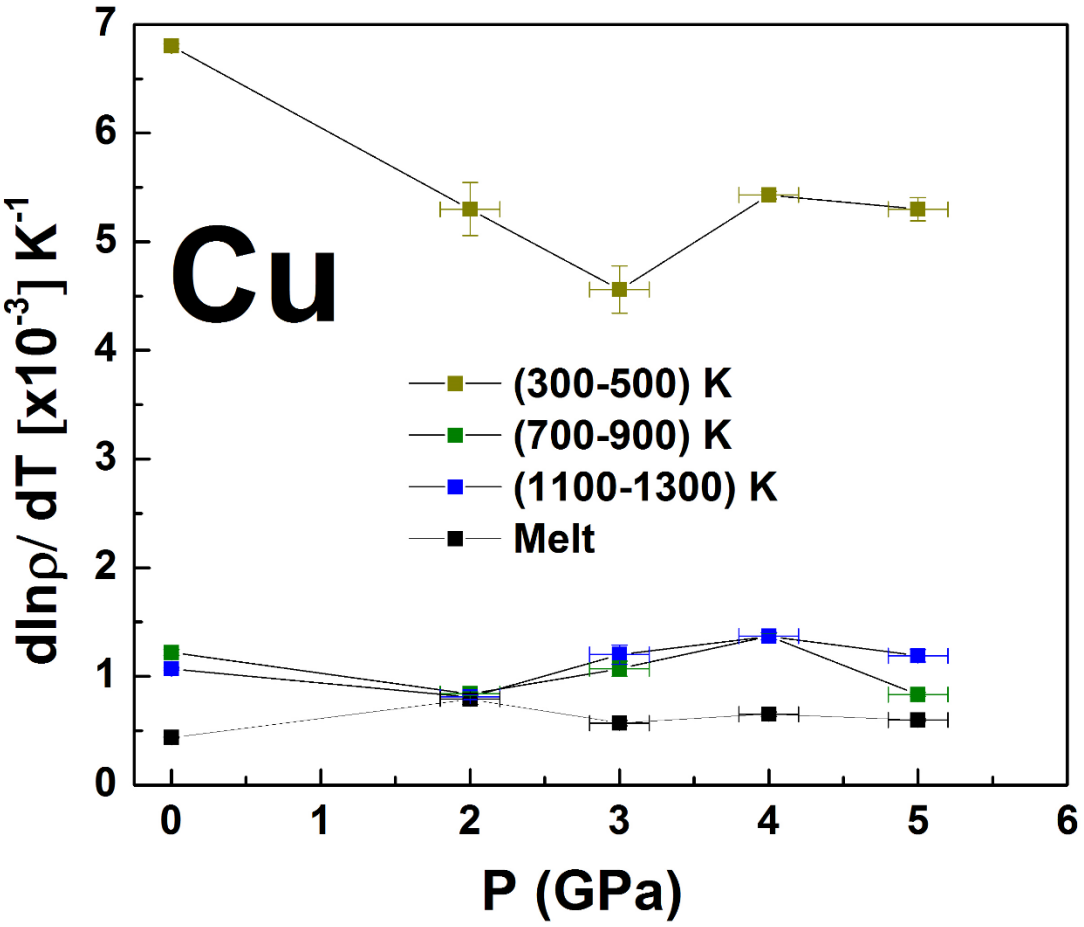

Figure 2.8. The T coefficient (dlnρ/dT) of electrical resistivity plotted for liquid Cu and three temperature ranges in the solid state for P range of 2-5GPa. Comparison is made with *dlnρ/dT* derived from the1atm data of many studies as compiled by Matula [22]. Error bars are provided or are within the symbol size.

As shown in Figure 2.6, the P-coefficient of resistivity on the melting boundary, $\left(\frac{\partial \ln \rho}{\partial P}\right)_{melt\ boundary}$ is -0.017 $\pm$ 0.003 GPa^{-1}, and the P-coefficient of resistivity along the 1350K isotherm, $\left(\frac{\partial \ln \rho}{\partial P}\right)_{1350K,}$ is -0.021 $\pm$ 0.003 GPa^{-1}. The value calculated using the relationship

derived by Stacey and Anderson [26] at $\left(\frac{\partial \ln \rho}{\partial \mathrm{P}}\right)_{1350K,}$ was compared with the results determined from this study.

$$\left(\frac{\partial \ln \rho}{\partial \mathrm{P}}\right)_{1350\mathrm{K}} = \frac{-2\,(\gamma - 1/3)}{\mathrm{K_T}} \qquad (1)$$

where γ is the Grüneisen parameter and K_T is the isothermal bulk modulus. γ was estimated to be 1.5 for solid Cu at 1350K from the 1.96 room T measurement by Chatterjee [47] and applying T-dependence of γ by Singh [48]. With a K_T value of 134GPa at 300K, K_T was extrapolated to 1350K from the T-dependence of K_T measured up to 800K by Chang and Himmel [49], to be 93.7 GPa and calculate a value of -0.025 GPa^{-1} for $(\partial \ln \rho/\partial P)_{1350K}$ from Eqn (1). The prediction of $(\partial \ln \rho/\partial P)_{1350K}$ by Eqn (1) compares well with the measured experimental value in this study. However, the $(\partial \ln \rho/\partial P)_{melting\ boundry}$ is not equal to zero which does not support the conclusion that the electrical resistivity of an electronically simple metal such as Cu is constant on the P-dependent melting boundary [1, 2]. Experimental findings in this study suggest that although electron scattering increases with both T at the melting point and with structural disorder that accompanies melting, the integrated effects of increasing P on electron scattering on melting results in an overall decrease in electrical resistivity at the melting boundary. This is clearly shown in Figure 2.7 where the ratio of the liquid to solid resistivity values at the melting point is plotted versus P. With nearly constant solid resistivity just below the melting point (10.1 – 10.5) μΩ-cm as evident in Figure 2.3, the decreasing resistivity in the liquid at the melting point with increasing P causes an overall decrease in the resistivity ratio.

There exist only few data on the direct measurement of thermal conductivity of Cu at high T and/or P [50-54]. This is primarily because of the challenges in maintaining a small T gradient at high T. At high T in the solid state and in the liquid state, there is an additional challenge of chemical contamination. At high P conditions, the challenges rise sharply. Hence, indirect

measurement and/or determination of the thermal conductivity at these conditions are desirable. The phonon contribution, k_P, to the total thermal conductivity, k_{total}, in a metal is generally negligible compared to the dominant contribution by the electrons, k_e [55]. Fortunately, the electrical resistivity is related to the electronic thermal conductivity through the Wiedemann - Franz law [56], $k_e = \frac{LT}{\rho}$ where L is the Lorenz number. Above the Debye T, the Lorenz number for solid Cu approaches the Sommerfeld value of $2.445\ x\ 10^{-8}\ V^2/K^2$ [57, 58].

The electronic thermal conductivity, k_e, of Cu was calculated from the electrical resistivity data measured in this study by using the Wiedemann-Franz law and using the Sommerfeld value of L ($2.445\ x\ 10^{-8}\ \frac{V^2}{K^2}$). The T-dependence of k_e at four P values is shown in Figure 2.9. The results of k_e were compared with those calculated in the same way using the 1atm electrical resistivity data of Matula [22]. As expected, k_e decreases with increasing T in the solid state. On melting, k_e decreases to approximately half of its solid state value and in the liquid state k_e increases slightly with T. With increasing P, k_e increases both in the solid and liquid state. Also plotted on Figure 2.8 for comparison are the recommended values of total thermal conductivity, k_{total}, at 1atm from experimental studies as collected in Ho et al. [53]. These values are recommended from a number of experimental studies and are expected to be accurate to within $\pm$4% in the solid state and $\pm$15% in the liquid state [53]. The 1atm experimental values of k_{total} are lower than the values of k_e calculated from electrical resistivity using the Wiedemann-Franz Law. This is unexpected since k_{total} is the sum of k_e and k_p. This suggests that the Sommerfeld value of the Lorenz number may not be valid for Cu at these T. The insert plot in Figure 2.9 indeed shows that the experimentally derived Lorenz number [52] varies with T for Cu and remains below the Sommerfeld value at T up to 1200K. The use of this Lorenz function would lower k_e calculated from electrical resistivity but would not completely reconcile the difference between the values of k_{total} [53] and k_e from [22]

and this study. On the other hand, the experimental study by Starr [51] indicates that the Wiedemann-Franz ratio for Cu up to a P range of 1.1GPa has a very small positive P-coefficient from the contribution of k_p.

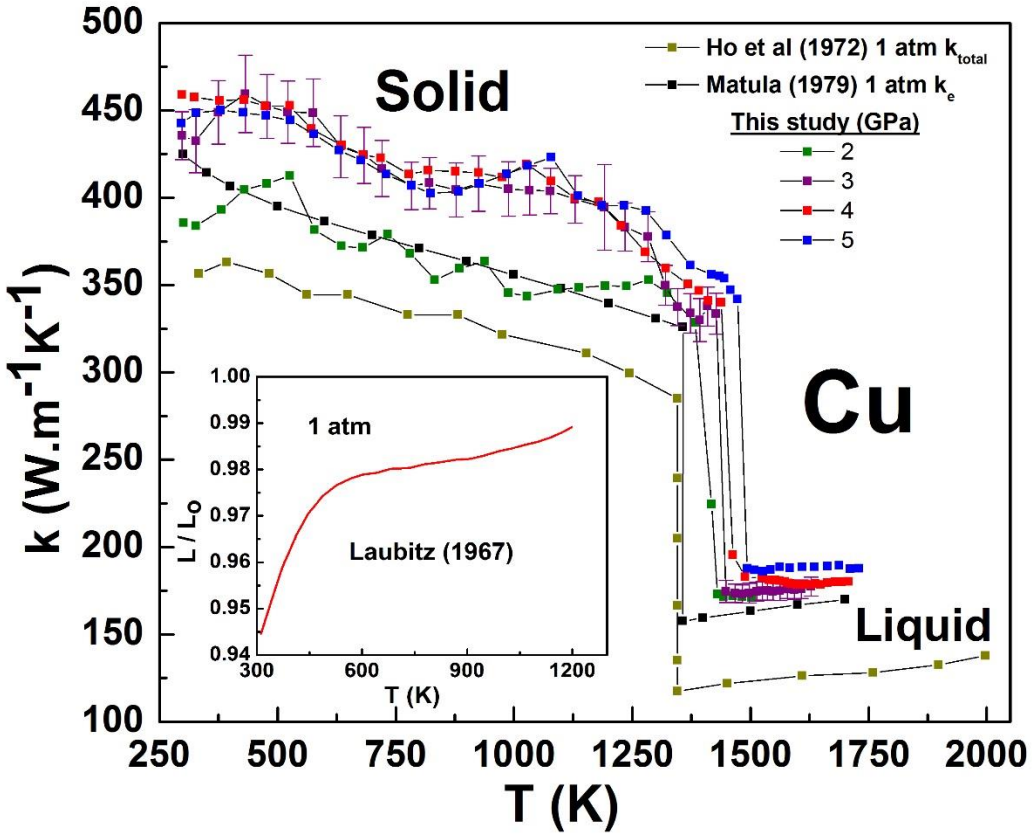

Figure 2.9. Temperature dependence of the thermal conductivity at various pressures. The electronic component (k_e) was calculated from the electrical resistivity data using the Wiedemann-Franz law and the Sommerfeld value($2.445 \times 10^{-8} \frac{V^2}{K^2}$) of the Lorenz number. Representative error bars are shown for the 3GPa dataset. Comparison is made with the electronic thermal conductivity based on Matula [22] resistivity data at 1 atm and with the total thermal conductivity (k_{total}) from experimental measurements reported in Ho et al. [53]. The inset figure shows the T-dependence of the measured Lorenz number for Cu [Laubitz [52]].

As shown in Figure 2.10, the P-dependence of k_e is plotted at, 1350K and at melt. The P-coefficient of k_e, $\left(\frac{\partial \ln k_e}{\partial P}\right)_{melt}$ of 0.038 $\pm$ 0.002 GPa^{-1} and $\left(\frac{\partial \ln k_e}{\partial P}\right)_{1350K}$ of 0.021 $\pm$ 0.003 GPa^{-1}

was calculated from the measured data. These values were compared with the same parameter calculated using the relationship derived by Bohlin [59] given in Eqn (2), which is similar to Eqn 1 for electrical resistivity:

$$\left(\frac{\partial \ln k_e}{\partial P}\right)_T = \frac{(2\gamma - {}^1/_3)}{K_T} \tag{2}$$

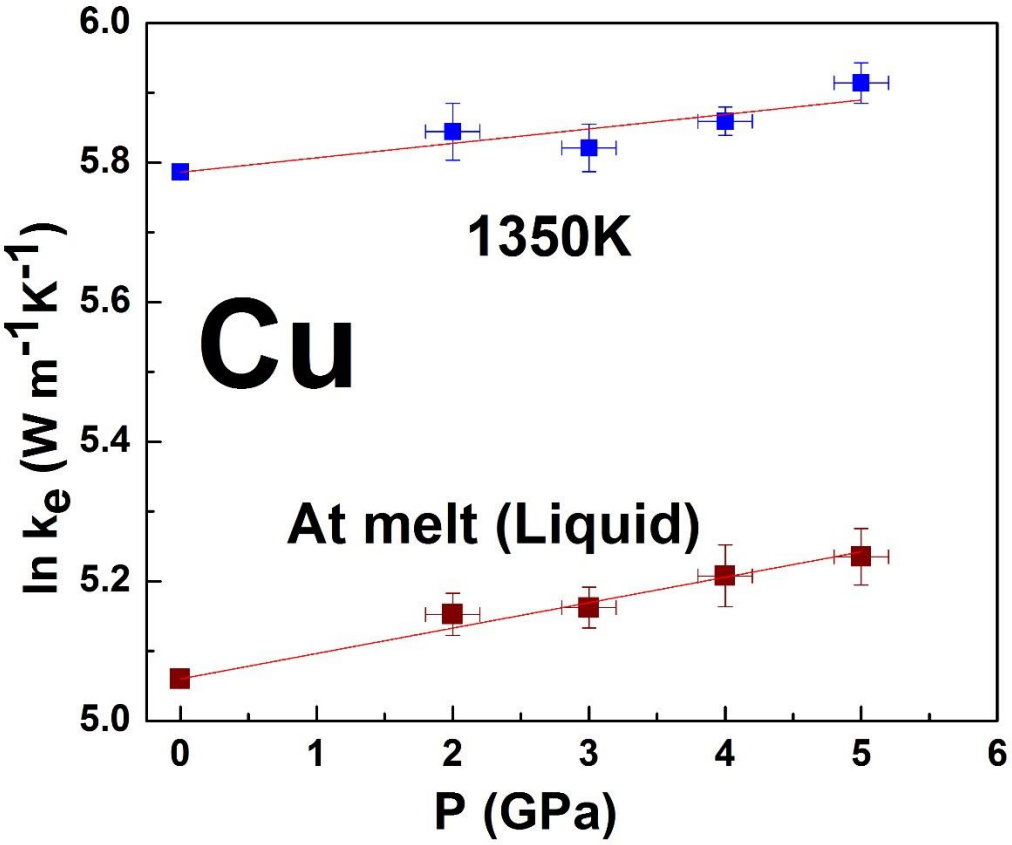

Figure 2.10. P-dependence of thermal conductivity of Cu at 1350K and along the melting boundary. The calculated slopes for the pressure coefficient of electronic thermal conductivity k_e, of the fitted lines are $(d\ln\rho/dP)_{1350K}$ = $(0.021 \pm 0.003)GPa^{-1}$ and $(d\ln\rho/dP)_{\text{melt boundary}}$ = (0.038 ± 0.002) GPa^{-1}.

A value of 0.038$\pm$ 0.003 GPa^{-1} for $(\partial \ln k_e / \partial P)_{1350K}$ was caluclated from Eqn (4), assuming a 10% error on γ *and* K_T values. The prediction of $(\partial \ln k_e / \partial P)_{1350K}$ by Eqn (2) is reasonably close to measured value in this study. Experimental findings from this study suggest that although electron mobility decreases with both T on the melting boundary and with structural disorder that accompanies melting, the integrated effects of increasing P on k_e on melting results in an overall increase in k_e.

2.3. Conclusions

The T-dependence of electrical resistivity of Cu in both solid and liquid states has been investigated up to P of 5GPa. Results show that the electrical resistivity at the melting T decreases as a function of P in contrast to prediction. These findings are interpreted in terms of the antagonistic effects of P and T on the electronic structure of liquid Cu as demonstrated in previous studies. The electronic thermal conductivity was calculated using the Wiedemann-Franz law with the Sommerfeld value of the Lorenz number. The electronic component of thermal conductivity increases with P both in the solid and liquid states and at fixed P, it decreases as a function of T in the solid state, but increases with T in the liquid state. Comparison of the calculated electronic thermal conductivity and experimentally measured total thermal conductivity at 1atm indicates that phonon conductivity is very low in Cu. Within experimental error, melting T measured in this study at P values up to 5GPa are in agreement with previous experimental studies.

2.4 References

[1] Stacey, F. D. and Anderson, O. L. (2001). Electrical and thermal conductivities of Fe–Ni–Si alloy under core conditions. *Physics of the Earth and Planetary Interiors*, *124*(3), 153-162.

[2] Stacey, F. D. and Loper, D. E. (2007). A revised estimate of the conductivity of iron alloy at high pressure and implications for the core energy balance. *Physics of the Earth and Planetary Interiors*, *161*(1), 13-18.

[3] Mott, N. F. (1936). The electrical conductivity of transition metals. In *Proceedings of the Royal Society of London A: Mathematical, Physical and Engineering Sciences* Vol. 153(880), 699-717.

[4] Ziman, J. M. (1961). A theory of the electrical properties of liquid metals. I: The monovalent metals. *Philosophical Magazine*, *6*(68), 1013-1034.

[5] Mott, N. F. (1972). The electrical resistivity of liquid transition metals. *Philosophical Magazine*, *26*(6), 1249-1261.

[6] Evans, R., Greenwood, D. A., and Lloyd, P. (1971). Calculations of the transport properties of liquid transition metals. *Physics Letters A*, *35*(2), 57-58.

[7] Dreirach, O., Evans, R., Guntherodt, H. J., and Kunzi, H. U. (1972). A simple muffin tin model for the electrical resistivity of liquid noble and transition metals and their alloys. *Journal of Physics F: Metal Physics*, *2*(4), 709.

[8] Hirata, K., Waseda, Y., Jain, A., and Srivastava, R. (1977). Resistivity of liquid transition metals and their alloys using the t matrix. *Journal of Physics F: Metal Physics*, *7*(3), 419.

[9] Ononiwu, J. S. (1993). Calculation of electrical resistivity of liquid transition metals. P*hysica Status Solidi (b)*, *177*(2), 413-423.

[10] Shvets, V. T., Savenko, S., and Datsko, S. (2002). Perturbation theory for electrical resistivity of liquid transition metals. Journal of Physics *Condensed Matter Physics*, *5*(3), 31.

[11] Bradley, C. C., Faber, T. E., Wilson, E. G., and Ziman, J. M. (1962). A theory of the electrical properties of liquid metals II. Polyvalent metals. *Philosophical Magazine*, *7*(77), 865-887.

[12] Ziman, J. M. (1960). Electrons and Phonons: The Theory of Transport Phenomena in Solids. pp 112-113. Oxford Univ. Press.

[13] Segall, B. (1962). Fermi surface and energy bands of copper. *Physical Review*,*125*(1), 109.

[14] Pippard, A. B. (1957). An experimental determination of the fermi surface in copper. *Philosophical Transactions of the Royal Society of London A: Mathematical, Physical and Engineering Sciences*, *250*(979), 325-357.

[15] Templeton, I. M. (1974). The effect of hydrostatic pressure on the fermi surfaces of copper, silver, and gold. II. High precision studies. *Canadian Journal of Physics*, *52*(17), 1628-1634.

[16] O'Sullivan, W. J., and Schirber, J. E. (1968). Experimental determination of the effect of hydrostatic pressure on the Fermi surface of copper. *Physical Review*, *170*(3), 667.

[17] Ahuja, R., Solanki, A. K., and Auluck, S. (1989). Effect of pressure on the Fermi surface of noble metals. *Physical Review B*, *39*(14), 9806.

[18] Ashcroft, N. W., and Lekner, J. (1966). Structure and resistivity of liquid metals. *Physical Review*, *145*(1), 83.

[19] Faber, T. E. (2010). Introduction to the Theory of Liquid Metals. Cambridge University Press.

[20] Zallen, R. (1966). The effect of pressure on optical properties of the noble metals. *Optical properties and electronic structure of metals and alloys: Proceedings of the International Colloquium*, 164.

[21] Miller, J. C. (1969). Optical properties of liquid metals at high temperatures. *Philosophical Magazine*, *20*(168), 1115-1132.

[22] Matula, R. A. (1979). Electrical resistivity of copper, gold, palladium, and silver. *Journal of Physical and Chemical Reference Data*, *8*(4), 1147-1298.

[23] Keeler, R. N., (1971) Electrical Conductivity of Condensed Media at High Pressures, in Physics of High Energy Density, Ed. by P. Caldirola and H. Knoepfel (Academic Press, New York, 1971).

[24] Bloomquist, D.D. and Sheffield, S.A., (1981) Shock-Compression Temperature Rise in Polymethyl Methacrylate Determined from Resistivity of Embedded Copper Foils, *Applied Physics Letters*, 38 (3), 185–187.

[25] Gulevich, M. A. (2011). Measurement of electrical conductivity of copper under impulsive loading. *Combustion, Explosion, and Shock Waves*, *47*(6), 715-720.

[26] Gilev, S. D., and Prokop'ev, V. S. (2016). Electrical resistance of copper under shock compression: Experimental data. *Combustion, Explosion, and Shock Waves*, *52*(1), 107-116.

[27] Bridgman, P. W. (1952, March). The resistance of 72 elements, alloys and compounds to 100,000 Kg/Cm². In *Proceedings of the American Academy of Arts and Sciences*, Vol. 81, No. 4, pp. 165-251.

[28] Secco, R. A. (1995). High P, T physical property studies of Earth's interior: Thermoelectric power of solid and liquid Fe up to 6.4GPa. *Canadian Journal of Physics*, *73*(5-6), 287-294.

[29] Secco, R. A., and Schloessin, H. H. (1986). On-line p, T calibration based on well-known phase transitions. *Journal of Applied Physics*, *60*(5), 1625-1633.

[30] Mirwald, P. W., and Kennedy, G. C. (1979). The melting curve of gold, silver, and copper to 60-Kbar pressure: A reinvestigation. *Journal of Geophysical Research: Solid Earth*, *84*(B12), 6750-6756.

[31] Errandonea, D. (2010). The melting curve of ten metals up to 12GPa and 1600 K. *Journal of Applied Physics*, *108*(3), 033517.

[32] Errandonea, D. (2013). High-pressure melting curves of the transition metals Cu, Ni, Pd, and Pt. *Physical Review B*, *87*(5), 054108.

[33] Vočadlo, L., Alfe, D., Price, G. D., and Gillan, M. J. (2004). Ab initio melting curve of copper by the phase coexistence approach. *The Journal of Chemical Physics*, *120*(6), 2872-2878.

[34] Subramanian, P. R., and Laughlin, D. E. (1991). Cu-W (Copper-Tungsten). *Phase diagrams of binary tungsten alloys*, 76-79.

[35] Davis, J. R. (Ed.). (1997). *ASM Specialty Handbook: Heat-resistant Materials*. ASM International, pp 380.

[36] Baym, G. (1964). Direct calculation of electronic properties of metals from neutron scattering data. *Physical Review*, *135*(6A), A1691.

[37] Zornberg, E. I., and Mueller, F. M. (1966). Fermi surface of copper. *Physical Review*, *151*(2), 557.

[38] Mijnarends, P. E. (1969). Determination of the Fermi surface of copper by positron annihilation. *Physical Review*, *178*(2), 622.

[39] Chelikowsky, J. R., and Chou, M. Y. (1988). Electronic and structural properties of elemental copper: A pseudopotential–local-orbital calculation. *Physical Review B*, *38*(12), 7966.

[40] Zhou, Y., Lai, W., and Wang, J. (1994). Calculated electronic structure of metastable phases of Cu. *Physical Review B*, *49*(7), 4463.

[41] Yamasaki, A., and Fujiwara, T. (2003). Electronic structure of transition metals Fe, Ni and Cu in the GW approximation. *Journal of the Physical Society of Japan*, *72*(3), 607-610.

[42] Vos, M., Kheifets, A. S., Bowles, C., Chen, C., Weigold, E., and Aryasetiawan, F. (2004). Electronic structure of copper studied by electron momentum spectroscopy. *Physical Review B*, *70*(20), 205111.

[43] Thakor, P. B., Sonvane, Y. A., and Jani, A. R. (2009). Electronic transport properties of some transition liquid metals. *Physics and Chemistry of Liquids*, *47*(6), 653-662.

[44] Spicer, W. E., and Berglund, C. N. (1964). d -band of copper. *Physical Review Letters*, *12*(1), 9.

[45] Lennard-Jones, J. E., and Devonshire, A. F. (1939). Critical and co-operative phenomena. III. A theory of melting and the structure of liquids. *Proceedings of the Royal Society of London. Series A, Mathematical and Physical Sciences*, 317-338.

[46] Tonkov, E. Y., and Ponyatovsky, E. G. (2004). Phase transformations of elements under high pressure (Vol. 4). CRC press.

[47] Chatterjee, B. (1981). On the relation of the grüneisen parameter to the thermal stability of metals. *Metallurgical Transactions A*, *12*(8), 1531-1534.

[48] Singh, R. N., Arafin, S., and George, A. K. (2007). Temperature-dependent thermo-elastic properties of s-, p-and d-block liquid metals. *Physica B: Condensed Matter*, *387*(1), 344-351.

[49] Chang, Y. A., and Himmel, L. (1966). Temperature dependence of the elastic constants of Cu, Ag, and Au above room temperature. *Journal of Applied Physics*, *37*(9), 3567-3572.

[50] Bridgman, P. W. (1922) The effect of pressure on the thermal conductivity of metals. In *Proceedings of the American Academy of Arts and Sciences* (Vol. 57, No. 5, pp. 77-127). American Academy of Arts and Sciences.

[51] Starr, C. (1938). The pressure coefficient of thermal conductivity of metals. *Physical Review*, *54*(3), 210.

[52] Laubitz, M. J. (1967). Transport properties of pure metals at high temperatures: I. Copper. *Canadian Journal of Physics*, *45*(11), 3677-3696.

[53] Ho, C. Y., Powell, R. W., and Liley, P. E. (1972). Thermal conductivity of the elements. *Journal of Physical and Chemical Reference Data*, *1*(2), 279-421.

[54] Sundqvist, B., and Bäckström, G. (1977). Thermal conductivity of copper under high pressure. *High Temperatures-High Pressures*, *9*(1), 41-48.

[55] Klemens, P. G., and Williams, R. K. (1986). Thermal conductivity of metals and alloys. *International Metals Reviews*, *31*(1), 197-215.

[56] Franz, R., and Wiedemann, G. (1853). Ueber die wärme-leitungsfähigkeit der metalle. *Annalen der Physik*, *165*(8), 497-531.

[57] Moore, J. P., McElroy, D. L., and Graves, R. S. (1967). Thermal conductivity and electrical resistivity of high-purity copper from 78 to 400° K. *Canadian Journal of Physics*, *45*(12), 3849-3865.

[58] Giordanengo, B., Benazzi, N., Vinckel, J., Gasser, J. G., and Roubi, L. (1999). Thermal conductivity of liquid metals and metallic alloys. *Journal of Non-Crystalline Solids*, *250*, 377-383.

[59] Bohlin, L. (1976). Thermal conduction of metals at high pressure. *Solid State Communications*, *19*(4), 389-390.

Chapter 3: Constant Electrical Resistivity of Zn on the Pressure Dependent Melting Boundary

3.0. Introduction

The attention of experimentalists and theorists in the high pressure (P) community studying the properties of Zn at extreme conditions have focused on understanding the hypothesized thermodynamically driven electronic topological transformation (Lifshitz transition) [1] in correlation with the abnormal c/a ratio of Zn [2, 3]. At ambient conditions, Zn has a distorted hexagonal close-packed (hcp) structure with a c/a ratio of 1.856, which is considerably larger than the ideal hcp c/a ratio of 1.633, as in the case of Mg. Although no structural transition has been observed in Zn up to 126GPa [4], the bonding anisotropy in the crystal structure changes under compression causing the abnormal c/a ratio to approach the ideal hcp value with increasing P at ambient temperature (T). Studies have suggested that the unusual c/a ratio results from the differences in the density of states of electrons at the Fermi energy relative to elements with ideal hcp value [5] or the bonding of *d* electrons through hybridization [6]. Some early x-ray diffraction studies observed anomalies in the trend of decreasing c/a ratio [2, 3] with increasing P, while some studies did not [7-9]. However, recent XRD study with more hydrostatic compression, using He as a pressure medium [10] demonstrated that the c/a ratio decreases uniformly towards the ideal hcp value with increasing P and associated the artifacts in the results of earlier experiments [2, 3] with the effects of non-hydrostatic P transmitting medium. Theoretical calculation has also demonstrated the absence of lattice strain anomalies at the electronic topological transition in Zn

at high P [11]. Thus, recent experimental and theoretical studies [10, 11] have resolved the long-standing conflict of different experimental and theoretical results.

The Fermi surface of Zn has many complex features, which have attracted many experimental and theoretical studies [12-18] over the past few decades in an attempt to understand the electronic transport mechanisms in Zn. The Fermi surface of Zn contains three elements ("cap", "monster" and "lens") of the six possible Fermi surface elements (e.g. Mg). The "cigar" and "butterfly" near the symmetry point L and the "needle" near the symmetry point K of the Brillouin zone (BZ) are absent in the Fermi surface of Zn at ambient conditions [19]. When incorporated in the theoretical model of the band structure of Zn [12, 15], the spin orbit coupling proposed by Cohen and Falicov [20] successfully explained the lack of saturation of magnetoresistance field normal to the c-axis [21]. Similarly, Joseph et al. [22], using de Hass van Alphen (dHvA) experimental technique, observed oscillations in the magnetic susceptibility of Zn which were accounted for using a model of the Fermi surface that included the effect of interaction between electron spin and its orbits (spin-orbit coupling). The effect of orbit splitting causes the region of holes in the first band to separate from the region of holes in the second band, causing the latter to extend infinitely along the c-axis [20], which leads to lack of saturation in the magnetic field normal to c-axis. The splitting effect shortens the mean free path of conduction electrons due to the restriction of the electrons in one zone and hence increases electrical resistivity. Experimental study [23] has demonstrated that at magnetic breakdown, the free electron surface restores and electrons can tunnel from one orbit to the other, which leads to an increased mean free path and lower resistivity.

Generally in transition metals, the mobility of delocalized electrons in the *s* band is greater than electrons in the *d*-band, thus metals with filled *d*-band such as Zn are generally more

conductive compared with unfilled *d*-bands metals. At ambient conditions, Zn has two atoms per unit cell, with an electronic configuration of [Ar] $3d^{10}4s^2$ and associated complex Fermi surface sections [24-26] that extend up to the third BZ. Together with the spin orbit splitting in the *K* symmetry which leaves holes and clusters of electrons [12, 19, 20] in its electronic structure, the Fermi surface terminations at and contacts with the BZ edges confines electrons which consequently causes a decrease in electron density of states and results in higher electrical resistivity. The many zone boundaries also suggest that the boundary scattering in Zn is large which results in further increased electrical resistivity. Molecular simulation study of Zn electronic structure [27] demonstrated that the narrow *d*-band overlapping the bottom of the broad *s* band and the top of the *p* band [28-29] induces a minimum in the density of states of the conduction electrons at the Fermi level. The atomic volume influences the degree of overlap between the *sp* and *d*-bands and relativistic effects, which tend to lower the *s* states not only to the *d*, but also relative to the *p* states [27]. From the bonding scheme approach [30], the abnormal nature of the electronic structure of Zn caused by a system of covalent bonds in the basal plane resulting from bonding orbitals that are hybrids of one *d* and two *p* atomic orbitals, accepts *s* electrons and leaves only 1.33 electrons/atom in the *s*-band. Hence, the molecular simulation results somewhat agree with the proposed covalent bonds in terms of bonding and hybridization inducing a minimum in the density of states near the Fermi level of Zn at ambient conditions.

A theoretical study by Ballentine [31] showed that the electronic structure of liquid Zn is nearly free electron (NFE) like. The electrical resistivity of liquid Zn can be accounted for in the theory of Ziman NFE model [32, 33] when both the electron-ion pseudopotential matrix element, which describes electron-ion core scattering, and the dynamic structure factor that depends on the effective packing density of the ions system and characterized by ion-ion interactions, are known

in some detail [34-36]. Although, Mott [37] suggested that for pure liquid transition metals, an *s-d* transition model used in solid crystal is appropriate but with different mean free paths for the *s-p* and *d* electrons, recent studies [38-42] have focused on finding the most suitable electron-ion pseudopotential matrix element that best describes a particular transition metal in the case of NFE.

The electrical resistivity of solid transition metals generally decreases with increasing P, as the amplitude of phonon vibrations, which induces electron scattering decreases with increasing P. However, the P-dependent electrical resistance of Zn [43, 44] showed an initial decrease to a minimum at ~10GPa, followed by a smooth increase to a maximum at ~20GPa. The anomaly in the P-dependent resistance behavior correlates with a change in the electronic density of states [44] with increasing P. In addition, high P Mossbauer studies [45, 46] observed a transition in the electronic topological structure of Zn with increasing P. Results of Mossbauer's studies appears to correlate with the observed change in the density of states with increasing P. Experimental study by Lynch and Drickamer [43] demonstrated a correlation of the minimum and maximum in the P-dependent resistance with an anomaly in the c/a ratio with increasing P. Nonetheless, given that both recent experimental and theoretical studies [10, 11] have observed the absence of anomaly in the c/a ratio with increasing P, it seems the observed anomaly in the P-dependent resistance results from the change in the electronic density of states and not thermodynamically induced.

The understanding of the effect of P on the electrical transport of a metal generally requires an understanding of the way in which the P affects its Fermi surface. Under hydrostatic pressure, the atomic volume decreases while the volume of the Fermi surface with the BZ increases [47]. Generally, changes also take place at any intersections of the Fermi surface with the BZ. For an anisotropic compressible crystal structure like Zn, a change in the BZ can lead to an appreciable change in the area of the Fermi surface sections [47-50]. With increasing P, the spin-orbit splitting

gap, which lifts the degeneracy in the BZ [51], decreases. When pressure is high enough to cause magnetic breakdown, electrons can tunnel from one orbit to another [52, 53], increasing electron mean free path and lowering electrical resistivity.

Desai et al. [54] have compiled the electrical resistivity dependence on T of solid and liquid Zn at 1atm measured by different authors. At T above 0K, thermal vibrations of the lattice reduces the mean free path of an electron by increasing the probability of phonon-induced electron scattering. Though Bloch theory predicts that the resistivity of a metal is approximately proportional to the absolute T above the Debye T, there are deviations at very high T due to thermal expansion. In the NFE model, the Fermi surface is a single sphere [55] with uniform density of states in *k*-space, which varies as a function of the radius of the sphere. With increasing T, the electrical resistivity behavior of liquid Zn is anomalous as it has a minimum in its T-dependent resistivity. From x-ray and neutron diffraction experiments, the T-variation of the distribution function of the liquid ions with the radius of the Fermi sphere [53, 55] accounted for the T-dependence of liquid resistivity of Zn. Above the melting T, the complete destruction of the hybridization of the *sp-d* bands leads to an increased density of conduction electrons [56]. This dominates over the increasing phonon-induced scattering effect due to the increasing lattice vibration amplitude with increasing T, and thus explains the decrease resistivity. Once the dehybridization-mediated release of *s* electrons is complete with two *s* electrons per atom, then the liquid resistivity displays a minimum as T-dependent phonon scattering leads to increased resistivity as T increases.

A recent calculation [57, 58] predicted that the electrical resistivity of metals with a filled *d*-band state such as Zn would be constant along its P-dependent melting boundary. In order to investigate further the effects of P on the electrical resistivity of Zn in the solid and liquid states,

and to test experimentally the predicted invariance of resistivity along its P-dependent melting boundary, the electrical resistivity of solid and liquid Zn up to 5GPa were measured in this study.

3.1. Experimental Details

The experiments were carried out in a 1000-ton cubic anvil press [59] with a capability of manually controlled heating rate. Shown in Figure 3.1 is the four-wire resistivity measurement technique and the cubic pressure cell design. A cubic press with three pairs of opposing anvils in mutually orthogonal directions is normally limited to two cube faces to make resistivity measurements at high P and T conditions. Using one pair of cube faces dedicated to the heater, and another pair needed for T measurement, a straightforward 4-wire electrode resistivity system was not possible. Adopted solution was to use the W5%Re-W26%Re thermocouples as temperature sensors in one mode and 4-wire electrode in another mode. In temperature mode, the thermocouple EMF's at the top and bottom of the sample was measured. While in resistance mode, a switched circuit passed a constant current of 0.2A (Keysight B2961A power source) through the W5%Re leads and sample and the voltage drop measured using the W26%Re leads while the switch was in resistance mode. A polarity switch reverses the current direction, which enabled any associated systematic errors in the voltage drop of the sample from the thermoelectric voltage between the sample and the electrodes corrected.

Pyrophyllite was used as the P-transmitting medium and the sample pressure was determined from hydraulic oil pressure using prior unpublished calibrations similar to those previously described [59, 60]. The junctions of the W5%Re-W26%Re thermocouples, which also served as electrodes, were in direct contact with the ends of the wire sample. The Zn wire (99.99% purity from Alfa Aesar) sample dimensions were 0.55 mm on average in diameter, measured at different widths, and 1.4mm in length. The sample length was 0.05mm longer than the boron

nitride (BN) sample container, which provided good thermocouple/electrode-sample contact. A preheating cycle up to 100K before melting T performed in each run P enhanced sample-electrode contact, which reduced the contact resistance contribution to the measured resistance to approximately zero. A cylindrical zirconia (ZrO_2) sleeve and two ZrO_2 disks placed on top and bottom of the sample container provided thermal insulation. The high compressibility of BN, which was used to contain the thermocouples, provided a tight seal at the metal–ceramic interface which helped in constraining the liquid above the melting T. A cylindrical graphite sleeve outside the sample container acted as a heat source when a high alternating current passed through it.

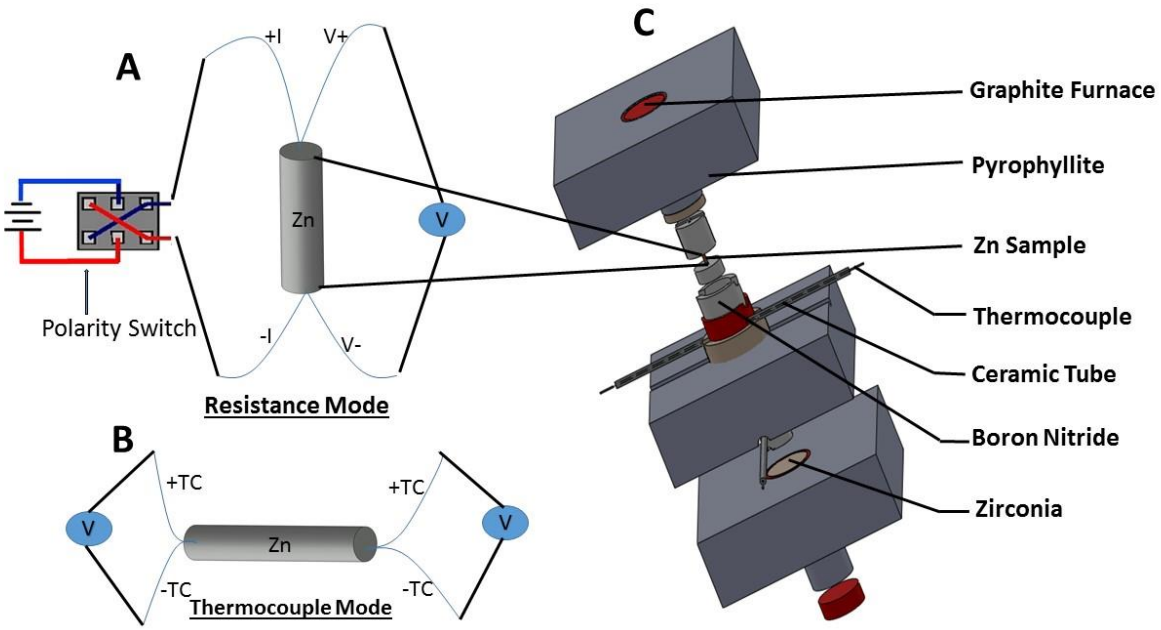

Figure 3.1. (A) Four-wire probe electrical resistivity design with current polarity switch and voltmeter (V). (B) Thermocouples measuring the temperature on top and bottom of the sample. (C) SolidWorks^{TM} design of the high-pressure cell with the components parts.

The mean voltage of the measured voltages in both current directions was computed at each temperature. A Keysight 34470A data acquisition meter, operating at a frequency of 20Hz with 1μV resolution, acquires measurements at 50K intervals in the solid state and at 20K interval

in the liquid state. The measurement interval in the liquid state decreased to 20K enabled enough data needed to define a slope before the likely chance of sample geometry change. The sample resistance at each temperature were calculated using Ohm's law, $R = \frac{V}{I}$, where R is resistance, V is voltage drop acquired from measurements and I is current. In a direction parallel to the radial axis of the cylindrical graphite heater, the ground recovered P cell exposed the middle section of the sample, after each run. Using a Nikon SMZ2800 microscope, the length and diameter of the exposed sample were carefully determined at several locations and the average computed. By incorporating the recovered sample geometry into Pouillet's law, $\rho = \frac{RA}{l}$, where l and A are sample length and cross-sectional area, respectively, the sample resistivity (ρ) was calculated. The chemical composition of the recovered sample and electrodes was analyzed by wavelength dispersive X-ray spectroscopy using a JEOL JXA-8530F field-emission electron microprobe. An accelerating voltage of 20kV, a probe current of 50nA, and a spot size (~100 nm) beam were used for all analyses in this study.

3.2. Results and Discussion

The T-dependent electrical resistivity measurements of Zn at P in the range 2-5GPa and at T up to 300K above melting T are shown in Figure 3.2. In comparison with the 1atm experimental data compiled by Desai et al. [54], high P data measured in this study show very good agreement both in the solid and liquid states. The onset of the solid-liquid phase transition marks an abrupt

increase in resistivity of Zn as clearly shown in Figure 3.2.

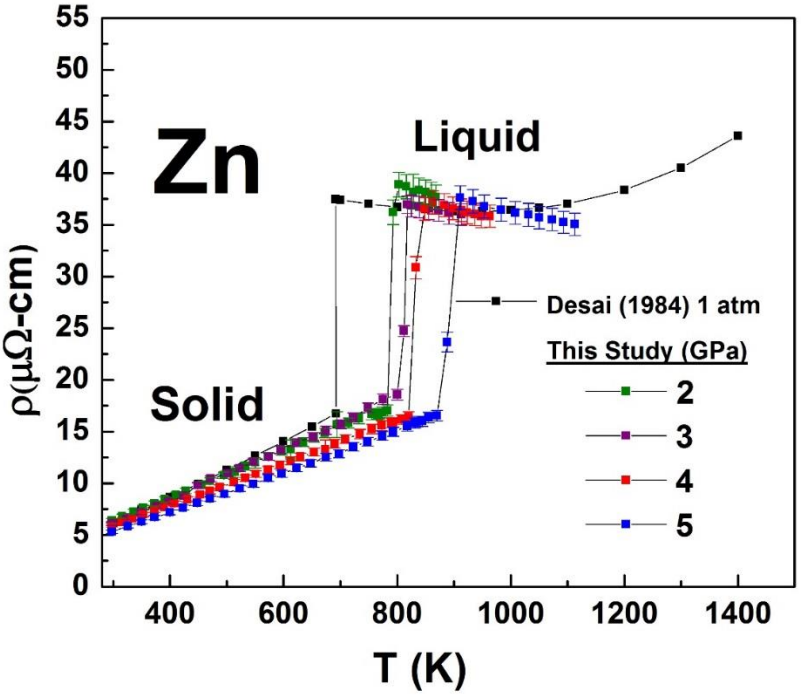

Figure. 3.2 Temperature dependence of electrical resistivity of Zn at fixed pressures compared with 1atm experimental data compiled by Desai et al. [54].

The melting T at a fixed P was determined by taking the average of the T measured at the start and completion of melting. Melting T determined in this study at a fixed P in this way agrees well with previous melting curve experimental studies determined by differential thermal analysis up to 5GPa [61], by electro-resistance method up to 5GPa and 12GPa [62, 63], and by infra-red pyrometry method up to 25GPa [64] as shown in Figure 3.3. Although the position of the thermocouples were ~0.7mm away from the central and hottest part of the sample, stabilization of the T before measurements allowed for thermal equilibration in the sample which improved the accuracy of the determined melting T.

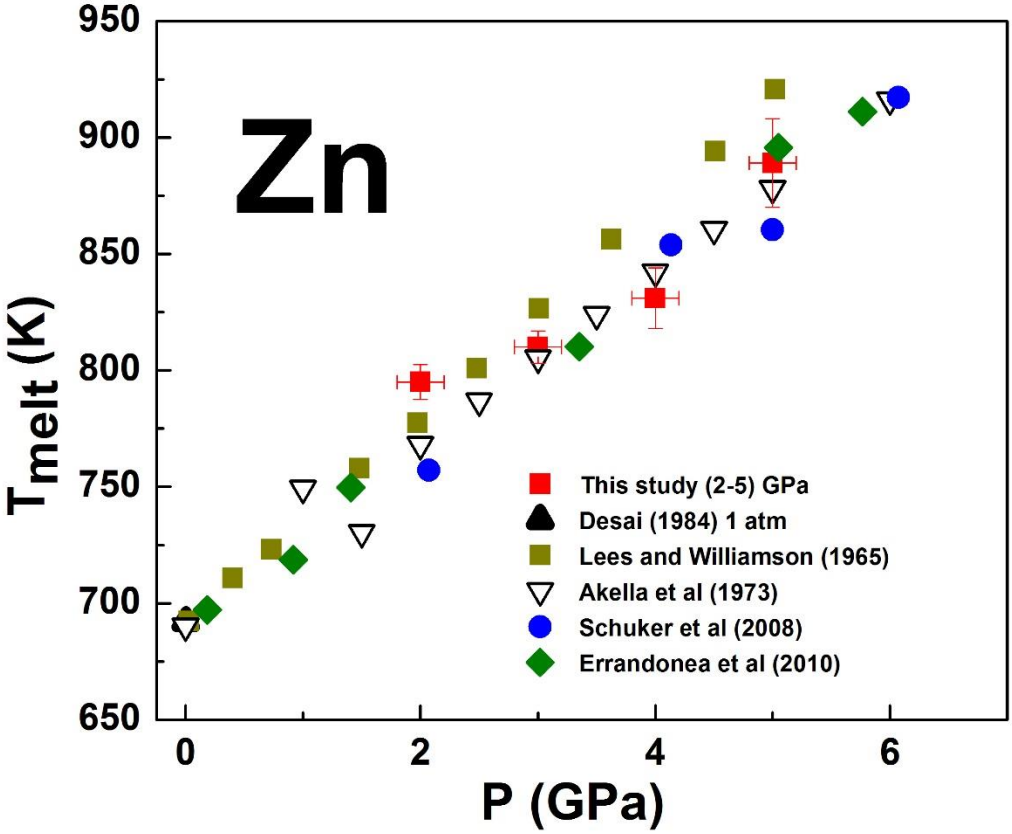

Figure 3.3. Melting curve of Zn up to 5GPa, determined by the jump in resistivity in this study, compared with previous experimental studies.

Although strict adherence to one experimental procedure measurements and with one type of cube assembly, the geometry of successive sample assemblies are never the same after exposure to high P and high T. This requires correction by careful inspection of the recovered sample and measurements of the geometry under microscopy as shown in Figure 3.4B. It is evident from microprobe analyses of the recovered sample shown in Figure 3.4C that there is no contamination of the sample either by the electrode/thermocouple or sample container.

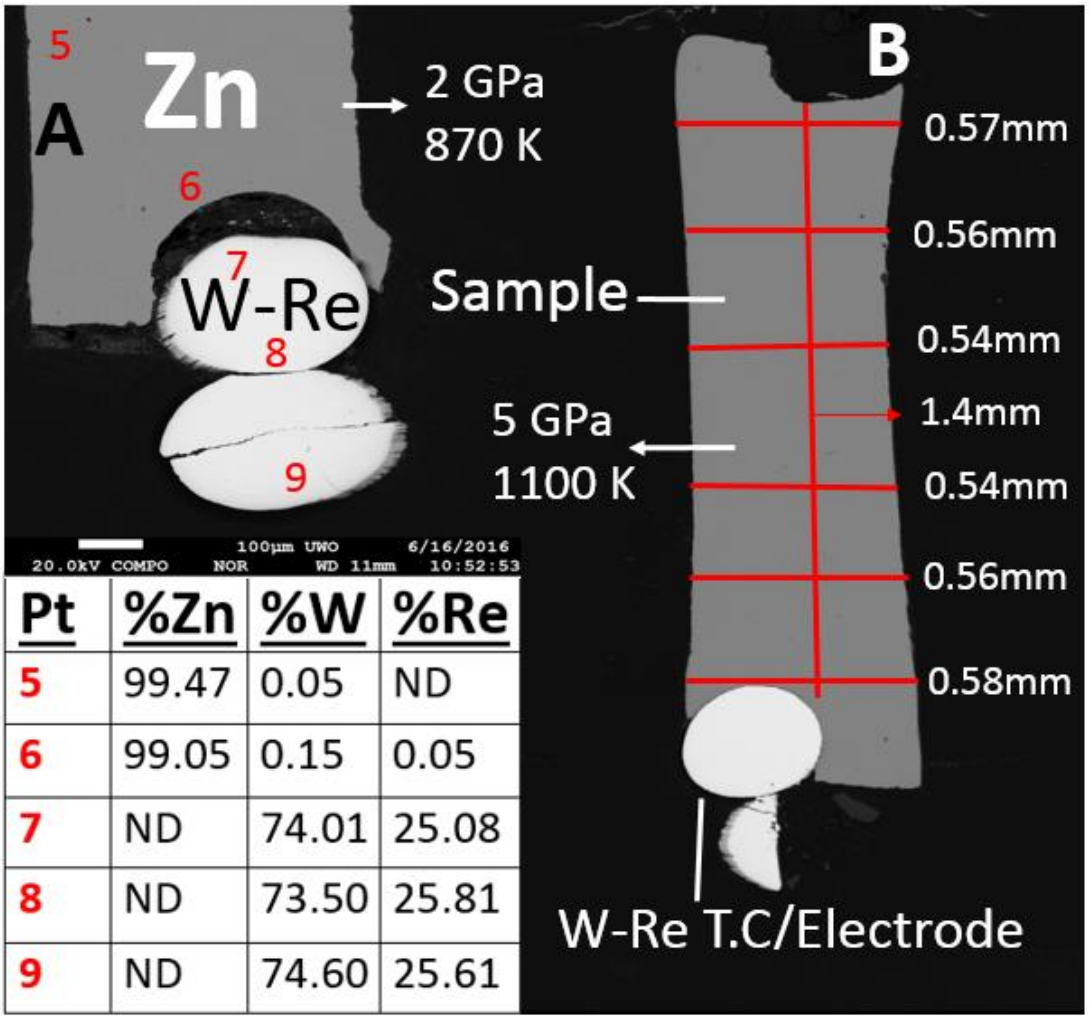

Pt	%Zn	%W	%Re
5	99.47	0.05	ND
6	99.05	0.15	0.05
7	ND	74.01	25.08
8	ND	73.50	25.81
9	ND	74.60	25.61

Figure 3.4. (A) Post-mortem view of a sectioned pressure cell recovered from 5GPa and 1100 K. Thermocouple/electrodes were W5%Re and W26%Re. Measurements of the length and width at several locations of the ground Zn sample are labelled. (B) Back scattered electron image of a sample recovered from 2GPa, 870K along with tabulated electron microprobe results of probe points 5-9.

The P-coefficient of resistivity of Zn decreases slightly in the solid with increasing pressure as shown in Figure 3.5 at 300K and 500K isotherms. With increasing P, the amplitude of the phonon vibration decreases and hence lowers the resistivity. Under compression, the components of the Fermi surfaces, the "cigar" and butterfly near the symmetry point *L* and the "needle" near the symmetry point *K* of the BZ, which were absent at ambient conditions, appear at different corresponding P [13, 16, 18]. The change in the electron density of states caused by the appearance

of these components with increasing P has been associated with the minimum and maximum observed in the solid-state P-dependence of resistivity [43, 44] around 10GPa. Due to the divalent nature of Zn, the total volume of the hole-sheet should ideally be equal to the total volume of the electron sheets [15]. However, spin-orbit interaction influences more the energy bands at *K* symmetry compared to other symmetry points [15, 16]. Within the central region of the crystal structure of Zn, the spin orbit splitting is negligible and vanishes at the center of the hexagonal face. If P is enough to cause magnetic breakdown, electrons upon approaching the spin orbit split boundary can tunnel through and jump to another orbit [52, 53]. Hence, the tunnelling effect increases the electron mean free path and lowers resistivity. With increasing P, the interaction of the *d*-electrons in the filled *d*-band with the *s* conduction electrons through hybridization [65] could increase and hence, high resistivity. However, if the proposed covalent bonding in the basal plane [30], which accounted for the anisotropy in the T- dependent volume expansion of Zn [66], applies, then with increasing P, the coordination of the covalent network could increase [30], which will contribute a term that will favor a decreasing resistivity. Over all, the integrated effect of reduced lattice vibration amplitude, the reduction/closing of spin orbit gap, *sp-d* hybridization effect and possible covalent bonding variation with increasing P results in a lower resistivity in the solid state of Zn up to the P range reached in this study.

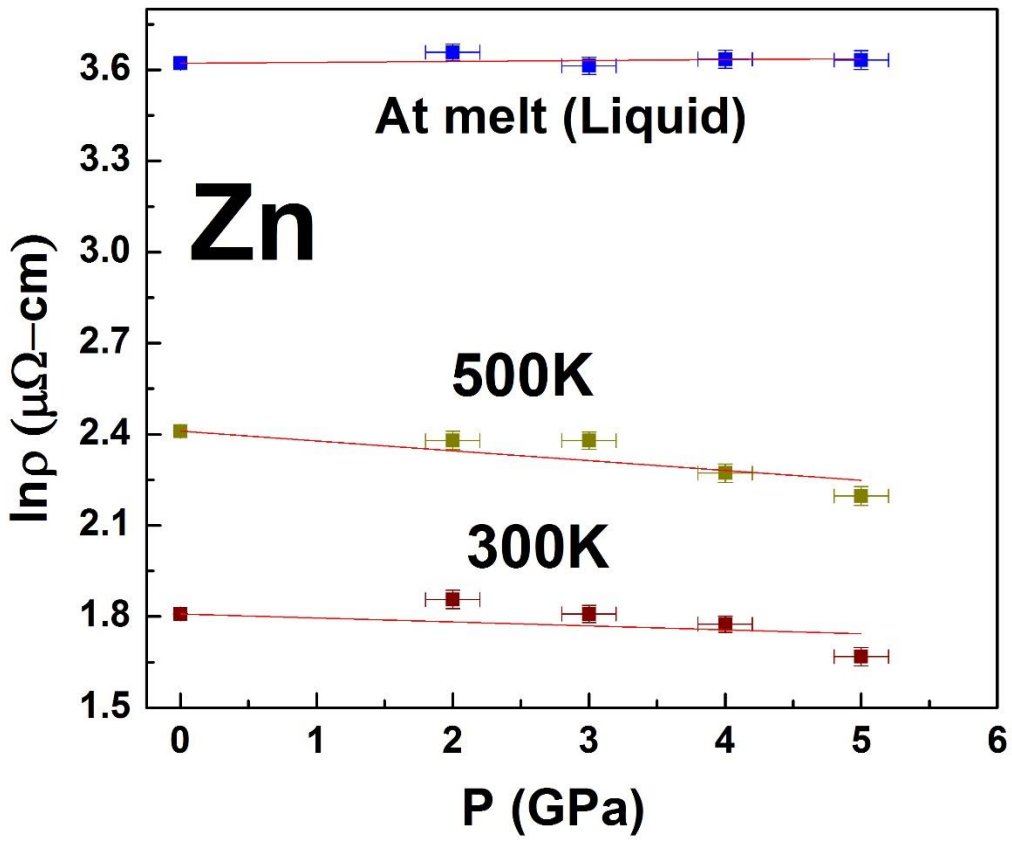

Figure 3.5. Pressure dependence of electrical resistivity of Zn at Isotherms 300K, 500K and at melt. The calculated slope of the fitted lines are (-0.013 $\pm$ 0.009 GPa^{-1}), (-0.032 $\pm$ 0.007 GPa^{-1}) and (0.002 $\pm$ 0.005 GPa^{-1}) respectively.

The resistivity at the solid-liquid phase transition increases by ~2.3 times as shown in Figure 3.2. On melting, the atoms vibrate about their non-equilibrium mean position which itself undergoes displacement, but maintains a short-range order structure. From the Ziman NFE model [32, 33], which accounts very well for the resistivity of liquid metals provided that the matrix of the pseudopotential is known, the relative change in resistivity during melting is caused by the change in the radial distribution function of the ions. The change in the electrical resistivity upon melting correlates with Lennard-Jones and Devonshire [67] order-disorder melting theory. In this model, the interatomic forces control the energy change required to transfer an atom from its

position to an immediate neighbour position on the same lattice. Melting occurs as a result of a change in the interatomic forces which translate to a change from long range ordered structure to a short range order. The interatomic forces between the atoms achieved at melt controls the dynamics of the ions, which in turn governs the resistivity on melting and in the liquid state. In Zn, there is an associated partial destruction of *sp-d* hybridization and any associated covalent bonding network at the onset of melting, leading to an increased density of sates of the conduction electrons [30, 33]. Knight et al. [68] have experimentally observed the increase in density of states of conduction electrons, in the T-dependent Knight shift investigation on Cd. As expected, the T-dependent Knight shift in Zn would mimic that of Cd, since Cd is an electronic analog to Zn. Other studies have demonstrated an increased density of states of *s* electrons on melting of Zn as reviewed by Busch and Güntherodt [69]. In addition, the relaxation effects of the zone boundary scattering, as the electronic structure approximates a NFE system, contributes to an increased electron mean free path and also lower resistivity on melting. On the other hand, due to the presence of imperfections in the hybridization and in the covalent network which is partially destroyed on melting, the conduction electrons still experience scattering [27, 30], which contribute in enhancing resistivity at the onset of melt. Similarly, the presence of possible spin-orbit interaction in the liquid state, contributes as well to increased resistivity on melting. Experimental study [56] found that the spin orbit effect, in the case of liquid Cd, contributes about 0.7% of the liquid resistivity and the effect in the case of Zn is estimated to be lower since Zn has a lower atomic number.

With increasing T in the liquid, the increasing destruction of the hybridization causes an increasing density of states of the *s* electrons, which dominates over the increasing phonon-induced *s-s* scattering processes. Thus, cause an initial decrease in resistivity with increasing T. Once the

destruction of the hybridization and the release of *s* electrons is complete giving room for two *s* electrons per atom, the T-dependent liquid resistivity displays a minimum and with further increasing T phonon-induce scattering dominates, leading to increase resistivity as observed in Figure 3.2.

Shown in Figure 3.6, the T-coefficient of resistivity $(d\ln\rho/dT)_P$ in the liquid state and at three temperature ranges in the solid state obtained in this study are plotted versus P and are compared with 1atm studies. Considering that the P range reached in this study is below the expected observed minimum in the P derivative of resistivity of about 10GPa [43, 44], the T-coefficient of resistivity is expected to be in general agreement with the 1 atm data as observed in this study.

The P-coefficient of resistivity on the melting boundary, $(d\ln\rho/dP)_{melt\ boundary}$, is 0.002 $\pm$ 0.005 GPa^{-1} as determined from the plot in Figure 3.5. Within the limit of error, the P-coefficient of resistivity on the melting boundary is zero. This suggests that with structural disorder that accompanies melting the integrated effects of P and T on the electrical resistivity on melting of Zn is constant along its P-dependent melting boundary up to 5 GPa. The antagonistic effect of P and T on the *sp-d* hybridization, spin-orbit splitting and Fermi surface topology, the respective resistivity decrease and increase with P and T appears to compensate each other at the melting boundary. The determined P-coefficient of resistivity, by least square fitting data in Figure 3.5, at 500K and 300K isotherm, $\left(\frac{\partial \ln \rho}{\partial P}\right)_{500K}$, and $\left(\frac{\partial \ln \rho}{\partial P}\right)_{300K}$, are -0.032 $\pm$ 0.007 GPa^{-1} and -0.013 $\pm$ 0.009 GPa^{-1} respectively. Comparison of these values was made with the values calculated using the relationship derived by Stacey and Anderson [57]:

$$\left(\frac{\partial \ln \rho}{\partial P}\right)_T = \frac{-2(\gamma - 1/3)}{K_T} \quad (1)$$

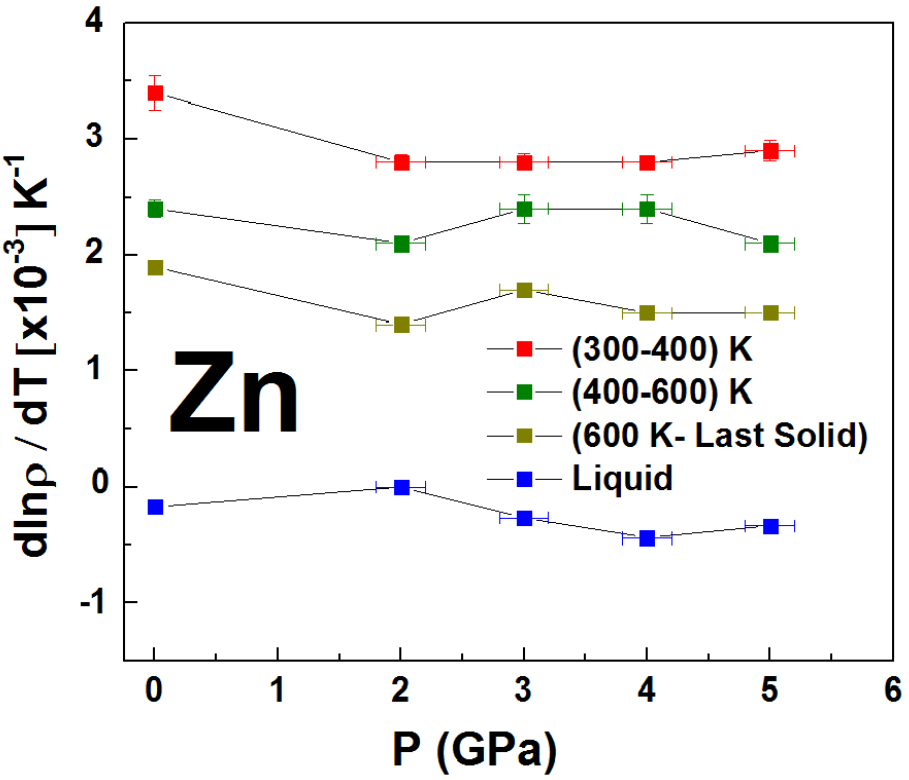

Figure 3.6. The T coefficient (dlnρ/dT) of electrical resistivity plotted for liquid Zn and three temperature ranges in solid state for P range of 2-5GPa. Comparison is made with the dlnρ/dT derived from 1atm data of many studies as compiled by Desai [54].

where γ is the Grüneisen parameter and K_T is the isothermal bulk modulus. γ was estimated to be 2.0 for solid Zn at 500K from the room T measurement of 2.03 by Rao [70] and applying T-dependence of γ calculated by Singh [71]. With a K_T value of 70GPa and 75GPa at 500K and 300K, respectively [70], values of -0.047GPa^{-1} and -0.045 GPa^{-1} for $\left(\frac{\partial \ln \rho}{\partial P}\right)_{500K}$, and $\left(\frac{\partial \ln \rho}{\partial P}\right)_{300K,}$ respectively were calculated from Eqn (1). The calculated P-coefficient of resistivity $(d\ln\rho/dP)_{500K}$ and $(d\ln\rho/dP)_{300K}$, using Eqn (1) is about 1.4 and 3.5 times higher than experimentally determined values respectively. However, determined $(d\ln\rho/dP)_{melting}$

boundry in this study compared well with the zero value predicted by theory [57, 58], which supports the conclusion that the P-dependent electrical resistivity of Zn at the melting boundary is constant.

Understanding thermal conductivity *(k)* of metals at P and/or T conditions is fundamental to the understanding of microscopic theories that predict the variations of *k* at these conditions. The difficulty with the experimental determination of *k* is with establishing and maintaining a controlled small T gradient. The challenge is even greater in measuring *k* of a liquid metal where convection and chemical contamination of the sample by the sample container is highly possible. The total *k* in a metal comprises contributions from the electronic and the phonon components. Above the Debye T, the electronic component dominates over the phonons. Notably, the electronic component of thermal conductivity k_e can be determined through Wiedemann-Franz law [72], $k_e = \frac{LT}{\rho}$, where L is the Lorenz number and ρ is the electrical resistivity. The Lorenz number L for solid and liquid Zn approaches the Sommerfeld value $L_o = 2.445 \times 10^{-8} \frac{V^2}{K^2}$, at high T above the Debye T of value 327K for the case of Zn [73]. On the other hand, experimental study of P-variation of k_{total} and L of Zn by Jacobsson and Sundqvist [74] up to 2GPa at room T indicates that both k_{total} and L increases with increasing P with a P-coefficient of 8.7×10^{-2} GPa^{-1} and 1.5×10^{-2} GPa^{-1} respectively. Using the Wiedemann-Franz law with the Sommerfeld value of L, k_e was calculated from the electrical resistivity data measured in this study, as shown in the T-dependence of k_e at fixed P values in Figure 3.7. Comparison of results of k_e determined in this study with those calculated using the 1atm electrical resistivity data of Desai et al. [54] were made. As anticipated, k_e decreases with increasing T in the solid state. On melting, it decreases to ~2.3 times of its solid-state value and increases with T in the liquid state. With increasing P, k_e increases both in the solid and liquid state. Also plotted on Figure 3.7 for comparison are the recommended values of k_{total} at

1atm from experimental studies as compiled in Touloukian et al. [75]. The 1atm experimental values of k_{total} are comparable with the values of k_e calculated from the measured electrical resistivity data using the Wiedemann-Franz Law. The general agreement between measured k_{total} and calculated k_e demonstrates that the Sommerfeld value of the Lorenz number is valid for Zn in both solid and liquid state.

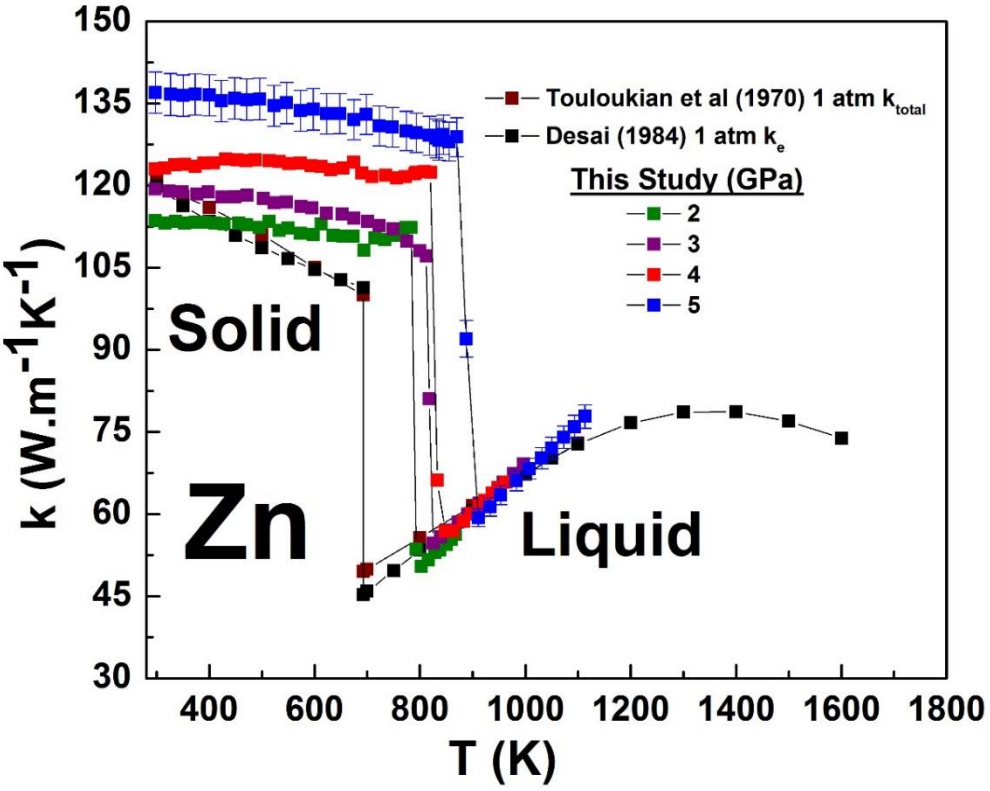

Figure 3.7. Temperature dependence of the electronic component of thermal conductivity at various pressures calculated from electrical resistivity data using the Wiedemann-Franz law and Sommerfeld value($2.445 \times 10^{-8} \frac{V^2}{K^2}$) of the Lorenz number. Represenatative error bars are shown for the 5GPa dataset. Comparison is made with the electronic thermal conductivity based on Desai et al. [54] resistivity data at 1 atm and with the total thermal conductivity from experimental measurements of Touloukian et al. [75].

The P-dependence of k_e is plotted at isotherm 500K and at melt as shown in Figure 3.8. P-coefficient of k_e, $\left(\frac{\partial \ln k_e}{\partial P}\right)_{melt}$ of 0.056 $\pm$ 0.002 GPa^{-1} and $\left(\frac{\partial \ln k_e}{\partial P}\right)_{500K}$ of 0.038 $\pm$ 0.005 GPa^{-1} were determined from the data obtained in this study. These values were compared with the same parameter calculated using the relationship derived by Bohlin [76] as shown in Eqn (2).

$$\left(\frac{\partial \ln k_e}{\partial P}\right)_T = \frac{(2\gamma - 1/3)}{K_T} \qquad (2)$$

A value of 0.052 GPa^{-1} was calculated for $(\partial \ln k_e/dP)_{500K}$ from Eqn (2). The prediction of $(\partial \ln k_e/dP)_{500K}$ by Eqn (2) is about 1.4 times higher than that determined value in this study.

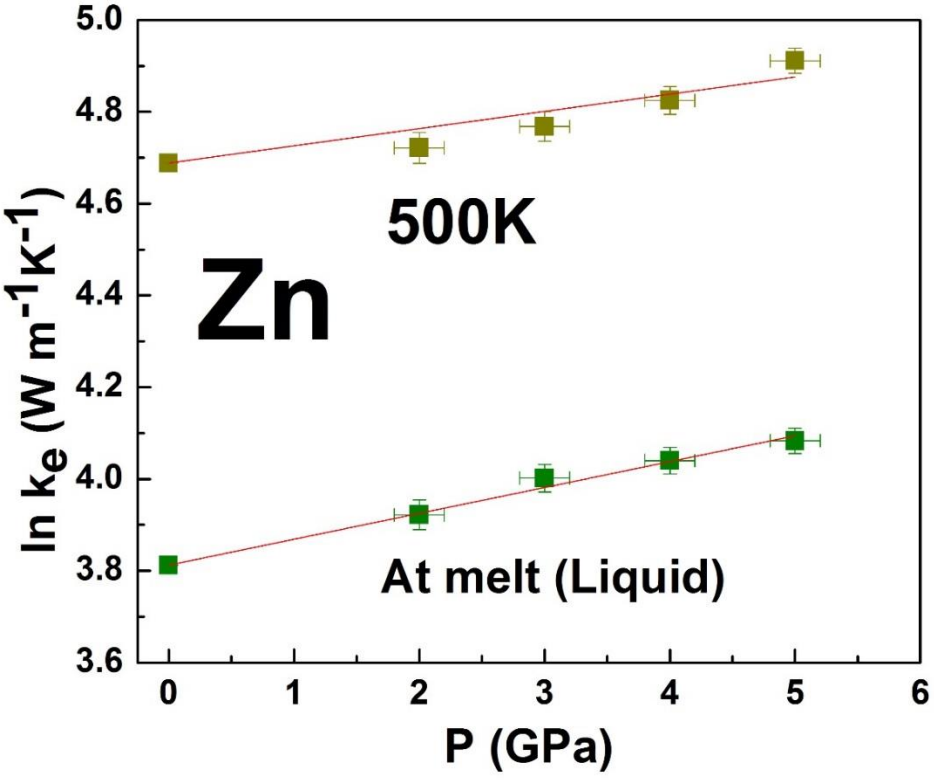

Figure 3.8. P-dependence of thermal conductivity k_e of Zn at 500K and along the melting boundary. The calculated slopes for the pressure coefficient of electronic thermal conductivity k_e, of the fitted lines are $(d\ln\rho/dP)_{\text{melt boundary}}$ = (0.056 $\pm$ 0.002) GPa^{-1} and $(d\ln\rho/dP)_{500K}$ = (0.034 $\pm$ 0.005) GPa^{-1}.

Experimental results from this research suggest that although electron mobility decreases with T on the melting boundary and with structural disorder that accompanies melting, the integrated effects of increasing P on k_e on melting results in an overall increase in k_e along the melting boundary. Calculation of $(\partial \ln k_e/dP)_{melt}$ with Eqn (2) is not possible since the T is not constant along the P-dependent melting boundary.

3.3. Conclusion

The T variation of the electrical resistivity of Zn above the melting boundary has been investigated up to 5GPa and results from this study demonstrated that the T-dependent resistivity of Zn is invariant along the melting boundary. These findings are interpreted in terms of the antagonistic effects of P and T on the electronic structure of liquid Zn as demonstrated in previous studies. Within experimental error, melting T determined at P values up to 5GPa are in agreement with previous experimental studies. The k_e was calculated using the Wiedemann-Franz law with Sommerfeld value of Lorenz function. With increasing P, k_e increased both in the solid and liquid state, however, k_e decreased with increasing T in the solid state and increased with T in the liquid state. Comparison of calculated *ke* and experimentally measured k_{total} at 1atm indicates that k_e really dominate over the phonon contribution in the T dependence of the k_{total} of Zn.

3.4 References

[1] Lifshitz, I. M. (1960). Anomalies of electron characteristics in the high pressure region. *Zhur. Eksptl'. i Teoret. Fiz.* 38.

[2] Schulte, O., A. Nikolaenko, and W. B. Holzapfel. (1991). Pressure-volume relations for Zn, Cd, Ga, In and TI at room temperature to 30 GPa and above. *International Journal of High Pressure Research* 6.3: 169-182.

[3] Takemura, K. (1995). Zn under Pressure: A singularity in the hcp structure at c/a= 3. *Physical Review Letters* 75.9: 1807.

[4] Takemura, K. (1997). Structural study of Zn and Cd to ultrahigh pressures. *Physical Review B* 56.9: 5170.

[5] Singh, D., and D. A. Papaconstantopoulos. (1990). Equilibrium properties of zinc. *Physical Review B* 42.14: 8885.

[6] Moriarty, J. A. (1974). Zero-order pseudoatoms and the generalized pseudopotential theory. *Physical Review B*, *10*(8), 3075.

[7] Schulte, O., and Holzapfel, W. B. (1996). Effect of pressure on the atomic volume of Zn, Cd, and Hg up to 75 GPa. *Physical Review B*, *53*(2), 569.

[8] Morgan, J. G., Von Dreele, R. B., Wochner, P., and Shapiro, S. M. (1996). Inelastic neutron scattering from single crystal Zn under high pressure. *Physical Review B*, *54*(2), 812.

[9] Takemura, K., Yamawaki, H., Fujihisa, H., and Kikegawa, T. (2002). High-pressure powder x-ray diffraction experiments on Zn at low temperature. *Journal of Physics: Condensed Matter*, *14*(44), 10563.

[10] Takemura, K., Yamawaki, H., Fujihisa, H., and Kikegawa, T. (2002). High-pressure x-ray studies of Zn at room and low temperatures with a He-pressure medium. *International Journal of High Pressure Research*, *22*(2), 337-341.

[11] Steinle-Neumann, G., Stixrude, L., and Cohen, R. E. (2001). Absence of lattice strain anomalies at the electronic topological transition in zinc at high pressure. *Physical Review B*, *63*(5), 054103.

[12 Harrison, W. A. (1962). Band structure and Fermi surface of Zinc. *Physical Review*, *126*(2), 497.

[13] O'Sullivan, W. J., and Schirber, J. E. (1966). Pressure dependence of the low-frequency de Haas—van Alphen oscillations in Zn. *Physical Review*, *151*(2), 484.

[14] Stark, R. W., and Falicov, L. M. (1967). Band structure and Fermi surface of zinc and cadmium. *Physical Review Letters*, *19*(14), 795.

[15] Auluck, S. (1973). Correlation between anisotropy in the normal-state mass renormalization and anisotropy in the superconducting energy gap for zinc. *Journal of Low Temperature Physics*, *12*(5-6), 601-629.

[16] Auluck, S., and Stark, R. W. (1976). Effect of changes in the lattice parameters on the Fermi surface of zinc. *Journal of Low Temperature Physics*, *25*(1), 219-224.

[17] Brennan, T. D., and Burdett, J. K. (1993). Electronic structure of elemental calcium and zinc. *Inorganic Chemistry*, *32*(5), 746-749.

[18] Kechin, V. V. (2001). Electronic topological transitions in Zn under compression. *Physical Review B*, *63*(4), 045119.

[19] Daniuk, S., Jarlborg, T., Kontrym-Sznajd, G., Majsnerowski, J., and Stachowiak, H. (1989). Electronic structure of Mg, Zn and Cd. *Journal of Physics: Condensed Matter*, *1*(44), 8397.

[20] Cohen, M. H., and Falicov, L. M. (1960). Effect of spin-orbit splitting on the Fermi surfaces of the hexagonal-close-packed metals. *Physical Review Letters*, *5*(12), 544.

[21] Alekseevskii, N. E., and Gaidukov, Y. P. (1963). Open cross sections of Cadmium, Zinc and Thallium Fermi surfaces. *Soviet Journal of Experimental and Theoretical Physics*, *16*, 1481.

[22] Joseph, A. S., Gordon, W. L., Reitz, J. R., and Eck, T. G. (1961). Evidence for spin-orbit splitting in the band structure of Zinc and Cadmium. *Physical Review Letters*, *7*(9), 334.

[23] Cohen, M. H., and Falicov, L. M. (1961). Magnetic breakdown in crystals. *Physical Review Letters*, *7*(6), 231.

[24] Juras, G. E., Segall, B., and Sommers, C. B. (1972). Electronic structure of zinc. *Solid State Communications*, *10*(5), 427-431.

[25] Daniuk, S., Jarlborg, T., Kontrym-Sznajd, G., Majsnerowski, J., and Stachowiak, H. (1989). Electronic structure of Mg, Zn and Cd. *Journal of Physics: Condensed Matter*, *1*(44), 8397.

[26] Singh, D., and Papaconstantopoulos, D. A. (1990). Equilibrium properties of zinc. *Physical Review B*, *42*(14), 8885.

[27] Jank, W., and Hafner, J. (1990). Structural and electronic properties of the liquid polyvalent elements. II. The divalent elements. *Physical Review B*, *42*(11), 6926.

[28] Fabian, D. J. (1968). Soft X-ray band spectra and the electronic structure of metals and materials. In *Soft X-ray Band Spectra and the Electronic Structure of Metals and Materialsls* (Vol. 1).

[29] Mosteller, L. P., Huen, T., and Wooten, F. (1969). Photoelectric emission from Zn. *Physical Review*, *184*(2), 364.

[30] Wallace, W. E. (1955). Bonding in the zinc family metals. *The Journal of Chemical Physics*, *23*(12), 2281-2294.

[31] Ballentine, L. E. (1966). Calculation of the electronic structure of liquid metals. *Canadian Journal of Physics*, *44*(11), 2533-2552.

[32] Ziman, J. M. (1961). A theory of the electrical properties of liquid metals. I: The monovalent metals. *Philosophical Magazine*, *6*(68), 1013-1034.

[33] Ziman, J. M. (1967). The electron transport properties of pure liquid metals. *Advances in Physics*, *16*(64), 551-580.

[34] Bradley, C. C., Faber, T. E., Wilson, E. G., and Ziman, J. M. (1962). A theory of the electrical properties of liquid metals II. Polyvalent metals. *Philosophical Magazine*, *7*(77), 865-887.

[35] Faber, T. E., and Ziman, J. M. (1965). A theory of the electrical properties of liquid metals: III. The resistivity of binary alloys. *Philosophical Magazine*, *11*(109), 153-173.

[36] Ashcroft, N. W., and Lekner, J. (1966). Structure and resistivity of liquid metals. *Physical Review*, *145*(1), 83.

[37] Mott, N. F. (1972). The electrical resistivity of liquid transition metals. *Philosophical Magazine*, *26*(6), 1249-1261.

[38] Evans, R., Greenwood, D. A., and Lloyd, P. (1971). Calculations of the transport properties of liquid transition metals. *Physics Letters A*, *35*(2), 57-58.

[39] Dreirach, O., Evans, R., Guntherodt, H. J., and Kunzi, H. U. (1972). A simple muffin tin model for the electrical resistivity of liquid noble and transition metals and their alloys. *Journal of Physics F: Metal Physics*, *2*(4), 709.

[40] Hirata, K., Waseda, Y., Jain, A., and Srivastava, R. (1977). Resistivity of liquid transition metals and their alloys using the t matrix. *Journal of Physics F: Metal Physics*, *7*(3), 419.

[41] Ononiwu, J. S. (1993). Calculation of electrical resistivity of liquid transition metals. P*hysica Status Solidi (b)*, *177*(2), 413-423.

[42] Shvets, V. T., Savenko, S., and Datsko, S. (2002). Perturbation theory for electrical resistivity of liquid transition metals. *Condens. Matter Phys*, *5*(3), 31.

[43] Lynch, R. W., and H. G. Drickamer. (1965). The effect of pressure on the resistance and lattice parameters of cadmium and zinc. *Journal of Physics and Chemistry of Solids* 26.1: 63-68.

[44] Garg, A. B., Vijayakumar, V., Modak, P., Gaitonde, D. M., Rao, R. S., Godwal, B. K., and Sikka, S. K. (2002). High-pressure resistance and equation-of-state anomalies in Zn: a possible Lifshitz transition. *Journal of Physics: Condensed Matter*, *14*(38), 8795.

[45] Potzel, W., Adlassnig, W., Moser, J., Schäfer, C., Steiner, M., and Kalvius, G. M. (1989). Zn 67 Mössbauer study of zinc metal at high pressure. *Physical Review B*, *39*(12), 8236.

[46] Potzel, W., Steiner, M., Karzel, H., Schiessl, W., Köfferlein, M., Kalvius, G. M., and Blaha, P. (1995). Electronically driven soft modes in zinc metal. *Physical Review Letters*, *74*(7), 1139.

[47] Brandt, N. B., Itskevich, E. S., and Minina, N. Y. (1972). Influence of pressure on the Fermi surface of metals. *Soviet Physics Uspekhi*, *14*(4), 438.

[48] Venttsel, V. A., Voronov, C. A., Likhter, A. I., and Rudnev, A. V. (1974). Effect of pressure on the Fermi surface of zinc. *Soviet Journal of Experimental and Theoretical Physics*, *38*, 1220.

[49] Templeton, I. M. (1974). The effect of hydrostatic pressure on the fermi surfaces of copper, silver, and gold. II. High precision studies. *Canadian Journal of Physics*, *52*(17), 1628-1634.

[50] Budarin, A. G., Ventsel, V. A., and Rudnev, A. V. (1978). Effective pressure on the Fermi surface of zinc. *Soviet Journal of Experimental and Theoretical Physics*, *48*, 858.

[51] Joseph, A. S., Gordon, W. L., Reitz, J. R., and Eck, T. G. (1961). Evidence for spin-orbit splitting in the band structure of Zinc and Cadmium. *Physical Review Letters, 7*(9), 334.

[52] Higgins, R. J., and Marcus, J. A. (1967). Magnetic breakdown in Zinc and its alloys as seen in the de Haas-van Alphen effect. *Physical Review*, *161*(3), 589.

[53] Van Dyke, J. P., McClure, J. W., and Doar, J. F. (1970). Theory of magnetic breakdown, g factor, and energy-band structure of Zinc. *Physical Review B, 1*(6), 2511.

[54] Desai, P. D., Chu, T. K., James, H. M., and Ho, C. Y. (1984). Electrical resistivity of selected elements. *Journal of Physical and Chemical Reference Data*, *13*(4), 1069-1096.

[55] Bradley, C. C., Faber, T. E., Wilson, E. G., and Ziman, J. M. (1962). A theory of the electrical properties of liquid metals II. Polyvalent metals. *Philosophical Magazine, 7*(77), 865-887.

[56] Kasowski, R. V., and Falicov, L. M. (1969). Calculation of the temperature dependence of the Knight shift in Cadmium. *Physical Review Letters*, *22*(19), 1001.

[57] Stacey, F. D., and Anderson, L. (2001). Electrical and thermal conductivities of Fe–Ni–Si alloy under core conditions. *Physics of the Earth and Planetary Interiors* 124.3: 153-162.

[58] Stacey, F. D., and Loper, D. E. (2007). A revised estimate of the conductivity of iron alloy at high pressure and implications for the core energy balance. *Physics of the Earth and Planetary Interiors* 161.1: 13-18.

[59] Secco, R. A. (1995). High p, T physical property studies of Earth's interior: Thermoelectric power of solid and liquid Fe up to 6.4GPa. *Canadian Journal of Physics*, *73*(5-6), 287-294.

[60] Secco, R. A., and Schloessin, H. H. (1986). On-line p, T calibration based on well-known phase transitions. *Journal of Applied Physics, 60*(5), 1625-1633.

[61] Akella, J., Ganguly, J., Grover, R., and Kennedy, G. (1973). Melting of lead and zinc to 60 Kbar. *Journal of Physics and Chemistry of Solids*, *34*(4), 631-636.

[62] Lees, J., and Williamson, B. H. J. (1965). Combined very high pressure/high temperature calibration of the tetrahedral anvil apparatus, fusion curves of Zinc, Aluminium, Germanium and Silicon to 60 kilobars. 278-279.

[63] Errandonea, D. (2010). The melting curve of ten metals up to 12 GPa and 1600 K. *Journal of Applied Physics*, *108*(3), 033517.

[64] Shuker, P., Melchior, A., Assor, Y., Belker, D., and Sterer, E. (2008). IR pyrometry in diamond anvil cell above 400 K. *Review of Scientific Instruments*, *79*(7), 073908.

[65] Shvets, V. T. (1982). Influence of sd hybridization of the electrical conductivity of liquid transition metals. *Theoretical and Mathematical Physics*, *53*(1), 1040-1046.

[66] Barron, T. H. K., and Munn, R. W. (1967). Analysis of the thermal expansion of anisotropic solids: application to zinc. *Philosophical Magazine*, *15*(133), 85-103.

[67] Lennard-Jones, J. E., and A. F. Devonshire. (1939). Critical and co-operative phenomena. III. A theory of melting and the structure of liquids. *Proceedings of the Royal Society of London. Series A, Mathematical and Physical Sciences*: 317-338.

[68] Knight, W. D., Berger, A. G., and Heine, V. (1959). Nuclear resonance in solid and liquid metals: A comparison of electronic structures. *Annals of Physics*, *8*(2), 173-193.

[69] Busch, G., and Güntherodt, H. J. (1974). Electronic properties of liquid metals and alloys. *Solid State Physics*, *29*, 235-313.

[70] Rao, R. R. (1974). Anderson-Grüneisen parameter δ of some hexagonal metals and MgO from third-order elastic-constant data. *Physical Review B*, *10*(10), 4173.

[71] Singh, R. N., Arafin, S., and George, A. K. (2007). Temperature-dependent thermo-elastic properties of s-, p-and d-block liquid metals. *Physica B: Condensed Matter*, *387*(1), 344-351.

[72] Franz, R., and Wiedemann, G. (1853). Ueber die wärme-leitungsfähigkeit der metalle. *Annalen der Physik, 165*(8), 497-531.

[73] Klemens, P. G., and Williams, R. K. (1986). Thermal conductivity of metals and alloys. *International Metals Reviews, 31*(1), 197-215.

[74] Jacobsson, P., and Sundqvist, B. (1985). Thermal diffusivity of Zinc as a function of pressure and temperature. *High Temperatures. High Pressures, 17*(1), 103-109.

[75] Touloukian, Y. S., Powell, R. W., Ho, C. Y., and Nicolaou, M. C. (1974). *Thermophysical Properties of Matter-The TPRC Data Series. Volume 10. Thermal Diffusivity*. Thermophysical and electronic properties information analysis center lafayette in.

[76] Bohlin, L. (1976). Thermal conduction of metals at high pressure. *Solid State Communications*, *19*(4), 389-390.

Chapter 4: Invariance of the Electrical Resistivity of Co along the Pressure Dependent Melting Boundary

4.0. Introduction

The magnetic field of the Earth has its origin in the Earth's core with a composition dominated by Fe with some Ni, this has attracted attention to the properties of ferromagnetic *3d* metals at high pressure (P) and temperature (T) conditions. Recently, both theoretical and experimental studies at core-relevant P and T conditions have resulted in revised estimates of electrical resistivity [1-7] which are lower than previously accepted values [8, 9]. These lower values of electrical resistivity require higher than expected values of thermal conductivity. Cobalt is a close analog to Fe and the understanding of the transport properties of these metals is important in understanding the origin and the sustainability of the Earth's magnetic field.

Magnetism and electrical resistivity in metals are governed by the valence electrons and as such makes the two quantities inseparable. Stoner [10] demonstrated a predictive model of the delocalized electron spin magnetisation by assuming an average spin field interacting with a single spin. This model was somewhat successful in predicting whether a given metal is ferromagnetic by characterizing the product of the Stoner parameter *(I),* which measures the strength of the exchange interaction, and the Density of States *(N)* of the electrons at the Fermi energy (E_f). From this criterion, a metal is ferromagnetic if $IN_{E_F} > 1$ or non-magnetic if $IN_{E_F} < 1$. This model was successful in predicting Fe and Ni to be ferromagnetic, however, it failed in the case of Co with a prediction of 0.972 [11, 12]. Interestingly, Ni is a weaker ferromagnet than Fe and Co and yet has the largest value of IN_{E_F} in this model. The T-dependent magnetic susceptibility and the electronic

specific heat of Fe, Co and Ni were also not successfully predicted in Stoner's model [13]. The model was derived from a parabolic band shape and does not consider the different shapes of *N* of different materials and their differences in the position of E_f within the band structure [12].

The origin of ferromagnetism in metals can be clearly understood from the foregoing differential shielding argument [12]. The concept of this model is rooted in Pauli's Exclusion Principle which forbids two electrons with the same magnetic quantum number from occupying the same state. An electron with a given spin experiences an effective electron density arising from the electron density of all the other electrons. However, an electron experiences an extra repulsion force from an electron with a similar spin in its neighbourhood, thus creating an exchange hole in an incompletely paired electron system. Thus, the spin-up (majority) and spin-down (minority) electrons experience differential shielding from the influence of the nucleus which then splits the band into two sub-bands. The spin bands associated with different types of electrons have differing spatial extents. Due to the influence of the nucleus, the lower lying spin band is more spatially contracted than the higher lying spin band and therefore, electron-electron repulsion is larger in the lower lying spin orbital [12]. The driving force for the spin polarization lies in the local anti-bonding of the states around the Fermi level in the event of splitting. The presence of the Fermi level in a strongly anti-bonding region after splitting results in a structurally unstable system which leads to redistribution of electrons that favours spin polarized direction to achieve a lower energy stable configuration, giving rise to magnetism. The filling of a lower bonding state at the expense of higher bonding state during the electron redistribution process leads to a magnetic P [14, 15] which in turn leads to a decrease in bulk modulus and volume dilation. The effects of magnetic P calculated for the case of Fe, Co and Ni [14, 16, and 17] were ~ 7% increase in volume and ~30% reduction in bulk modulus in Fe and Co but much less in Ni. As expected, the magnetic moment

of Co of 1.74 [18] lies between the value of Fe (2.2) [12] and Ni (0.62) [12]. The trend in increasing value of magnetic moment correlates inversely with the population of *3d* electrons. Ni, with the highest *d* electron has the smallest magnetic moment while Fe with the least *d* electrons has the highest magnetic moment. Similarly, the occupancy of the *3d* electron band correlates with the stability of the fcc phase in the phase diagrams of Fe, Co and Ni, where the highest occupied *d*-band has the widest stability range in fcc [19, 20]. Experimental studies at room T have shown that Co remains in the hcp structure to well over 100GPa, and in the range 105-150 GPa, hcp-fcc will coexist. Beyond 150GPa, the stable phase of Co is the non-magnetic fcc phase. Fe has the least number of *d* electrons and is only stable in fcc region at elevated T while Ni transforms from ferromagnetic fcc to non-magnetic fcc at ~250GPa [19-22].

The Fermi surfaces of the *3d* ferromagnets are experimentally and theoretically more complicated than those of other transition metals [23]. Studies using the de Haas-van Alphen (dHvA) technique [24-26] revealed a series of frequency branches corresponding to cross sectional areas of the Fermi surfaces that are two orders of magnitude smaller than expected for the principal sheets. From the study by Batallan et al. [25] on the Fermi surface of Co, the principal cross section of the spin-up Fermi surface consists of a quasi-hyperboloid centered about ΓA axis which consists of the neck and an anisotropic ball elongated along ΓA with protuberances of hexagonal symmetry in the (1010) directions. While the principal cross sections of the spin-down Fermi surface consist of three pockets centered on Γ, there is a multi-connected monster and a hole surface centered around *L* and composed of intersecting pockets due to degeneracy. It has been demonstrated that the spin-up Fermi surface of Co is analogous to that of the noble metals [27] while the spin down Fermi surface is analogous to Re, which has 7 valence electrons per atom while the minority sub-band of Co has 7.44 valence electrons per atom [28, 29]. Magnetoresistance measurements [30,

31] also revealed some of the low frequency branches, as well as established the existence of open orbits in the Co band structure due to the non–compensating nature of electrons and holes. In an uncompensated system of electrons and holes, the magnetoresistance saturates at high field [23]. The removal of spin degeneracy explains the fact that Ni, with atomic number (Z) of 28, is uncompensated from the general saturation of magnetoresistance and thus, has a well-defined Hall coefficient of -1. Similarly, hcp Co, with Z of 27, is also uncompensated, however its Hall coefficient has not been accurately determined. Fe, with Z of 26, exhibits a quasi-quadratic growth of the magnetoresistance for the general direction of induction which indicates compensated electrons and holes [23]. The presence of open orbits in the band structure of Co enhances resistivity as electrons are confined within an orbit like the case of the uncompensated electronic structure in Zn [31-35]. The interruptions of open orbit structure lead to a decreased mean free path of electrons. The open orbit contribution to liquid resistivity in the case of Cd and Zn has been demonstrated to be negligible, with a value less than 1% [36]. Inference is drawn that this value would not be anything too different in the case of Co that melts from fcc structure with less asymmetry.

The T-dependent electrical resistivity of a solid transition metal is generally understood through Mott's *s-d* scattering theory [37]. The conduction s electrons, which are more mobile than the conduction *d* electrons, can undergo both *s-s* and *s-d* scattering processes induced by phonons and magnons. The mobility of *s* electrons is higher than that of *d* electrons because of the higher effective mass of the *d* electrons. As *s* electrons are scattered into empty *d* states, their effective mass increases and their velocity decreases. Thus, resistivity increases as mobility decreases. The *s-d* scattering processes dominate over s-s scattering due to the high density of states of *d* bands which are unfilled in the case of Co.

With T rise at fixed P, solid state Co undergoes a martensitic type of crystal structural transformation from hcp to fcc at 695K [38]. Yoo et al. [20] suggested that the fcc high T paramagnetic phase and the high P fcc paramagnetic/non-magnetic phase of Co are electronically the same. At T below the Curie T, the spin fluctuation of the magnetic ordering induced scattering dominates over phonon scattering as shown by the upward curvature of T-dependent resistivity behavior. However, above the Curie T of ~1400K [39] at 1atm, the reverse is the case, because of change of long to short range magnetic ordering, the phonon induced scattering becomes dominant. The effect of T on the magnetic spin gap (i.e. the energy difference between the sub-bands) was investigated by dHvA methods to examine the energy shift on the dimensions of the Fermi surface of Fe which relates to the change in the spin gap [40]. Their result showed that the energy difference does not vary much with T. This is in contradiction to Stoner's model which predicted that the spin gap is proportional to magnetization and should decrease to zero at the Curie point. Thus, it is expected that Co will show similar characteristics of the small T effect on spin gap to Fe, since they both have similar electronic structure.

Upon compression, the amplitude of lattice vibration, magnetic spin gap and open orbit gap present in some symmetry directions decreases. A change in the spin gap, leads to a change in exchange interactions and electron redistribution between the spin sub-bands. The overflow of electrons from the majority to the minority spin sub-band because of electron redistribution leads to a decrease in the cross sections of the majority sub-band hole-pockets and an increase in the cross sections of the electron pockets in the minority spin sub-band [28]. The change in magnetic moment and the exchange interaction with increasing P are reflected in the change of saturation magnetization and in a shift in the Curie T, respectively. Experimental measurements up to 9GPa [41] have demonstrated that with increasing P, the Curie T of Co remains constant, however a

theoretical study [42] demonstrated a slight change in Curie T with P. This could suggest that P has minor influence on the spin gap of Co. The effects of P-variation on the magnetic ordering, change in the amplitude of phonon vibration, electronic density of states, and scattering processes, are all integrated in the P-dependent electrical resistivity.

The Modified Nearly Free Electron (MNFE) model [43, 44] has accounted well for the electrical resistivity of liquid non-simple transition metal by applying appropriate electron-ion pseudopotentials in the Nearly Free Electron (NFE) [45] model, with *d* resonance effects incorporated using a simple muffin-tin potential model [46, 47]. From the NFE model, the relative change in resistivity on melting is caused by the change in radial distribution function of the ions, called the structure factor, while the T-variation of liquid resistivity in the liquid state follows from the T-dependent Fourier transform of the radial distribution function of the liquid ions. Due to hybridization of adjacent *d* orbitals, the mobile s electrons spend longer time around the vicinity of the d virtual bound state (d-resonance effect) [46, 47] and as such leads to an overall delay in the propagation time of electron and increased resistivity. Although Mott [48], suggested that for the pure liquid transition metals a different model involving s-d transitions and with different mean free paths for *s* and *d* electron like solid state s-d scattering, no qualitative treatment after Mott has been pursued in the case of liquid transition metals drawn from intensive literature search.

Though semi-theoretical calculation [8] predicted electrical resistivity of both filled and unfilled *d*-band metals are constant along their P-dependent melting boundary, a later theory [9] predicted the opposite for unfilled *d*-band metals. To investigate further the effects of P on the electrical resistivity of an unfilled *d* band metal, both in the solid and liquid states, especially on its P-dependent melting boundary, the electrical resistivity of solid and liquid Co up to 5GPa was measured.

4.1. Experimental Details

A 1000-ton cubic anvil press was used in carrying out the high P, T resistivity experiments [50]. Illustrated in Figure 4.1 are the four-wire resistivity measurement technique and the cubic pressure cell design. The P-transmitting medium used was pyrophyllite and the sample P was determined from hydraulic oil P using prior unpublished calibrations like those previously described [49, 50].

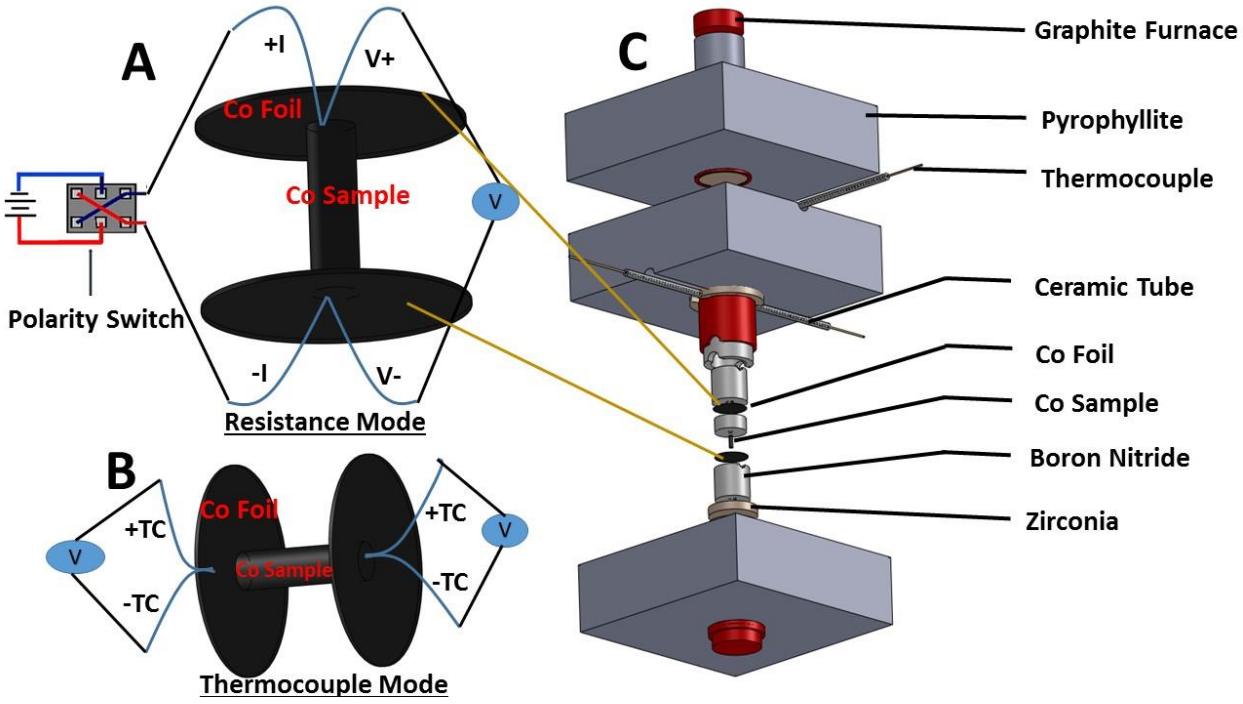

Figure 4.1. Schematic drawing of two modes (resistance (A) and temperature (B)) of measurement. (A) Four–wire probe design, showing the current polarity switch and the voltmeter for measuring the voltage drop across the sample. (B) Thermocouples measuring the temperature on top and bottom of the sample. (C) Exploded view (SolidWorks^{TM} design) of the high-pressure cell with components parts.

Four-wire resistivity measurement ideally requires two pairs of opposite faces of a cubic pressure cell. With one pair of cube faces dedicated to the heater, and another pair needed for temperature measurement, a straightforward four-wire electrode system was not possible. A technique using two pairs of Type C thermocouples as T sensors in one measurement mode and

four-wire electrodes in another mode was adopted. In T mode, the thermocouple EMF's at the top and bottom of the Co foil was measured. A constant current of 0.2A (Keysight B2961A power supply) was passed through the W5%Re leads by a switched circuit and measurement of the voltage drop was made using the W26%Re leads while the switch was in resistance mode. At every measured voltage drop, the current direction was reversed using a polarity switch which enabled any associated systematic errors in the voltage drop measured across the sample, arising from thermoelectric voltages between any metal junction or any other parasitic voltage, to be corrected. The mean voltage of the measured voltages in both current directions was computed at each temperature. A Keysight 34470A data acquisition meter, operating at a frequency of 20Hz with 1μV resolution, was used to make measurements at 50K intervals in the solid state and at 20K intervals in the liquid state. The measurement interval in the liquid state was decreased to acquire enough data needed to define a slope before the likely chance of sample geometry change.

The starting dimensions of the Co sample wire (99.99% purity, Alfa Aesar) sample were 0.53mm in diameter and 1.78mm in length. The junctions of the W5%Re-W26%Re thermocouples, which also served as electrodes in a four-wire arrangement, were in direct contact with the ends of the Co foil which formed part of the sample circuit. The main function of the two Co foils placed at the top and bottom of the sample was to reduce contamination from the thermocouple/electrode which was expected to occur in the sample liquid state. The foil dimensions were 4.57mm in diameter and 0.1mm thick. The foil diameter was ~ 9 times larger than the diameter of the sample and its thickness was ~6% of the sample length. Due to dimensional differences of the foil and the sample, the contribution of the foil resistance to the total resistance measured is negligible relative to the sample resistance. The sample length was 0.05mm longer than the sample container which was an alumina (Al_2O_3) ceramic tube which

provided good thermocouple/electrode-sample contact. A preheating cycle up to 1000K was carried out for every run P to enhance sample-electrode contact which reduced the contact resistance contribution to the measured resistance to approximately zero. The T was cooled down rapidly after preheating at a rate of 100K/s. A cylindrical zirconia (ZrO_2) sleeve and two ZrO_2 disks placed on top and bottom of the sample container provided thermal insulation. The high compressibility of boron nitride (BN), which was used to contain the thermocouples and the Al_2O_3 sample container, provided a tight seal at the metal–ceramic interface which helped in containing the liquid above the melting T. A cylindrical graphite sleeve outside the BN acted as a heat source when a high alternating current passed through it.

Ohm's law, $R = \frac{V}{I}$, where R is resistance, V is voltage drop measured across the sample, and I is current was used to calculate the sample and the foil resistance at each T. In a direction, parallel to the radial axis of the cylindrical graphite heater, the recovered P cell was ground to expose the middle section of the sample and the foil, after each run. A Nikon SMZ2800 microscope was used to measure carefully the length and diameter of the sample at several locations and the average was computed. By incorporating the recovered sample geometry into Pouillet's law, $\rho = \frac{RA}{l}$, where l and A are sample length and cross-sectional area, respectively, the sample resistivity (ρ) was calculated. The chemical compositions of the recovered sample and electrodes were determined by wavelength dispersive X-ray spectroscopy using a JEOL JXA-8530F field-emission electron microprobe. An accelerating voltage of 20kV, a probe current of 50nA, and a spot size (~100nm) beam were used for all analyses.

4.2. Results and Discussion

Back-scattered electron images of samples, recovered from 1830K at 3GPa, for the sample bottom and sample top regions, showing microprobe points, are shown in Figures 4.2B and 4.2C, respectively. The composition data shown in the table within Figure 4.2 demonstrate that the contamination from W and Re is limited to the Co foil region. The foil with its negligible contribution to measured resistance acts as a chemical buffer, impeding the dissolution of W and Re into the sample on melting. The purity of recovered samples as shown in Figure 4.2 gave confidence in the reliability of Co resistivity values for the liquid state.

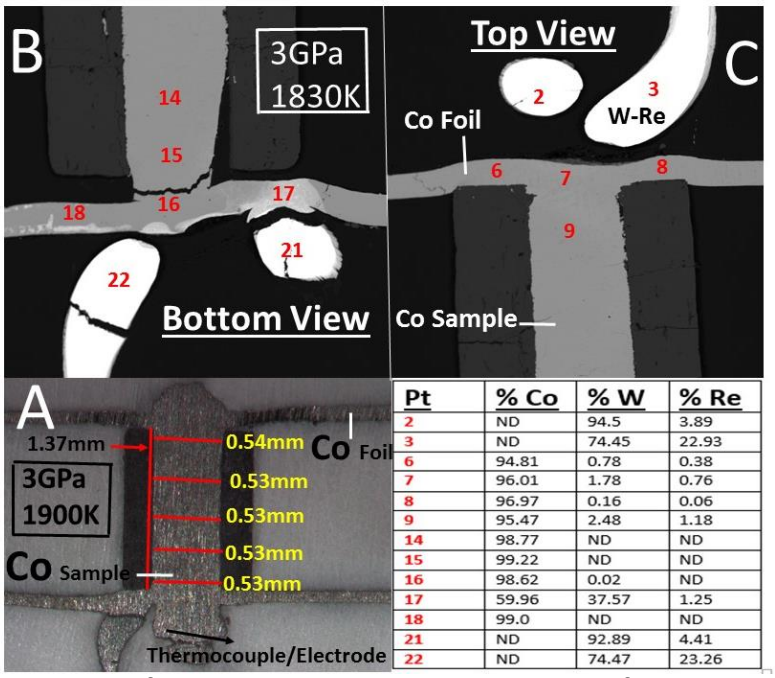

Pt	% Co	% W	% Re
2	ND	94.5	3.89
3	ND	74.45	22.93
6	94.81	0.78	0.38
7	96.01	1.78	0.76
8	96.97	0.16	0.06
9	95.47	2.48	1.18
14	98.77	ND	ND
15	99.22	ND	ND
16	98.62	0.02	ND
17	59.96	37.57	1.25
18	99.0	ND	ND
21	ND	92.89	4.41
22	ND	74.47	23.26

Figure 4.2. (A) Post-mortem view of a sectioned pressure cell recovered from 3GPa and 1900K. Thermocouple/electrodes were W5%Re and W26%Re. Measurements of the length and width at several locations of the ground Co sample are labelled. Back scattered electron image of a sample sectioned into two parts: Top (B) and Bottom View (C), recovered from 3GPa and 1830K. Tabulated electron microprobe results of probe points 2-22 points as labelled in (B) and (C).

Although measurements were made with one type of P-cell assembly and firm adherence to one experimental procedure was adopted in all experiments, there are unavoidable slight but

significant differences in the geometry between successive sample assemblies after exposure to high P and T. Because of this, careful inspection of the recovered sample and measurements of the diameter and length of the sample at different locations to obtain average dimensions were made under microscope as shown in Figure 4.2A. The computed averages were used as input into the calculation of the resistivity in the Pouillet equation.

The T-dependence of the electrical resistivity of Co in the P-range of 2-5GPa and T up to 100K above the melting T is shown in Figure 4.3. In comparison with 1 atm data by Laubitz and Matsumura measured up to 1700K [39] and Seydel and Fucke measured from 1200K to 2300K [51], measured high P data in this study show very good agreement above the Curie T and in liquid state. At T below the Curie T, measured data in this study are higher than the 1 atm data because of the effects due to preheating in this study experiments. The α-β transformation is a martensitic type and the T at which it occurs appears to be a function of purity, grain size and perhaps sample size [52]. However, on pre-heating up to 1000K, It is expected that much of the sample has converted to the fcc (β) phase. The fcc (β) $\rightarrow$ hcp (α) back transformation in Co is very sluggish [39]. Due to the rapid cooling rate in the preheating cycle after exposure up to 1000K, some amount of β phase, which is more resistive than the α phase, may have persisted at ambient T, resulting in a resistivity value higher than the 1 atm reference data. Though the measured resistivity trends mimic the 1 atm data, it was not possible to correlate clearly a change in the slope of T-dependent resistivity at fixed P with the α-β transformation point due to the sluggish behavior of the transformation. The T-dependent resistivity change in slope at ~1400K correlates with a change from a long range magnetic (ferromagnetic) to short range magnetic (paramagnetic) order. In the paramagnetic region, the contribution of the spin fluctuation effect in inducing scattering processes saturates, leaving the increasing phonon contribution to dominate the T-dependence of resistivity.

The change in electronic scattering is reflected in the change in the slope and curvature of the T-dependence of resistivity at the Curie point.

The abrupt increase in resistivity at ~1800K marks the solid–liquid transition in Co. The resistivity at the solid-liquid transition increases about 1.15 times as shown in Figure 4.3. In liquid metals, the atoms vibrate about their non-equilibrium mean position which itself undergoes displacement, but maintains a short range order. The electrical resistivity of liquid *3d* transition metals has been accounted for by the MNFE theory [46]. Güntherodt et al. [53] suggested that the jump in resistivity on melting in ferromagnetic metal is less than the jump in nonmagnetic metal such as Pd because of the presence of short range magnetic order which does not change significantly on melting [54]. They inferred this might be an indication that in the liquid state where the atomic disorder is rather large, the spin disorder contribution to the electrical resistivity of Fe, Co and Ni is still present but is not simply additive. Thus, it is expected that the positive contribution of magnetic ordering to thermal expansion through magnetic P [55], will contribute to the volume increment on melting. In liquid Fe, Co and Ni, there are not only s electrons but also bound *d* electrons and the contribution to the conductivity is due mainly to the s electrons [56]. From the MNFE theory, the *d*-resonance decreases the mobility of the dominant s conduction electrons as electrons with energy close to the resonance spend relatively longer time near the resonance [47], decreasing the mobility of the electrons and hence increased resistivity. Although electron scattering increases on melting with structural disorder that accompanies solid-liquid transition, the integrated effects of magnetic short range order and the *d* resonance contributes to the overall resistivity of Co on melting. From the NFE model, the T-variation of resistivity in the liquid state follows from the T-dependent Fourier transform of the radial distribution function of

the liquid ions. It is expected in the case of MNFE that the T-variation of resistivity includes additional terms from the T-dependence of magnetic ordering and *d* resonance scattering.

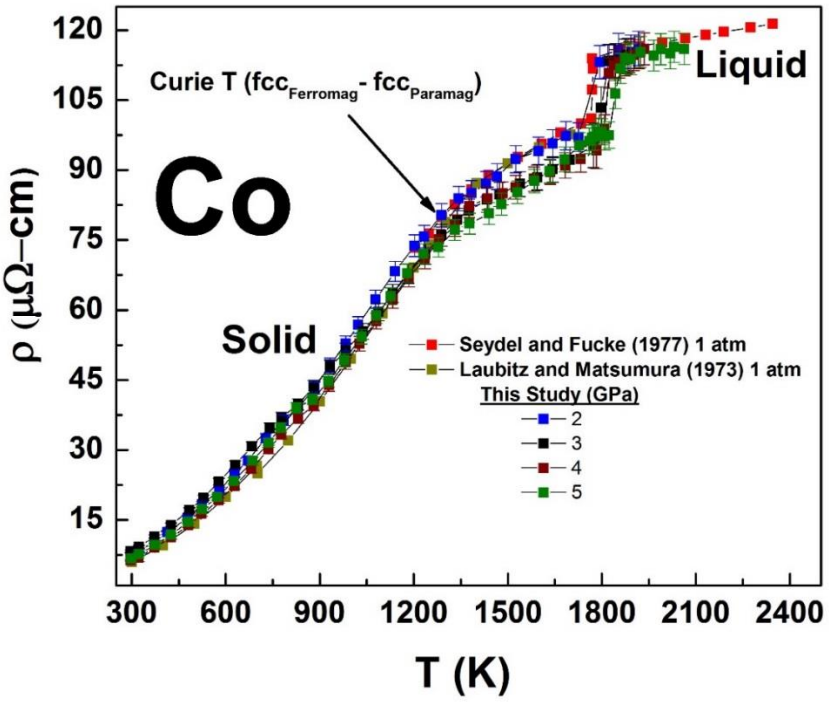

Figure 4.3. The Temperature dependence of electrical resistivity of solid and liquid Co at pressures in the range 2 – 5 GPa compared with the temperature dependence of resistivity at 1 atm by Laubitz and Matsumura [40] and by Seydel and Fucke [52].

As shown in Figure 4.4, the melting T at a fixed P was determined by taking the average of the T measured at the start and completion of melting. Melting T determined at 2 – 5 GPa in this way agrees with previous experimental studies [57].

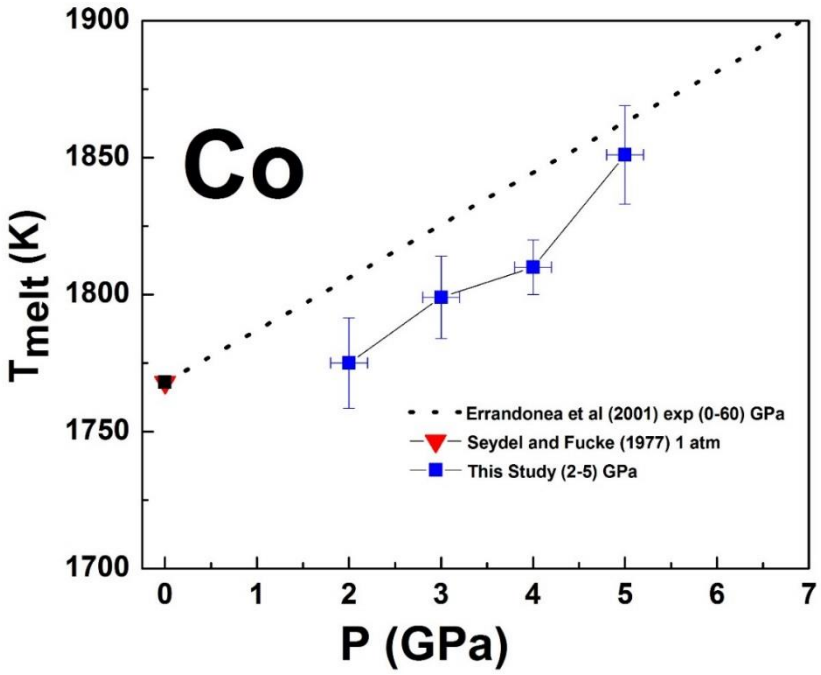

Figure 4.4. Melting curve of Co up to 5GPa, determined by the jump in resistivity in this study, compared with previous studies.

As expected, the resistivity of Co decreases with increasing P in the solid state as shown by the isothermal resistivity behavior in Figure 4.5. Comparison with the 1 atm data was only made with the 1600K isotherm and at melting, since the data measured in this study below the Curie T are higher than 1 atm, for reasons previously explained. With increasing P, the amplitude of lattice vibration which induces *s*-*d* and *s*-*s* scattering processes decreases and hence lowers resistivity. The P-dependence of resistivity at the melting boundary of Co as shown in Figure 4.5, demonstrates that the combined effects of P and T on the electrical resistivity of Co on melting is such that it remains constant up to the limit of P investigated. At the melting point, the reduction in the amplitude of lattice vibrations with increasing P (decreasing resistivity) could be compensated by the effect of P on the *d*-resonance which is expected to increase hybridization of adjacent d electron orbitals and could bring the Fermi level closer to the *d* virtual bound (increasing

resistivity). The effect of P on the anisotropy of the Fermi surface of the sub-bands is cancelled by T as the Fermi surface becomes near spherical on melting. These effects of P and T on the electrical resistivity of Co at the melting boundary appear to cancel out and hence resistivity is invariant. Though the revised theory by Stacey and Loper [9] predicted that the resistivity of unfilled *d* band transition metals such as Co would vary along its melting boundary, while the earlier theory by Stacey and Anderson [8] predicted the opposite, the calculated value of the P coefficient of resistivity on the melting boundary, $(d\ln\rho/dP)_{melt\ boundary}$, of 0.0018 ± 0.0003 GPa^{-1}, compares well with the zero value as predicted in [8].

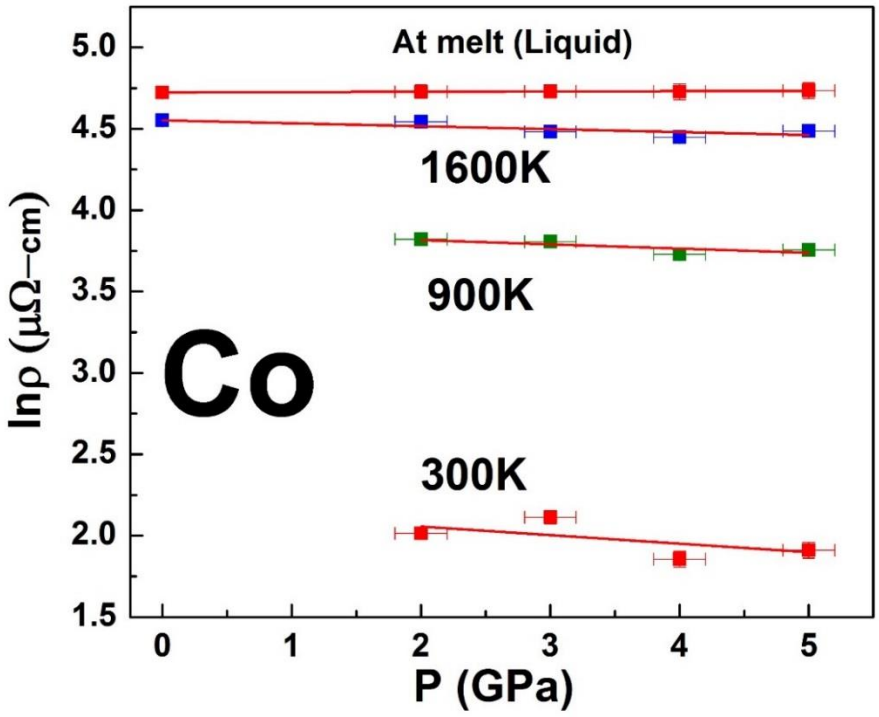

Figure 4.5. Pressure dependence of electrical resistivity of Co in the solid state along the 300K, 900K, 1600K isotherm and in the liquid state (variable T) along the melting boundary. The calculated slopes for the pressure coefficient of resistivity $(d\ln\rho/dP)_T$ along the solid state isotherms based on least squares fit are -0.052 ± 0.048 GPa^{-1}, -0.026 ± 0.013 GPa^{-1}, -0.018 ± 0.048 GPa^{-1} respectively and $(d\ln\rho/dP)_{melt\ boundary} = 0.0018 \pm 0.003$ GPa^{-1}. Data at 1 atm are from Seydel and Fucke [52]. Error bars are provided or within the symbol size.

As shown in Figure 4.5, the P-coefficient of resistivity along the 1600K isotherm, $\left(\frac{\partial \ln \rho}{\partial P}\right)_{1600K}$, is -0.018 $\pm$ 0.003 GPa^{-1}, or an order of magnitude lower than along the melting boundary. Comparison of values of $\left(\frac{\partial \ln \rho}{\partial P}\right)_{1600K}$, determined from this study was made with the value calculated using the relationship derived by Stacey and Anderson:

$$\left(\frac{\partial \ln \rho}{\partial P}\right)_{1600K} = \frac{-2\left(\gamma - {}^{1}/_{3}\right)}{K_T} \qquad (1)$$

where γ is the Grüneisen parameter and K_T is the isothermal bulk modulus. γ was estimated to be 2.6 for solid Co at 1600K from the 2.0 value measured at the Curie T at 1 atm by Armentrout and Kavner [55] and applying a T-dependence of γ given by Singh [58]. With a K_T value of 150GPa at 1600K [55], a value of -0.03 GPa^{-1} for $(\partial \ln \rho/\partial P)_{1600K}$ was calculated from Eqn (1). The prediction of $(\partial \ln \rho/\partial P)_{1600K}$ by Eqn (1) compares reasonably with the measured experimental value. Because of the β-Co incorporation in the α-Co phase during the preheating cycle in these experiments, the evaluation of the Eqn (1) was only made at 1600K. It is expected that at 1600K, the β-Co phase should be the only phase present as discussed earlier.

The T-coefficient of resistivity is shown for different ranges of T as a function of P in Figure 4.6. The high P data of the present study are in good agreement with the 1 atm data [39, 51].

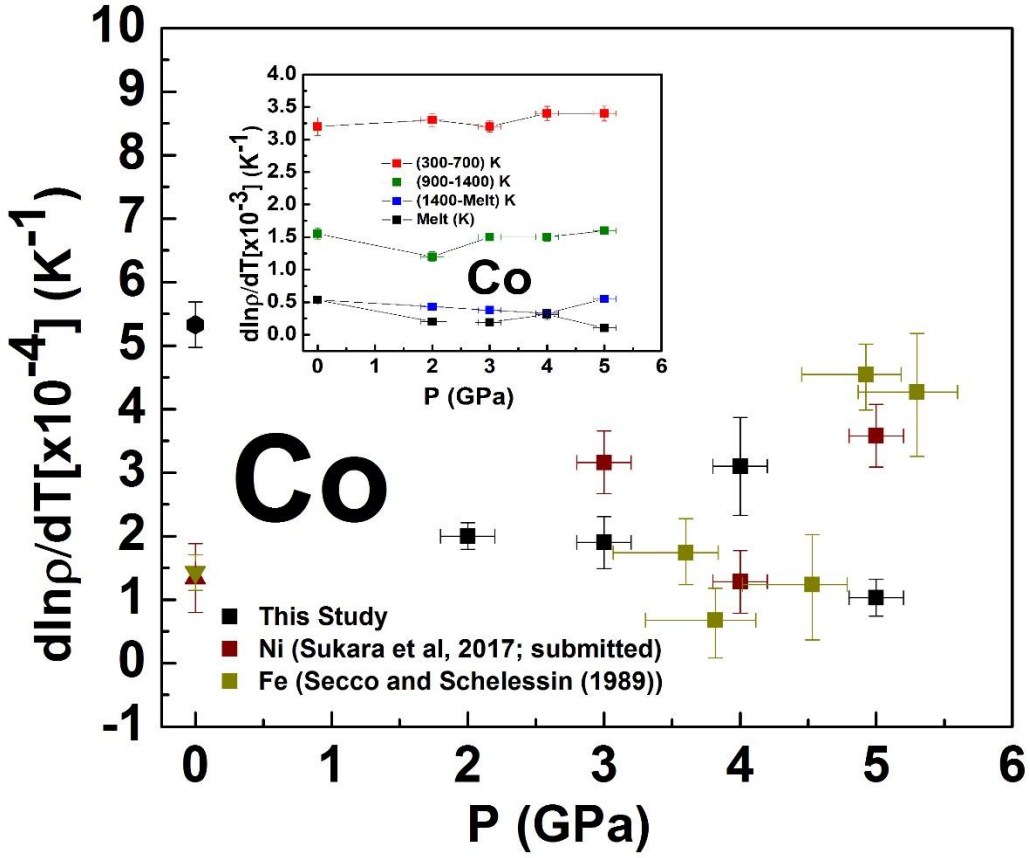

Figure 4.6. Temperature-coefficient of resitivity of Co as a function of pressure at various temperatures. The data at 1 atm are from Laubitz and Matsumura [40] for room T to 1400K and from Seydel and Fucke [52] from 1400K to liquid. Comparisons are made with Fe [68] and Ni. The 1 atm data in Fe and Ni are average data as collected by Sukara et al. [69].

Shown in Figure 4.7 is the Curie T determined at different fixed P. Within the limit of error, the Curie T appears to be constant in agreement with a previous experimental study [41]. The band calculation of ferromagnetic hcp Co at ambient conditions obtained by a simple rigid splitting of the paramagnetic bands demonstrated that the spin band gap is about 1.3eV [59, 60]. Theoretical studies on the magnetic states, as a function of Wigner-Seitz radius, using the total energy band theory with the local density approximation [61-63] suggest that the structural symmetry and local environment strongly affect magnetic ordering and are responsible for the difference in

ferromagnetism among the *3d* metals. The relative shift in the magnetic spin band gap with increasing P causes sub-bands electrons to redistribute between states of different symmetry. The increasing effect of P also causes changes in the corresponding volumes and cross-sections of certain parts of the Fermi surface in non-hybridized *s-p-d* states obtained in a metal like Co, otherwise the effect of electron redistribution is hardly observed [64]. The consequence of electron redistribution and changes in the volume cross-sections of the Fermi surface seems to compensate each other in such a way that the Curie T variation with P remains approximately constant as shown in Figure 4.7.

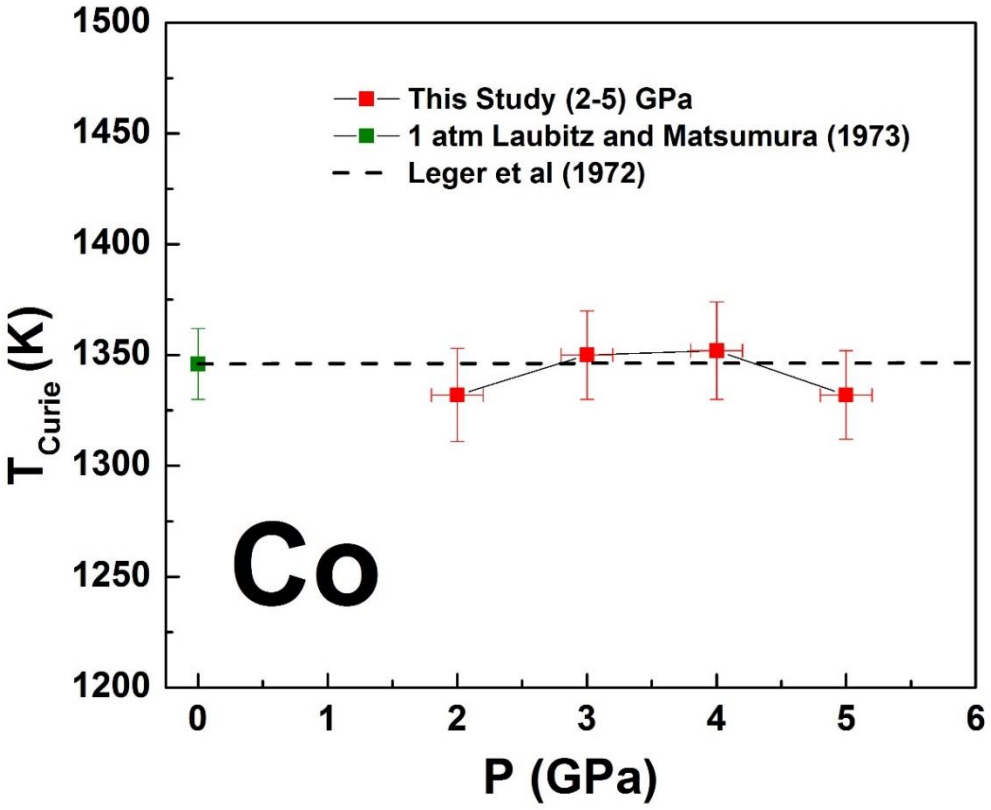

Figure 4.7. Curie temperature of Co up to 5GPa, determined by the change in the slope of the temperature dependence of the resistivity, compared with previous studies by Laubitz and Matsumura [40].

Thermal conductivity *(k)* is a difficult property to measure on metals because of the difficulty in establishing and maintaining a small T-gradient. This challenge is magnified at high T and at high P. A further difficulty is present in the liquid state where the possibility of convection and chemical contamination of the sample by the sample container increases. Fortunately, from the electrical resistivity relationship with the electronic component of thermal conductivity *(ke)* through the Wiedemann-Franz law [65], $ke = \frac{LT}{\rho}$, where L is the Lorenz number, and ρ is the electrical resistivity; *ke* can be calculated from the measured resistivity. In a metal, the electronic component dominates over the phonon component thus the calculation by the Wiedemann-Franz law, using a selected value of L, is expected to provide a good estimate of the total thermal conductivity. The electronic thermal conductivity of Co was calculated from the electrical resistivity measured in this study using the Sommerfeld value $Lo = (2.445 \text{ x } 10^{-8} \frac{V^2}{K^2})$of L. As expected, *ke* decreases with increasing T in the solid state. On melting, *ke* decreases to approximately 87% of the solid state value and in the liquid state *ke* increases with T. With increasing P, *ke* increases both in the solid and liquid state. Also, plotted on Figure 4.8 for comparison are the recommended values of total thermal conductivity, *ktotal,* at 1atm from experimental studies as collected in Ho et al. [66]. The 1 atm experimental values of *ktotal* are higher than the values of *ke* calculated from electrical resistivity using the Wiedemann-Franz Law. This suggests that L_o is not valid for Co at high T and in the liquid state. The insert plot in Figure 4.8 indeed shows that the Lorenz number varies with T for Co [39].

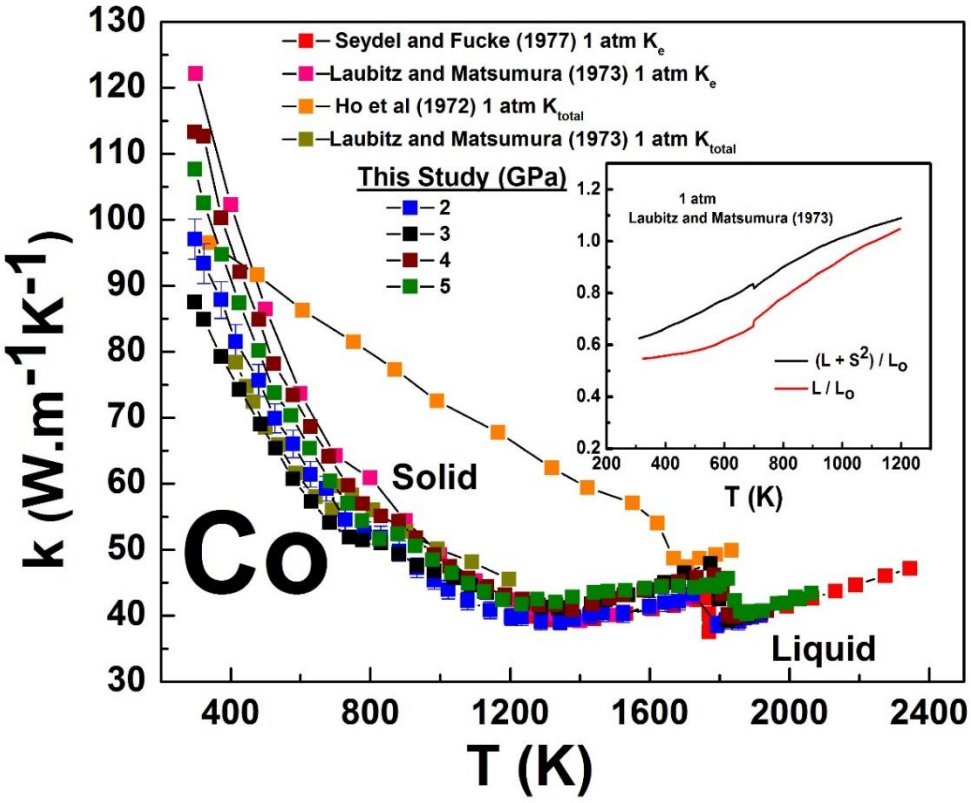

Figure 4.8. Temperature dependence of the thermal conductivity at various pressures. The electronic component (k_e) was calculated from the electrical resistivity data using the Wiedemann-Franz law and a Sommerfeld value ($2.445 \times 10^{-8} \frac{V^2}{K^2}$) of the Lorenz number. Representative error bars are shown for the 3GPa dataset. Comparison is made with the electronic thermal conductivity based on Laubitz and Matsumura [40] and Seydel and Fucke [52] resistivity data at 1 atm and with the total thermal conductivity (k_{total}) from collected experimental measurements reported in Ho et al. [67]. The insert figure shows the temperature dependence of the measured Lorenz function [40], corrected with and without thermoelectric power (S) up to 1200K.

The P-dependence of *ke* at 300K, 900K and 1600K as well on melting is shown in Figure 4.9. Results of *ke* was compared with that calculated using the 1 atm electrical resistivity data of Laubtiz and Matsumura [39] and Seydel and Fucke [51] only for 1600K and at melt. P-coefficient of k_e, $\left(\frac{\partial \ln k_e}{\partial P}\right)_{melt}$ of 0.01499 $\pm$ 0.0006 GPa^{-1} and $\left(\frac{\partial \ln k_e}{\partial P}\right)_{1600K}$ of 0.01484 $\pm$ 0.00243 GPa^{-1}

was calculated from measured data. Comparison of this value was made with the same parameter calculated using the relationship derived by Bohlin [67] in Eqn 2, which is similar to Eqn 1:

$$\left(\frac{\partial \ln k_e}{\partial \mathrm{P}}\right)_T = \frac{(2\gamma - 1/3)}{\mathrm{K_T}} \qquad (2)$$

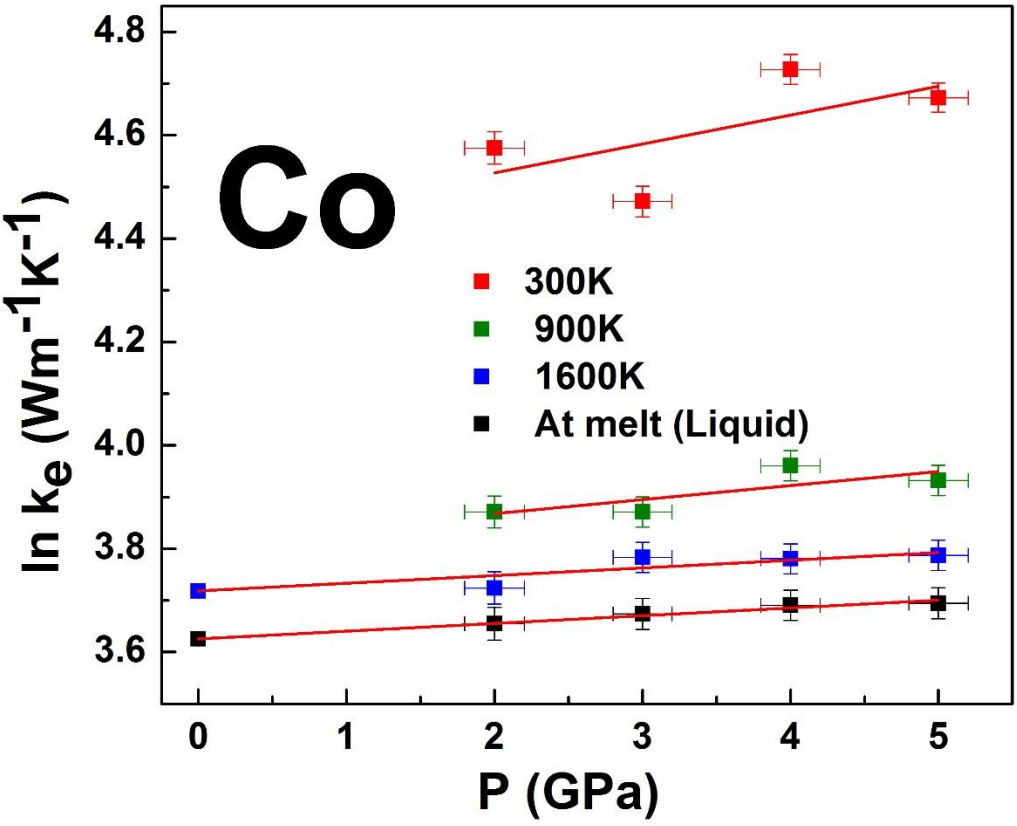

Figure 4.9. Pressure dependence of thermal conductivity of Co at 300K, 900K 1600K and at melt. The calculated slopes $(d\ln\rho/dP)_T$ at solid state iostherms for the pressure coefficient of electronic thermal conductivity k_e, of the fitted lines are = 0.056 $\pm$ 0.048 GPa^{-1}, 0.027 $\pm$ 0.016 GPa^{-1}, 0.015 $\pm$ 0.002 GPa^{-1}, respectively and $(d\ln\rho/dP)_{\text{melt boundary}}$ = 0.015 GPa^{-1}.

The prediction of $(\partial \ln k_e/dP)_{1600K}$ by Eqn (2) is 0.0325 GPa^{-1} which compares relatively well with the experimental value measured in this research and supports the prediction of k_e by the derived expression.

4.3. Conclusion

The T-variation of the electrical resistivity of solid and liquid Co has been investigated up to 5GPa and results demonstrate that the resistivity of Co is invariant along the melting boundary. These findings are interpreted in terms of the antagonistic effects of P and T on the electronic structure of liquid Co as demonstrated in previous studies. The k_e was calculated using the Wiedemann-Franz law. With increasing P, k_e increased both in the solid and liquid state, however, k_e decreased with increasing T in the solid state and increased with T in the liquid state.

Since Fe is an electronic analog of Co, this could imply that the k_{total} of the ICB may be similar to k_{Fe} at 1 atm at the melting point of ~33 $Wm^{-1}K^{-1}$ [3, 4]. This agrees with the result of direct measurement of solid Fe by Konôpková et al. [5] which placed the k_{total} of the Earth's core near the low end of previous estimates at (18-44)$Wm^{-1}K^{-1}$. A low value of k_{core} implies that the age of the inner core may be old and that the geodynamo may have had an energy source from compositionally-induced convection since the birth of the inner core. In addition, a low value of k_{core} such as $33Wm^{-1}K^{-1}$ implies that thermal convection may have played a role in sustaining the geodynamo before the birth of the inner core. It is beyond the scope of this work to speculate further on the thermal conductivity of other regions of the core such as core-mantle boundary.

4.4 References

[1] de Koker, N., Steinle-Neumann, G., and Vlček, V. (2012), Electrical resistivity and thermal conductivity of liquid Fe alloys at high P and T, and heat flux in Earth's core. *Proceedings of the National Academy of Sciences*, 109(11), 4070-4073.

[2] Pozzo, M., Davies, C., Gubbins, D., and Alfe, D. (2012), Thermal and electrical conductivity of iron at Earth's core conditions. *Nature*, 485(7398), 355-358.

[3] Gomi, H., Ohta, K., Hirose, K., Labrosse, S., Caracas, R., Verstraete, M. J., and Hernlund, J. W. (2013), The high conductivity of iron and thermal evolution of the Earth's core. *Physics of the Earth and Planetary Interiors*, 224, 88-103.

[4 Pozzo, M., Davies, C., Gubbins, D., and Alfè, D. (2014), Thermal and electrical conductivity of solid iron and iron–silicon mixtures at Earth's core conditions. *Earth and Planetary Science Letters*, 393, 159-164.

[5] Gubbins, D., Alfè, D., Davies, C., and Pozzo, M. (2015), On core convection and the geodynamo: Effects of high electrical and thermal conductivity. *Physics of the Earth and Planetary Interiors*, 247, 56-64.

[6] Gomi, H., Hirose, K., Akai, H., and Fei, Y. (2016), Electrical resistivity of substitutionally disordered hcp Fe–Si and Fe–Ni alloys: Chemically-induced resistivity saturation in the Earth's core. *Earth and Planetary Science Letters*, 451, 51-61.

[7] Ohta, K., Kuwayama, Y., Hirose, K., Shimizu, K., and Ohishi, Y. (2016), Experimental determination of the electrical resistivity of iron at Earth's core conditions. *Nature*, 534(7605), 95-98.

[8] Stacey, F. D., and Anderson, O. L. (2001). Electrical and thermal conductivities of Fe–Ni–Si alloy under core conditions. *Physics of the Earth and Planetary Interiors*, 124(3), 153-162.

[9] Stacey, F. D., and Loper, D. E. (2007). A revised estimate of the conductivity of iron alloy at high pressure and implications for the core energy balance. *Physics of the Earth and Planetary Interiors*, 161(1), 13-18.

[10] Stoner, E. C. (1938). Collective electron ferromagnetism. *Proceedings of the Royal Society of London. Series A, Mathematical and Physical Sciences*, 372-414.

[11] Janak, J. F. (1977). Uniform susceptibilities of metallic elements. *Physical Review B*, 16(1), 255.

[12] Landrum, G. A., and Dronskowski, R. (2000). The orbital origins of magnetism: from atoms to molecules to ferromagnetic alloys. *Angewandte Chemie International Edition*, 39(9), 1560-1585.

[13] Stoner, E. C. (1939). Collective electron ferromagnetism. II. Energy and specific heat. *Proceedings of the Royal Society of London. Series A, Mathematical and Physical Sciences*, 339-371.

[14] Janak, J. F. (1978). Itinerant ferromagnetism in fcc cobalt. *Solid State Communications*, 25(2), 53-55.

[15] Eastman, D. E., Janak, J. F., Williams, A. R., Coleman, R. V., and Wendin, G. (1979). Electronic structure of magnetic 3d metals: Ground state, fermi surface and photoemission properties. *Journal of Applied Physics*, 50(B11), 7423-7438.

[16] Andersen, O. K., Madsen, J., Poulsen, U. K., Jepsen, O., and Kollar, J. (1977). Magnetic ground state properties of transition metals. *Physica B+ C*, *86*, 249-256.

[17] Poulsen, U. K., Kollar, J., and Andersen, O. K. (1976). Magnetic and cohesive properties from canonical bands (for transition metals). *Journal of Physics F: Metal Physics*, *6*(9), L241.

[18] Chikazumi, S., and Graham, C. D. (2009). Physics of ferromagnetism 2e (No. 94). *Oxford University Press on Demand*.

[19] Steinle-Neumann, G., Stixrude, L., and Cohen, R. E. (1999). First-principles elastic constants for the hcp transition metals Fe, Co, and Re at high pressure. *Physical Review B*, *60*(2), 791.

[20] Yoo, C. S., Cynn, H., Söderlind, P., and Iota, V. (2000). New β (fcc)-cobalt to 210 GPa. *Physical Review Letters*, *84*(18), 4132.

[21] Goncharov, A. F., Crowhurst, J., and Zaug, J. M. (2004). Elastic and vibrational properties of cobalt to 120 GPa. *Physical Review Letters*, *92*(11), 115502.

[22] Iota, V., Klepeis, J. H. P., Yoo, C. S., Lang, J., Haskel, D., and Srajer, G. (2007). Electronic structure and magnetism in compressed 3d transition metals. *Applied Physics Letters*, *90*(4), 42505-42505.

[23] Gold, A. V. (1974). Review paper: Fermi surfaces of the ferromagnetic transition metals. *Journal of Low Temperature Physics*, *16*(1-2), 3-42.

[24] Rosenman, I., and Batallan, F. (1972). Low-frequency de Haas-van Alphen effect in cobalt. *Physical Review B*, *5*(4), 1340.

[25] Batallan, F., Rosenman, I., and Sommers, C. B. (1975). Band structure and fermi surface of hcp ferromagnetic cobalt. *Physical Review B*, *11*(1), 545.

[26] McMullan, G. J., Pilgram, D. D., and Marshall, A. (1992). Fermi surface and band structure of ferromagnetic cobalt. *Physical Review B*, *46*(7), 3789.

[27] Pérez-Díaz, J. L., and Muñoz, M. C. (1995). Fermi surface of ferromagnetic fcc cobalt. *Physical Review B*, 52(4), 2471.

[28] Anderson, J. R., and Schirber, J. E. (1981). Influence of pressure on de Haas-van Alphen frequencies in cobalt. *Journal of Applied Physics*, 52(3), 1630-1632.

[29] Veselago, V. G., and Vinokurova, L. I. (1988). The magnetic and electron structures of Transition Metals and Alloys (Vol. 3). *Nova Publishers*, page 154.

[30] Coleman, R. V., Morris, R. C., and Sellmyer, D. J. (1973). Magnetoresistance in Iron and Cobalt to 150 kOe. *Physical Review B*, 8(1), 317.

[31] Batallan, F., and Rosenman, I. (1973). Magnetoresistance and open orbits domain in cobalt. *Solid State Communications*, *12*(1), 75-78.

[32] Cohen, M. H., and Falicov, L. M. (1960). Effect of spin-orbit splitting on the Fermi surfaces of the hexagonal-close-packed metals. *Physical Review Letters*, 5(12), 544.

[33] Joseph, A. S., Gordon, W. L., Reitz, J. R., and Eck, T. G. (1961). Evidence for spin-orbit splitting in the band structure of Zinc and Cadmium. *Physical Review Letters*, 7(9), 334.

[34] Alekseevskii, N. E., and Gaidukov, Y. P. (1963). Open cross sections of Cadmium, Zinc and Thallium Fermi surfaces. *Soviet Journal of Experimental and Theoretical Physics*, 16, 1481.

[35] Cohen, M. H., and Falicov, L. M. (1961). Magnetic breakdown in crystals. *Physical Review Letters*, 7(6), 231.

[36] Kasowski, R. V., and Falicov, L. M. (1969). Calculation of the temperature dependence of the Knight shift in Cadmium. *Physical Review Letters*, 22(19), 1001.

[37] Mott, N. F. (1936). The electrical conductivity of transition metals. In *Proceedings of the Royal Society of London A: Mathematical, Physical and Engineering Sciences* (Vol. 153, No. 880, pp. 699-717). The Royal Society.

[38] Guillermet, A. F. (1987). Critical evaluation of the thermodynamic properties of cobalt. *International Journal of Thermophysics*, *8*(4), 481-510.

[39] Laubitz, M. J., and Matsumura, T. (1973). Transport properties of the ferromagnetic metals. I. Cobalt. *Canadian Journal of Physics*, 51(12), 1247-1256.

[40] Edwards, D. M. (1974). Temperature dependence of the exchange splitting in ferromagnetic metals II. The study of stoner excitations by the de Haas-van Alphen effect. *Canadian Journal of Physics*, 52(8), 704-707.

[41] Leger, J. M., Loriers-Susse, C., and Vodar, B. (1972). Pressure effect on the Curie temperatures of transition metals and alloys. *Physical Review B*, 6(11), 4250.

[42] Shimizu, M. (1978). Forced magnetostriction, magnetic contributions to bulk modulus and thermal expansion and pressure dependence of Curie temperature in Iron, Cobalt and Nickel. *Journal of the Physical Society of Japan*, 44(3), 792-800.

[43] Faber, T. E., and Ziman, J. M. (1965). A theory of the electrical properties of liquid metals: III. The resistivity of binary alloys. *Philosophical Magazine*, 11(109), 153-173.

[44] Ashcroft, N. W., and Lekner, J. (1966). Structure and resistivity of liquid metals. *Physical Review*, 145(1), 83.

[45] Ziman, J. M. (1961). A theory of the electrical properties of liquid metals. I: The monovalent metals. *Philosophical Magazine*, 6(68), 1013-1034.

[46] Evans, R., Greenwood, D. A., and Lloyd, P. (1971). Calculations of the transport properties of liquid transition metals. *Physics Letters A*, 35(2), 57-58.

[47] Gaspari, G. D., and Gyorffy, B. L. (1972). Electron-phonon interactions, d resonances, and superconductivity in transition metals. *Physical Review Letters*, 28(13), 801.

[48] Mott, N. F. (1972). The electrical resistivity of liquid transition metals. *Philosophical Magazine*, 26(6), 1249-1261.

[49] Secco, R. A. (1995). High p, T physical property studies of Earth's interior: Thermoelectric power of solid and liquid Fe up to 6.4 GPa. *Canadian Journal of Physics*, 73(5-6), 287-294.

[50] Secco, R. A., and Schloessin, H. H. (1986). On-line p, T calibration based on well-known phase transitions. *Journal of Applied Physics*, 60(5), 1625-1633.

[51] Seydel, U., and Fucke, W. (1977). Sub-microsecond pulse heating measurements of high temperature electrical resistivity of the 3d-transition metals iron, cobalt, and nickel. *Chemischer Informationsdienst*, *8*(49).

[52] Whittemore, C. (1961). 8. Cobalt. *Rare metals handbook*, 2nd ed. edited by C.A Hampel (Reinhold, N.Y), p.114.

[53] Güntherodt, H. J., Hauser, E., Künzi, H. U., and Müller, R. (1975). The electrical resistivity of liquid Fe, Co, Ni and Pd. *Physics Letters A*, 54(4), 291-292.

[54] Busch, G., and H-J. Güntherodt. Electronic properties of liquid metals and alloys. *Solid State Physics* 29 (1974): 235-313, page 289.

[55] Armentrout, M. M., and Kavner, A. (2015). A new high pressure and temperature equation of state of fcc cobalt. *Journal of Applied Physics*, 118(19), 194904.

[56] Shvets, V. T. (1982). Influence of sd hybridization of the electrical conductivity of liquid transition metals. *Theoretical and Mathematical Physics*, 53(1), 1040-1046.

[57] Errandonea, D., Schwager, B., Ditz, R., Gessmann, C., Boehler, R., and Ross, M. (2001). Systematics of transition-metal melting. *Physical Review B*, 63(13), 132104.

[58] Singh, R. N., Arafin, S., and George, A. K. (2007). Temperature-dependent thermo-elastic properties of s-, p-and d-block liquid metals. *Physica B: Condensed Matter*, 387(1), 344-351.

[59] Wong, K. C., Wohlfarth, E. P., and Hum, D. M. (1969). Density of states and effective electron interaction in hexagonal cobalt. *Physics Letters A*, *29*(8), 452-453.

[60] Batallan, F., Rosenman, I., and Sommers, C. B. (1975). Band structure and Fermi surface of hcp ferromagnetic cobalt. *Physical Review B*, 11(1), 545.

[61] Moruzzi, V. L. (1986). Singular volume dependence of transition-metal magnetism. *Physical Review Letters*, 57(17), 2211.

[62] Moruzzi, V. L., Marcus, P. M., Schwarz, K., and Mohn, P. (1986). Ferromagnetic phases of bcc and fcc Fe, Co, and Ni. *Physical Review B*, 34(3), 1784.

[63] Marcus, P. M., and Moruzzi, V. L. (1988). Magnetism of metastable phases: Band theory and epitaxy. *Journal of Applied Physics*, 63(8), 4045-4050.

[64] Svechkarev, I. V., and Panfilov, A. S. (1974). Effects of pressure on the electronic structure of transition d-metals. *Physica Status Solidi (b)*, 63(1), 11-50. Page 33.

[65] Franz, R., and Wiedemann, G. (1853). Ueber die Wärme-Leitungsfähigkeit der Metalle. *Annalen der Physik*, *165*(8), 497-531.

[66] Ho, C. Y., Powell, R. W., and Liley, P. E. (1972). Thermal conductivity of the elements. *Journal of Physical and Chemical Reference Data*, *1*(2), 279-421.

[67] Bohlin, L. (1976). Thermal conduction of metals at high pressure. *Solid State Communications*, *19*(4), 389-390.

[68] Secco, R. A., and Schloessin, H. H. (1989). The electrical resistivity of solid and liquid Fe at pressures up to 7 GPa. *Journal of Geophysical Research: Solid Earth*, *94*(B5), 5887-5894.

[69] Sukara, E.R, Secco, R.A and Yong, W (in prep, 2017) Electrical Resistivity Measurements of solid and Liquid Ni at High Pressures.

Chapter 5: Electronic Transition in Solid Nb at High Pressure and Temperature

5.0. Introduction

From the general concept of magnetic susceptibility, the electron spin susceptibility of paramagnetic metals decreases as electrons are excited and spin fluctuation increases with increasing total internal energy as temperature (T) rises [1] . This is primarily due to the gain in momentum of the electron spin when the total internal energy is raised thermally which overrides a forced spin alignment caused by the external magnetic field. However, the T-variation of spin susceptibility of some paramagnetic metals investigated by Stoner [2] demonstrated a positive coefficient with increasing T. Stoner demonstrated that their spin susceptibility is dependent on their electronic band form. With increasing T, electrons can transfer from the lower sub-band to the upper sub-band, forcing electron spin ordering and hence positive magnetic susceptibility. The ability of an electron to tunnel from the lower sub-band to the upper sub-band is brought about by the position of Fermi level in the Density of States (*N)* function. If the top of the Fermi level of two overlapping bands falls close to a region of a minimum in *N*, the probability of electrons tunneling from the lower band and populating the upper band will dominate over spin fluctuation with increasing T. Theoretical study [3] grouped the paramagnetic transition metals into a "plus group" (Mo, W, Zr, Ti and Cr) composed of those exhibiting a positive coefficient of spin susceptibility with increasing T and a "minus group" (V, Pt, Pd, Ta and Nb) composed of those exhibiting a negative coefficient of spin susceptibility with increasing T. The Fermi level of the plus group is located within a region of a minimum in *N* while the Fermi level of the minus group is located within a region of a maximum in *N*.

The concavity of T-dependence of the electrical resistivity at 1atm of the plus and the minus groups were clearly distinct. While the plus group showed a convex slope with rising T, the minus group slope is concave with increasing T [4]. In the case of the T-dependences of the electrical resistivity of Pd and Pt of the minus group investigated by Mott [5, 6], the possibility of a change in density of states of the *d*-electrons (N_d) at high temperature within the model of *s*-*d* scattering, in conjunction with Debye T variation as a function of thermal expansion, was suggested. This model explained that at high T, the available N_d decreases and thus, less of the *s* conduction electrons which dominate conduction are scattered, resulting in lower resistivity. This effect causes the T-coefficient of resistivity of Pd and Pt to decrease at higher T contrary to the expected trend from a linear law [5] predicted by Bloch-Grueneisen function. Similarly, theoretical calculation [4] demonstrated that *R/T*, *1/k*, and *T/ S* variation with T increases for the plus group but decreases for the minus group respectively (R is resistance, k is thermal conductivity and S is thermoelectric power). The electronic spin susceptibility and electronic specific coefficient also increases with increasing T for the plus group but decreases with increasing T for the minus group [4]. Thus, there is a clear distinction in the T-dependent behaviour of properties which depend on the electronic structures of the plus and the minus groups. While changes in lattice structure are accompanied by changes in electronic structure, the reverse is not usually the case.

The theory of electrical resistivity of transition metals in the solid state is generally understood in the context of *s*-*d* scattering [5]. In metals, valence electrons are delocalised and are distributed over a range of energy bands. With increasing T, thermal vibrations of the lattice reduce the mean free path of an electron by increasing the probability of phonon-induced electron scattering processes. Although the resistivity of a metal is approximately proportional to the absolute T above Debye T, as predicted by Bloch theory, there are deviations at very high T due

to thermal expansion. As T increases in unfilled *d*-band metals, the higher mobility s electrons are scattered to unfilled *d* band states where their effective mass increases, leading to a decrease in mobility and higher resistivity. However, with increasing P, the amplitude of lattice vibration is reduced, as a consequence of volume reduction, which reduces phonon-induced scattering processes and lowers resistivity.

Understanding the electrical resistivity of a metal at elevated P and/or T conditions requires knowledge of the electronic band structure at those conditions. The electronic structure of Cr, Mo and W of the plus group metals [7] was based primarily on Fe band structure calculations [8]. This model demonstrated that the Fermi surface of the plus group has a deformed surface, containing roughly an equal number of electrons and holes at the Γ and *H* symmetry points respectively, with additional small holes at *N* and pockets of electrons or holes along the cubic ΓH symmetry. On the other hand, the electronic structure of V, Nb and Ta of the minus group, predicted earlier from the augmented plane wave energy calculations for W by Matheiss [9], reveals a set of 6 distorted ellipsoidal surfaces centered at *N* in the Brillouin zone and a multiply connected so-called *"jungle-gym."* The ellipsoidal surfaces consist of inter-connecting arms along the (100) direction with intersections of Γ and *H*, resulting in a Fermi surface that is not as deformed as the plus group [2]. The band structure of Nb has been well investigated both experimentally and theoretically [10-17], using different techniques. Experimental investigation of the frequency shifts in the de Hass van Alphen oscillations in the Nb Fermi surface under the influence of hydrostatic P [18] demonstrated that the cross sectional area of the hole ellipsoids at *N* changes almost uniformly with pressure at approximately 0.1% / kbar while the *jungle-gym* arms extremal cross section normal to (100) decreases significantly with P. Thus the anisotropy in the P derivative of the Fermi

surface of Nb could cause a deformation of the surface, such that under P, it could mimic the already deformed Fermi surface of the plus group [2] at ambient conditions.

Static compression of Nb up to 54GPa at room T showed no evidence of any structural phase transition [19]. Upon compression, the Brillouin zone with the Fermi surface enclosed, expands and ideally scales with increasing P in the case of an isotropically compressible metal like Nb with a cubic crystal structure similar to Cu [20]. However, the exhibition of anisotropy in the P derivative of Nb Fermi surface demonstrates that Nb deviates from the expected behaviour. Superconducting temperature (T_c) and electron-phonon coupling investigations in Nb up to 132GPa using magnetic susceptibility techniques [21] showed anomalies in T_c around 5-6GPa and 60-70GPa. The anomaly around 5-6GPa was suggested to arise from stress sensitive electronic topological transition while the 60-70GPa anomaly arose from the crossing of the Fermi level with the *d* bands which requires a decrease of about 8% of the lattice constant [21]. Nonetheless, a full potential linear muffin-tin orbital method based on linear response approach used in calculating the electron-phonon coupling in Nb under hydrostatic P [22] did not observe an anomaly around 5GPa. It was suggested that the P conditions under which the experimental study [21] were made may not have been hydrostatic. Interestingly, the partial *N* function investigation of Nb using the generalized gradient approximation within the framework of density functional theory [22] indicates that the s and *d* bands move away relative to the Fermi level position as the unit cell volume decreases. Hence, from the concept of the spin polarization of the unfilled *d* band electrons in ferromagnetic transition metals [23] and perhaps paramagnetic metals, the relative displacement of the *d* states could move the Fermi level position into the region of anti-bonding states creating an in-balance in chemical potential between the sub-bands at reduced volume. With increasing T, the chemical potential in-balance increases and may eventually lead to adjustment in the position

of the Fermi level as electrons redistribute between the upper and lower bands, in order to maintain a balanced chemical potential between the lower and upper sub-bands.

The understanding of the electrical resistivity and thermal conductivity of paramagnetic metals under high P and/or T conditions is not only important in characterizing the nature of electron-phonon, electron-electron and spin polarization interactions as well any associated phase changes in their condensed matter state, but also on their relation to the lower spin sub-band of Earth's interior materials such as Fe and Ni which are electronically analogous to Mo and W respectively [24]. Nb in particular has attracted a considerable amount of attention due to its importance in electronics, nuclear and superconducting applications. Surprisingly, there is no study on the combined effects of high P and T on the electrical resistivity behaviour of virtually all the paramagnetic metals to date. In this study, investigation of the T-dependence of electrical resistivity of Nb at fixed P range 2-5GPa up to ~1900K was made. The experimental investigations of electrical resistivity of Nb at 1atm up to ~2000K measured by Tye [25] and up to ~1700K by Aisaka and Shimizu [4] will be compared with that measured in this study.

5.1. Experimental Details

The experiments were performed in a 1000-ton cubic press with pyrophyllite as the P-transmitting medium. Illustrated in Figure 5.1A, B and Figure 5.1C are the measurement technique and the cubic P cell design, respectively. The sample pressure was determined from hydraulic oil P using prior unpublished calibrations similar to those previously described [26, 27]. The dimensions of the Nb wire (99.99% purity, Alfa Aesar) were 0.51mm in diameter and 1.78mm in length. The welded junctions of the Pt-Pt10%Rh thermocouples, which also served as 4-wire electrodes, were in direct contact with the ends of the wire sample. Both the thermocouples and the sample were contained in a ceramic (Al_2O_3) tube. The sample length was 0.05mm longer than

the Al_2O_3 sample container which provided good thermocouple/electrode-sample contact. The Al_2O_3 sample container was contained in a boron nitride (BN) sleeve and a cylindrical graphite sleeve next to and outside the BN acted as a heat source when a high alternating current was passed through it. A cylindrical zirconia (ZrO_2) sleeve and two ZrO_2 disks, placed as shown in Figure 5.1C, provided thermal insulation.

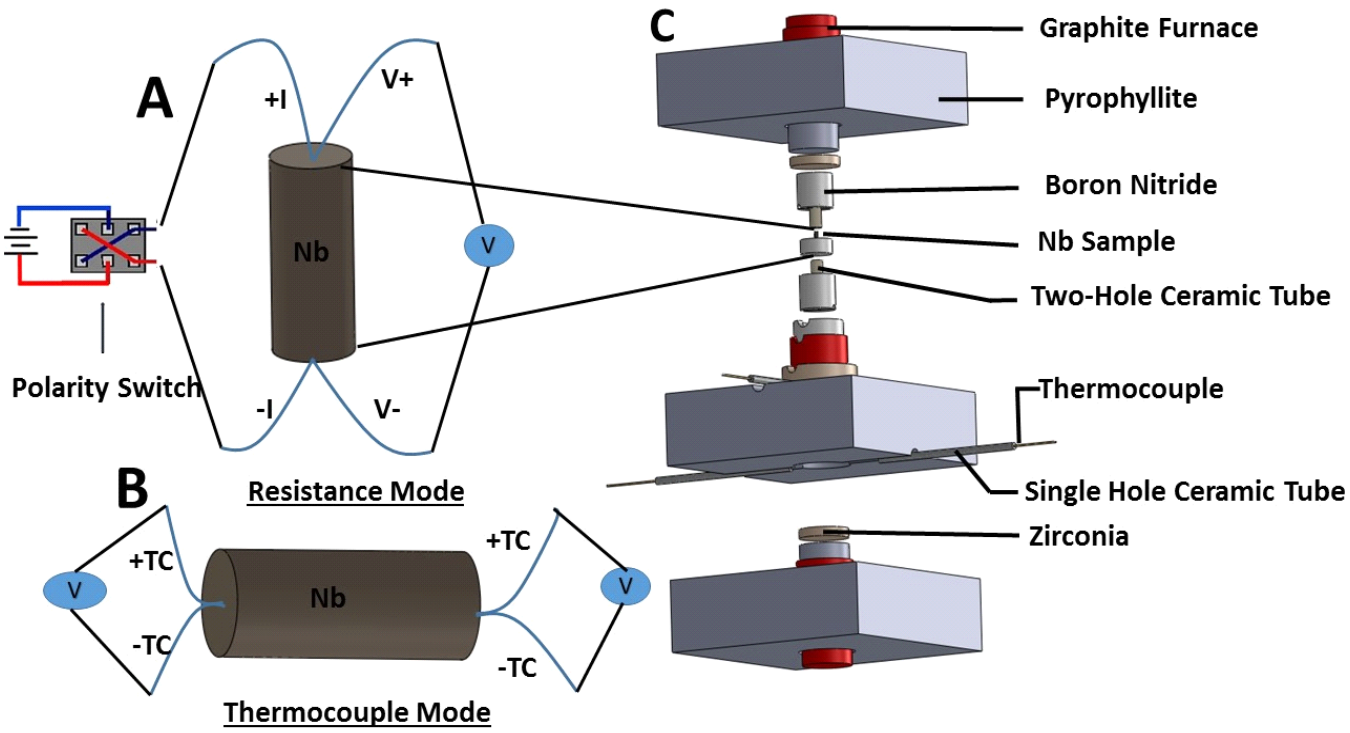

Figure 5.1. Schematic drawing of two modes (resistance (A) and temperature (B)) of measurement. (A) Four–wire probe design, showing the current polarity switch and the voltmeter for measuring the voltage drop across the sample. (B) Thermocouples measuring the temperature on top and bottom of the sample. (C) Exploded view (SolidWorks^{TM}) of the 1 inch edge length high-pressure cell with the components parts.

A cubic press with three pairs of opposing anvils in mutually orthogonal directions is normally limited to two cube faces to make resistivity measurements at high P and T conditions. Using one pair of cube faces dedicated to the heater, and another pair needed for T measurement, a straightforward 4-wire electrode resistivity system was not possible. Adopted approach to this

limitation was to use the thermocouples as T sensors in one mode of measurement and 4-wire electrodes in another mode. A switched circuit passed a constant direct current of 0.2A (Keysight B2961A power source) through the Pt leads and sample while measurement of the voltage drop was made using the Pt10%Rh leads with the mode switch in resistance mode (Figure 5.1A). In T mode, the thermocouple EMF's at the top and bottom of the sample were used to measure T (Figure 5.1B). Systematic errors in the voltage drop across the sample from the thermoelectric voltage between the sample and the electrodes were corrected by reversing the current direction with the use of a polarity switch. The mean value of the measured voltages in both current directions was computed at each T in an interval of 50K. A data acquisition meter (Keysight 34470A), operating at a frequency of 20Hz with 1μV resolution, was used to record measurements. The softening of the sample and the electrodes at high T ~700K reached in the preheating cycle, provided a good sample-electrode contact which minimized, if not eradicated, the effect of contact resistance.

The sample resistance was calculated using Ohm's law, $R = \frac{V}{I}$, where R is resistance, V is voltage drop and I is current. The sample resistivity ρ, was calculated by incorporating the recovered sample geometry into Pouillet's law, $\rho = \frac{RA}{l}$, where l and A are sample length and cross-sectional area, respectively. The recovered P cell was ground in a direction parallel to a radial axis of the cylindrical graphite heater to expose the middle section of the sample. Using a microscope (Nikon SMZ2800), the length and diameter of the exposed sample were carefully measured at several locations. Using a JEOL JXA-8530F field-emission electron microprobe with an accelerating voltage of 20kV, a probe current of 50 nA, and a spot size (~100 nm) beam, analyses of the chemical composition of the recovered sample and electrodes were determined by wavelength dispersive X-ray spectroscopy.

5.2. Results and Discussion

The microprobe analyses of the recovered sample as shown Figure 5.2 gave evidence that the sample was not contaminated either by the electrode/thermocouple or sample container. After exposure to high P and T, there are typically small but significant differences in the geometry of successive sample assemblies even though measurements were made with one type of P-cell design. Careful inspection of the recovered sample and measurement of the geometry was made for each sample.

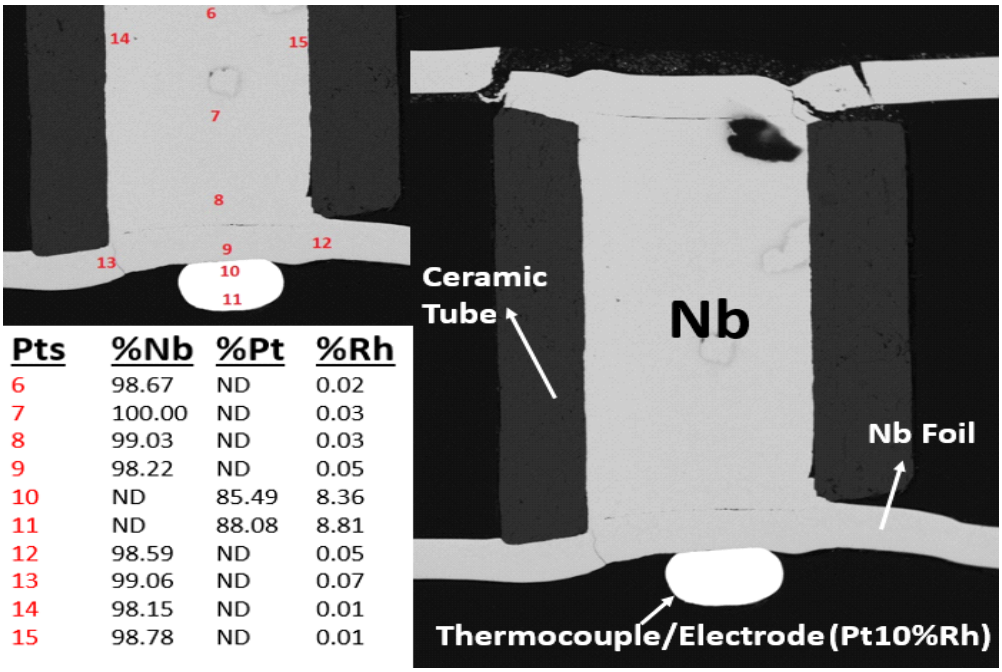

Pts	%Nb	%Pt	%Rh
6	98.67	ND	0.02
7	100.00	ND	0.03
8	99.03	ND	0.03
9	98.22	ND	0.05
10	ND	85.49	8.36
11	ND	88.08	8.81
12	98.59	ND	0.05
13	99.06	ND	0.07
14	98.15	ND	0.01
15	98.78	ND	0.01

Figure 5.2. Back scattered electron image of a sample recovered from 5GPa, 1500K along with tabulated electron microprobe results of probe points 6-15 ("ND" is "not detectable"). The thermocouple/electrodes were Pt and Pt10%Rh. The width of the Nb sample is ~0.5mm.

As shown in Figure 5.3, the resistivity increase with T and decrease with P can been accounted for in the context of P and T effects on phonon-induced *s-d* scattering processes [5]. The electronic configuration of Nb, $Kr4d^{4}5s^{1}$, demonstrates that *4d* band of Nb is unfilled and as such with increasing T, the high mobility *s* electrons undergo both *s-s* and *s-d* scattering processes.

The effective mass of *d*-electrons is greater than the *s*-electron mass and because of the high *N* of the *d* band, the probability of *s*-*d* scattering dominates. Thus, metals with unfilled *d* bands generally have higher resistivity than filled *d* band metals. The T-dependence of resistivity at fixed P up to 5GPa in this study is compared with 1atm data of Nb [25], with behavior of the minus group, and that of W [4], with behavior of plus group, over the entire T-range plotted in Figure 5.3. From the change in concavity of $\rho(T)$ in Figure 5.3, it is obvious that the T-dependent resistivity of Nb at fixed P undergoes a transition from the minus group to plus group behavior in the mid-T range. The transition may be understood in terms of the P effect on the Fermi surface of Nb and the relative position of *s* and *d* bands with respect to the Fermi level. Under the influence of P, the anisotropy in the P derivative of Fermi surface of Nb [18] causes deformation that render it comparable to the Fermi surface of the plus group at ambient conditions [2]. Also the relative separation of the *s* and *d* bands from the Fermi surface at reduced volume creates a meta-stability in the upper and lower band with its associated Fermi level position. With increasing T, the in-balance in chemical potential between sub-bands increases and eventually the system finds an equilibrium position which leads to electron redistribution and relative movement of the Fermi level. This re-positions the Fermi level to a region of the minimum in the *N* function. Hence at high P and T above the transition T, the electronic structure of Nb mimics that of the plus group at ambient conditions which is characterized by a deformed Fermi surface with a Fermi level position in the region of the minimum in the *N* function. The transition observed is thus an electronic transition.

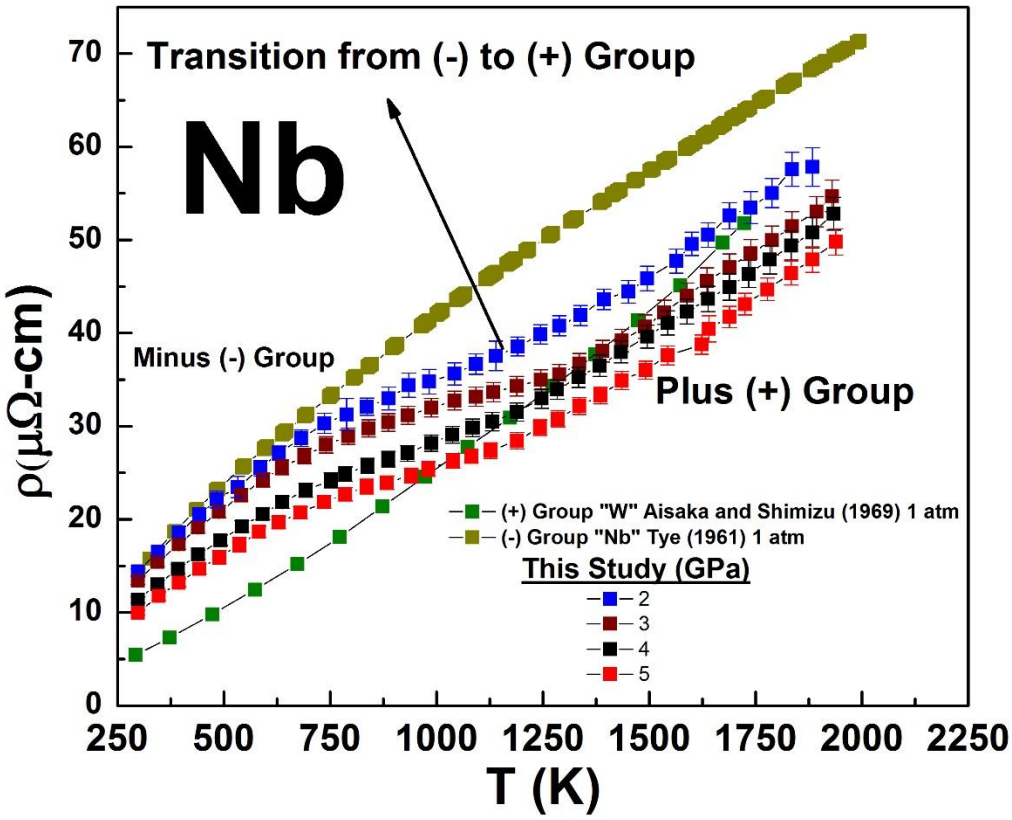

Figure 5. 3. Temperature dependence of electrical resistivity of Nb at fixed pressures compared with 1atm data of Nb by Tye [24] and W by Aisaka, and Shimizu [5].

The P-dependence of the transition temperature shown in Figure 5.4 has a negative slope. It is not clear from the P-range studied if this slope should continued back to 1atm. On the other hand, it appears the concavity of the 1atm changes with T and in the 1400-1500K region, the slope of resistivity vs T appears nearly constant. The insert illustrates that, assuming a constant P-dependence of the transition T above 2GPa, Nb will transform to the plus group at P ~27GPa and at room T. This implies that the P effect alone at room T is enough to create an unstable state in the electronic structure of Nb capable of causing electron redistribution and consequently a shift in Fermi level position.

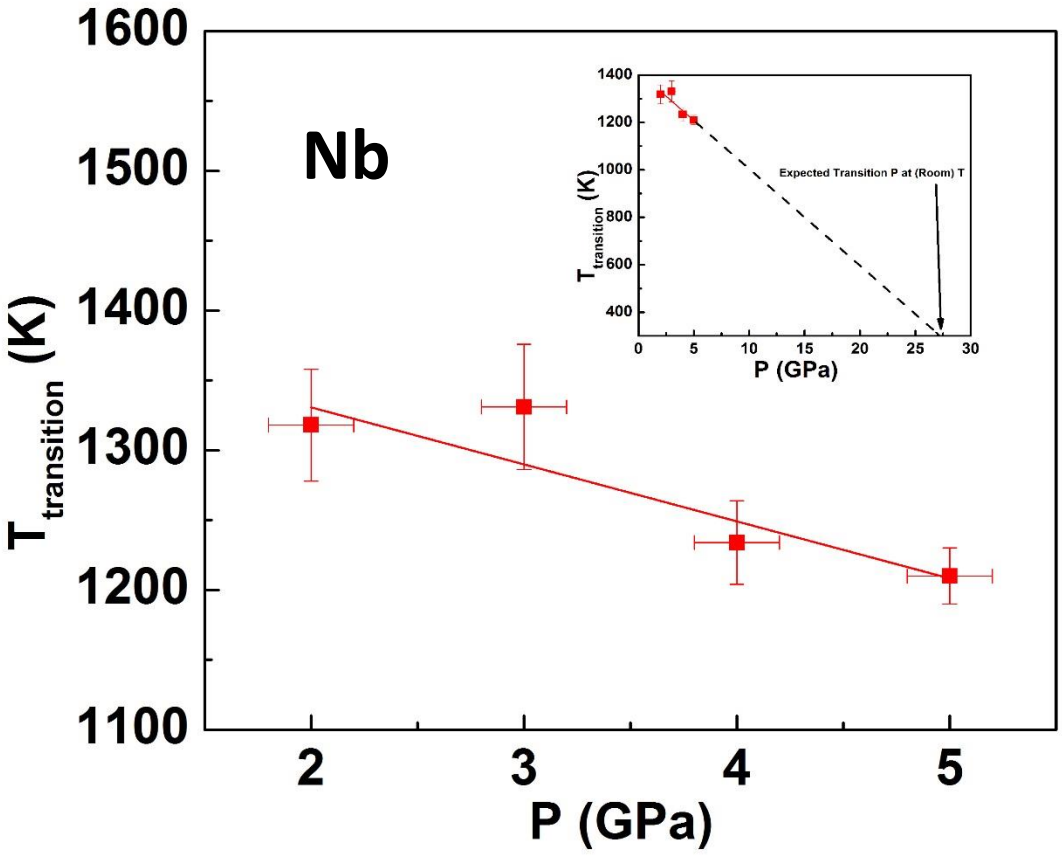

Figure 5.4. Pressure dependence of minus to plus group transition temperature in Nb. Insert is the least square fit of the pressure dependence extrapolated to room temperature.

As expected, the resistivity of Nb decreases with increasing P in the solid state as shown by the P-dependence of resistivity at three different isotherms plotted in Figure 5.5. Investigation of electrical resistivity of Nb as a function of P and T by Neve et al. [32] in the region of (273-313) K and (0-1) GPa appears to be the only available data on the electrical resistivity of Nb at combined P and T conditions. The P-coefficient of resistivity of these data, computed from the resistance measurement of Neve et al. [32], using a geometric factor which was calculated using the resistance data in conjunction with the corresponding 1atm resistivity value as measured by Tye [24], compared well with the result computed at 300K as shown in the insert in Figure 5.5.

The determined values of the P-coefficient of resistivity, $\left(\frac{\partial \ln \rho}{\partial P}\right)_T$, at 300K, 1200K and 1500K isotherms are (-0.0563 $\pm$ 0.014)GPa^{-1}, (-0.11 $\pm$ 0.002)GPa^{-1} and (-0.095 $\pm$ 0.005)GPa^{-1} respectively. Comparison of these values with the same parameter calculated using the relationship derived by Stacey and Anderson [28] was made:

$$\left(\frac{\partial \ln \rho}{\partial P}\right)_T = \frac{-2(\gamma - 1/3)}{K_T} \quad (1)$$

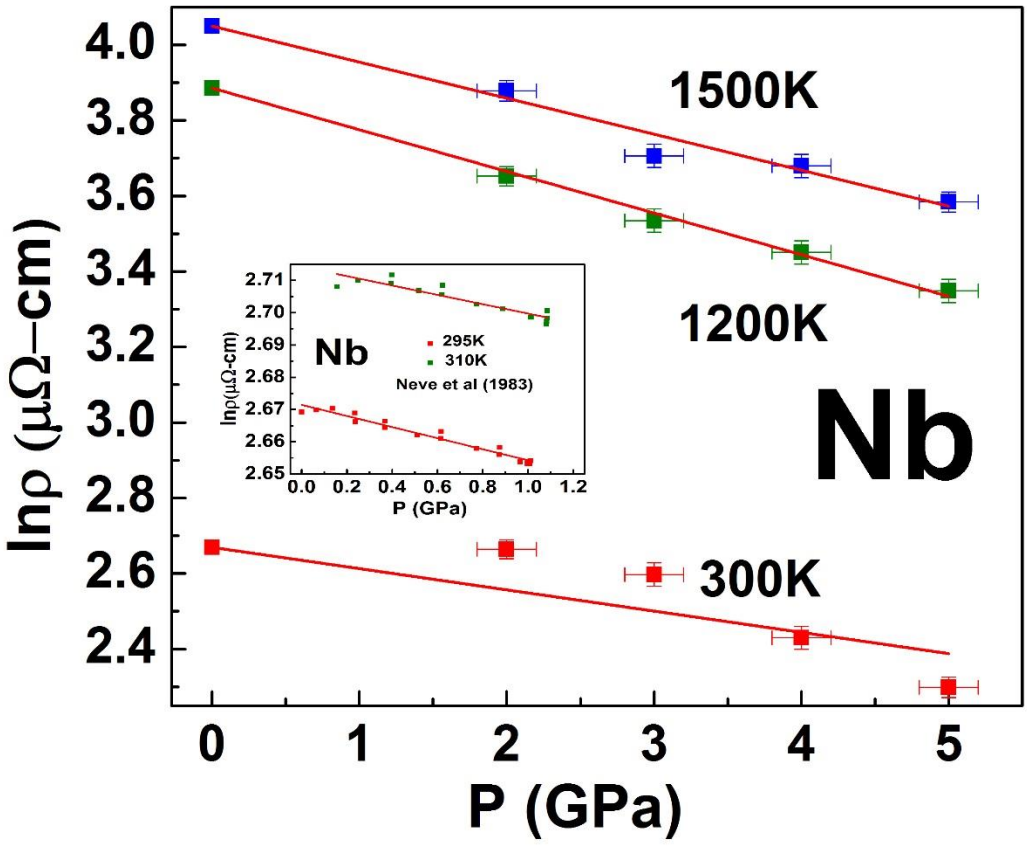

Figure 5.5. Pressure dependence of electrical resistivity of Nb in the solid state along the 1500K 1200K and 300K isotherms. The calculated slopes for the pressure coefficient of resistivity of the fitted lines are $(d\ln\rho/dP)_T$ at 300K, 1200K and 1500K are (-0.056 $\pm$ 0.014)GPa^{-1} GPa^{-1}, (-0.11$\pm$ 0.002) GPa^{-1} and (-0.095$\pm$ 0.005) GPa^{-1} for the respectively isotherms. Data at 1 atm are from Tye [24]. The insert is resistance data from Neve et al. (1983) normalized to resistivity value from Tye [24] at the corresponding T. The computed slopes for the Neve data at 295K and 310K are -0.017 $\pm$ 0.0009 GPa^{-1} and -0.015 $\pm$ 0.0017GPa^{-1} respectively.

where K_T is the isothermal bulk modulus and γ is the Grüneisen parameter. Using a K_T value of 174GPa at room T and applying a T-derivative of K_T of -0.06GPa K^{-1}, derived from an in-situ x-ray diffraction study [29], K_T was calculated at isotherms 300K, 1200K and 1500K to be 156GPa, 102GPa and 84GPa respectively. Using a value for γ of 1.35 for Nb at room T [30], which would not differ much at higher temperatures considering that γ is almost constant at high T above the Debye T [30], calculated values were -0.013 GPa^{-1}, -0.020 GPa^{-1} and -0.024 GPa^{-1} for the 300K, 1200K and 1500K isotherms for $(d\ln\rho/dP)_T$ respectively. The experimentally determined and calculated values at 300K are fairly comparable. However, at 1200K, the experimentally determined value is higher than predicted by a factor of approximately 5. This might be caused by the influence of the electronic transition from the minus group to plus group as 1200K isotherm is within this region. Alternatively, the errors in values used for K_T and γ may also increase at high T leading to inaccuracy in the calculated values.

In a metal, the propagation of electrons carries heat energy along with charge and hence the electronic thermal conductivity of a metal can be determined through its electrical resistivity using the Wiedemann-Franz law [31], $k_e = \frac{LT}{\rho}$, where L is the Lorenz number. The contribution of the electronic thermal conductivity in a metal dominates over the phonon contribution in the total thermal conductivity at high T above the Debye T, therefore understanding the total thermal conductivity largely depends on understanding the electronic component. Direct measurements of the total thermal conductivity at high P,T are desirable, however, the experimental challenges make this difficult. Thus, its indirect determination through resistivity measurements is preferred. Using the Sommerfeld value of L, the T-dependence of k_e of Nb at four P values were determined as shown in Figure 5.6. Results of k_e determined from this study were compared with that calculated using the 1atm electrical resistivity data of Tye [24] and the Sommerfeld value of L.

The electronic thermal conductivity increases with increasing T up to the electronic transition T for all P investigated. However, above the transition T, k_e remains constant with increasing T at 2GPa but k_e has an increasingly negative slope with T at P above 2GPa. Plotted in Figure 5.6 for comparison are the recommended values of total thermal conductivity, k_{total}, at 1atm from experimental studies as collected in Touloukian [33]. The 1atm experimental values of k_{total} are higher than the values of k_e calculated from 1atm electrical resistivity data using the Wiedemann-Franz Law. This suggests that the Sommerfeld value of L is valid for Nb for this T-range.

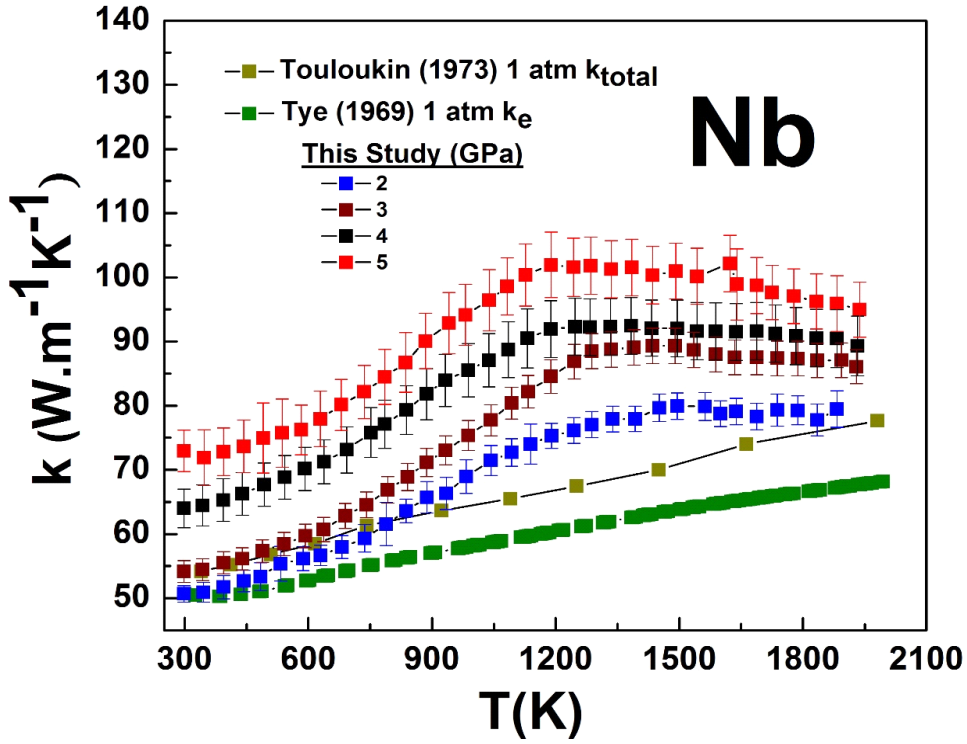

Figure 5.6. Temperature dependence of the thermal conductivity at 2-5GPa. The electronic component (k_e) was calculated from the electrical resistivity data using the Wiedemann-Franz law and the Sommerfeld value of the Lorenz number. Comparison is made with the electronic thermal conductivity based on resistivity data at 1 atm from Tye [24] and with the total thermal conductivity (k_{total}) from experimental measurements reported in Touloukian [36].

The P-dependence of k_e is plotted at 300K, 1200K and 1500K isotherms as shown in Figure 5.7. The P-coefficient of k_e increases with increasing P up to 5GPa reached in this study. P-coefficient of k_e, $\left(\frac{\partial \ln k_e}{\partial P}\right)_T$ of 0.051 $\pm$ 0.015 GPa^{-1}, 0.105 $\pm$ 0.001 GPa^{-1}, and 0.095 $\pm$ 0.004 GPa^{-1} were determined for 300K, 1200K and 1500K isotherms respectively, as shown in Figure 5.7. These values were compared with the same parameter calculated using the relationship derived by Bohlin [59] given in Eqn (2), which is similar to Eqn 1 for electrical resistivity:

$$\left(\frac{\partial \ln k_e}{\partial P}\right)_T = \frac{(2\gamma - 1/3)}{K_T} \tag{2}$$

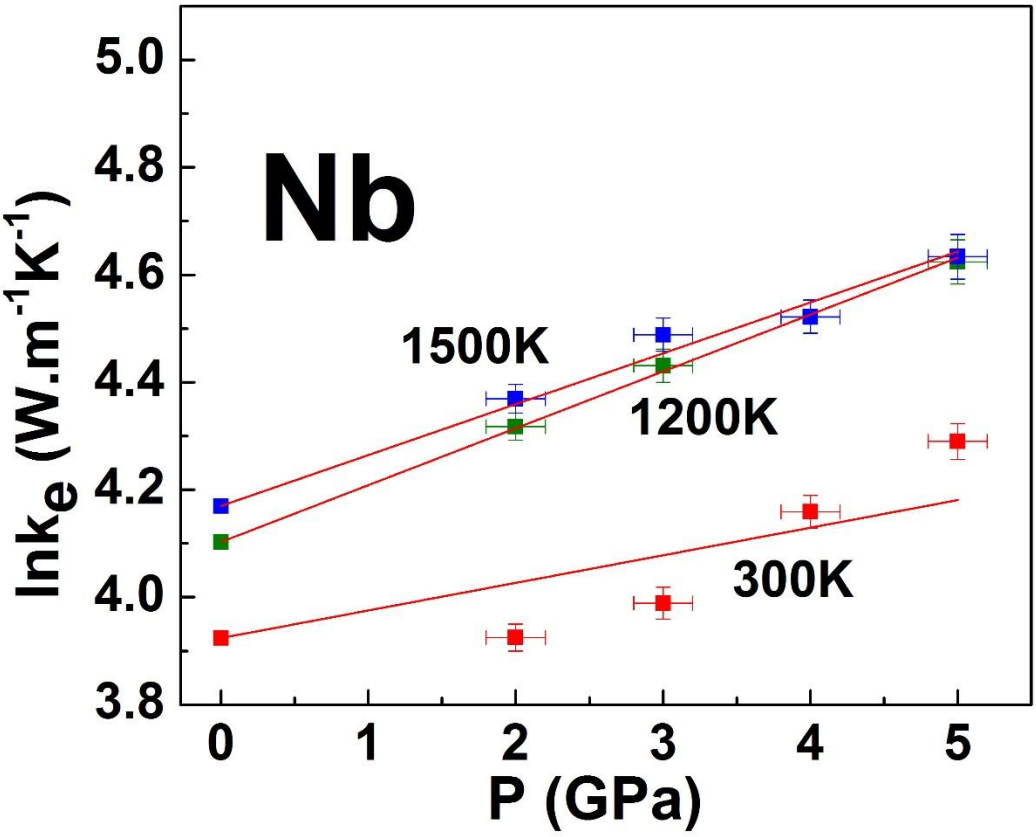

Figure 5.7. P-dependence of thermal conductivity of Nb at 300K, 1200K and 1500K isotherms. The calculated slopes for the pressure coefficient of electronic thermal conductivity k_e, $(d\ln\rho/dP)_T$ are (0.051 $\pm$ 0.015) GPa^{-1}, (0.105 $\pm$ 0.001) GPa^{-1} and (0.095 $\pm$ 0.004) GPa^{-1} for the respective isotherms. Data at 1atm are from Tye [24].

Values of 0.015GPa^{-1}, 0.023GPa^{-1} and 0.028GPa^{-1} were caluclated for 300K, 1200K and 1500K isotherms respectively. The predictions of $(\partial \ln k_e / \partial P)_T$ by Eqn (2) for the 300K, 1200K and 1500K isotherms are in reasonable agrrement but lower than the experimental vlaues by ~30%, 22%, and 30%, respectively.

5.3. Conclusions

The T-dependence of electrical resistivity of Nb in the solid state up to ~1900K has been investigated up to 5GPa. At fixed P, the T-dependence of electrical resistivity undergoes an electronic transition from the minus group to the plus group with increasing T. The transition T decreases with increasing P. The extrapolated value of the electronic transition T versus P, suggests that Nb will transform from a minus group metal to a plus group metal at room T at ~27GPa. The electrical resistivity decreases as a function of P on any given isotherm, as expected. These findings are interpreted in terms of the effects of P and T on the Fermi surface and displacement of the relative position of the s and *d* bands to the Fermi level position. The electronic thermal conductivity was calculated using the Wiedemann-Franz law using the Sommerfeld value of the Lorenz number. . The T-dependence of k_e increases with increasing T up to the transition T at all fixed P. However, above the transition T, k_e remains constant with increasing T at fixed 2GPa but at higher P, k_e has an increasingly negative slope. The P-dependence of k_e increased with increasing P up to 5GPa reached in this study.

5.4 References

[1] Getzlaff, M. (2007). Fundamentals of magnetism. *Springer Science and Business Media*. p 3.

[2] Stoner, E. C. (1936). Collective electron specific heat and spin paramagnetism in metals. Proceedings of the Royal Society of London. Series A, *Mathematical and Physical Sciences*, 154(883), 656-678.

[3] Shimizu, M., Takahashi, T., and Katsuki, A. (1962). Calculations of electronic specific heat and paramagnetic susceptibility of Chromium. *Journal of the Physical Society of Japan*, 17(11), 1740-1746.

[4] Aisaka, T., and Shimizu, M. (1970). Electrical resistance, thermal conductivity and thermoelectric power of transition metals at high temperatures. *Journal of the Physical Society of Japan*, 28(3), 646-654.

[5] Mott, N. F. (1936). The electrical conductivity of transition metals. In *Proceedings of the Royal Society of London A: Mathematical, Physical and Engineering Sciences* (Vol. 153, No. 880, pp. 699-717). The Royal Society.

[6] Mott, N. F. (1964). Electrons in transition metals. *Advances in Physics*, 13(51), 325-422.

[7] Lomer, W. M. (1962). Electronic structure of chromium group metals. *Proceedings of the Physical Society*, 80(2), 489.

[8] Wood, J. H. (1962). Energy bands in iron via the augmented plane wave method. *Physical Review*, 126(2), 517.

[9] Mattheiss, L. F. (1965). Fermi surface in tungsten. *Physical Review*, 139(6A), A1893.

[10] Deegan, R. A., and Twose, W. D. (1967). Modifications to the orthogonalized-plane-wave method for use in transition metals: Electronic band structure of niobium. *Physical Review*, 164(3), 993.

[11] Halloran, M. H., Condon, J. H., Graebner, J. E., Kunzier, J. E., and Hsu, F. S. L. (1970). Experimental study of the fermi surfaces of niobium and tantalum. *Physical Review B*, 1(2), 366.

[12] Mattheiss, L. F. (1970). Electronic structure of niobium and tantalum. *Physical Review B*, 1(2), 373.

[13] Euwema, R. N. (1971). Plane-wave-Gaussian energy-band study of Nb. *Physical Review* B, 4(12), 4332.

[14] Fong, C. Y., and Cohen, M. L. (1973). Pseudopotential calculation of the electronic structure of a transition metal-niobium. *Physics Letters A*, 44(5), 375-376.

[15] Ho, K. M., Louie, S. G., Chelikowsky, J. R., and Cohen, M. L. (1977). Self-consistent pseudopotential calculation of the electronic structure of Nb. *Physical Review B*, 15(4), 1755.

[16] Boyer, L. L., Papaconstantopoulos, D. A., and Klein, B. M. (1977). Effect of self-consistency and exchange on the electronic structure of the transition metals, V, Nb, and Ta. Physical Review B, 15(8), 3685.

[17] Shein, K. I., Shein, I. R., Medvedeva, N. I., Shalaeva, E. V., Kuznetsov, M. V., and Ivanovskii, A. L. (2006). Effects of atomic relaxation and the electronic structure of niobium (100) and (110) surfaces. *The Physics of Metals and Metallography*, 102(6), 604-610.

[18] Anderson, J. R., Papaconstantopoulos, D. A., and Schirber, J. E. (1981). Influence of pressure on the Fermi surface of niobium. *Physical Review B*, 24(12), 6790.

[19] Young, D. A. (1991). Phase diagrams of the elements. *Univ of California Press*. p 172.

[20] Templeton, I. M. (1974). The effect of hydrostatic pressure on the fermi surfaces of copper, silver, and gold. II. High precision studies. *Canadian Journal of Physics*, *52*(17), 1628-1634.

[21] Struzhkin, V. V., Timofeev, Y. A., Hemley, R. J., and Mao, H. K. (1997). Superconducting Tc and electron-phonon coupling in Nb to 132 GPa: magnetic susceptibility at megabar pressures. *Physical Review Letters*, *79*(21), 4262.

[22] Ostanin, S. A., Trubitsin, V. Y., Savrasov, S. Y., Alouani, M., and Dreyssé, H. (2000). Calculated Nb superconducting transition temperature under hydrostatic pressure. *Computational Materials Science*, *17*(2), 202-205.

[23] Landrum, G. A., and Dronskowski, R. (2000). The orbital origins of magnetism: from atoms to molecules to ferromagnetic alloys. *Angewandte Chemie International Edition*, *39*(9), 1560-1585.

[24] Veselago, V. G., and Vinokurova, L. I. (1988). The magnetic and electron structures of transition metals and alloys (Vol. 3). *Nova Publishers*, page 154.

[25] Tye, R. P. (1961). Preliminary measurements on the thermal and electrical conductivities of molybdenum, niobium, tantalum and tungsten. *Journal of the Less Common Metals*, 3(1), 13-18.

[26] Secco, R. A. (1995). High p, T physical property studies of Earth's interior: Thermoelectric power of solid and liquid Fe up to 6.4 GPa. *Canadian Journal of Physics*, 73(5-6), 287-294.

[27] Secco, R. A., and Schloessin, H. H. (1986). On- line p, T calibration based on well- known phase transitions. *Journal of Applied Physics*, 60(5), 1625-1633.

[28] Stacey, F. D., and Anderson, O. L. (2001). Electrical and thermal conductivities of Fe–Ni–Si alloy under core conditions. *Physics of the Earth and Planetary Interiors*, *124*(3), 153-162.

[29] Zou, Y., Qi, X., Wang, X., Chen, T., Li, X., Welch, D., and Li, B. (2014). High-pressure behavior and thermoelastic properties of niobium studied by in situ x-ray diffraction. *Journal of Applied Physics*, 116(1), 013516.

[30] Barron, T. H. K. (1955). On the thermal expansion of solids at low temperatures. *The London, Edinburgh, and Dublin Philosophical Magazine and Journal of Science*, *46*(378), 720-734.

[31] Franz, R., and Wiedemann, G. (1853). Ueber die Wärme-Leitungsfähigkeit der Metalle. *Annalen der Physik*, 165(8), 497-531.

[32] Neve, J., Sundqvist, B., and Rapp, Ö. (1983). Electron band structure, resistivity, and the electron-phonon interaction for niobium under pressure. *Physical Review B*, 28(2), 629.

[33] Touloukian, Y. S., Powell, R. W., Ho, C. Y., and Nicolaou, M. C. (1974). Thermophysical Properties of Matter-The TPRC Data Series. Volume 10. Thermal Diffusivity. Thermophysical and electronic properties information analysis center.

Chapter 6: Conclusion

6.0 General Conclusion

The electrical resistivity of high purity Cu, Zn and Co has been measured at pressures (P) up to 5GPa in a large volume press and at temperatures (T) up to ~200K into the liquid phase. Solid state electrical resistivity of Nb was also measured at P up to 5GPa and at T up to ~1900K. The results are summarised below:

- Cu resistivity decreases along the melting boundary
- Zn resistivity is constant along the melting boundary
- Co resistivity is constant along the melting boundary
- Nb undergoes an electronic transition at high T that decreases as P is increased.

The experiments utilized a four-wire technique and polarity switch. Comparisons with 1atm studies were generally in good agreement. Using the Wiedemann-Franz law with the Sommerfeld value for the Lorenz number, electronic thermal conductivity (k_e) was calculated from resistivity data for each of the four metals.

6.1 Filled *d*-band Metals: Cu and Zn

The electrical resistivity at the melting T of Cu decreased as a function of P up to 5GPa in contrast to theoretical prediction of resistivity invariance [1] along its melting boundary. In Cu, the distance of separation between the *d*-band and the Fermi level (E_{fd}) increases with increasing P. Although, the onset of melting is accompanied with a change from long to short range structural order which is manifested in the abrupt change in electrical resistivity, E_{fd} is unaffected by the melting process. This suggests that in addition to the normal antagonistic effects of P and T on resistivity, the effect of P on E_{fd} at the melting boundary could explain the decreasing resistivity

of Cu with increasing P along the melting boundary as observed in this study. The calculated k_e increased with increasing P both in the solid and liquid state. However, at fixed P, k_e decreased with increasing T in the solid state and increased with increasing T in the liquid state.

The electrical resistivity of Zn remained constant along the melting boundary up to 5GPa. These findings were interpreted in terms of the antagonistic effects of P and T on the electronic structure of liquid Zn. The Fermi surface of Zn extends to the third Brillouin zone which results in a complex Fermi surface. The Fermi level of Zn is located within the filled *d*-band in contrast to Cu with its *d*-band located below the Fermi level. Owing to the complexity of the Fermi surface of Zn, an *s*-*d* hybridized network is formed. From the effects of P and T on the *s*-*d* hybridization, spin-orbit splitting, amplitude of phonon vibration and Fermi surface topology, the respective resistivity decrease and increase with P and T appear to compensate each other at the melting boundary as predicted [1]. The k_e of Zn increased both in the solid and liquid state. However, with increasing T, k_e decreased in the solid state and increased with increasing T in the liquid state.

The resistivity of Zn and Cu along their respective melting boundaries behaves differently even though they both have filled *3d*-band states. This suggests that the criterion for electrical resistivity invariance cannot be only ascribed only to the state of filling of *d*-band as theories suggested. The position of the *d*-band relative to the Fermi level and the complexity of the Fermi surface and its volume relationship with the Brillouin Zone appears to play a role. These factors will determine if the *d* electrons will hybridize with the conduction *s* electrons as in the case of Zn or unhybridize in the opposite case of Cu. The P effect on the electrical resistivity of metals with a filled *d*-band at the melting boundary appears to be dictated by the presence of *s*-*d* hybridization or non *s*-*d* hybridization around the Fermi surface. In the hybridized case of Zn, it is expected that

increasing P would lead to increasing hybridization hence increase resistivity. However, in non-hybridized case of Cu, increasing P leads to increasing E_{fd} and hence a decrease resistivity.

6.2 Unfilled d-band metal: Co

The electrical resistivity of Co measured up to 5GPa demonstrated that its resistivity also remained constant along its melting boundary similar to Zn. This was interpreted in terms of the cancelling effects of the reduction in the amplitude of lattice vibrations with increasing P, tending to decrease resistivity, and the P-induced increase in *d*-resonance bringing the Fermi level closer to the *d*-resonance energy, which tends to increase resistivity. T seems to have little effect on the electronic structure of Co on melting. These results disagree with the prediction of the revised theory by Stacey and Loper [2] and tend to favor the earlier theory by Stacey and Anderson. However, the assumption made by Stacey and Anderson on the mobility of *d*-electrons being comparable to *s* electrons disagrees with theories which accounted very well for the electrical resistivity of unfilled *d*-band liquid transition metals through *d*-resonance scattering in the modified Ziman nearly free electron model. The calculated k_e from resistivity data showed an increasing trend with increasing P both in the solid and liquid state, but upon T increase, k_e decreases in the solid and increases in the liquid state.

6.3 Nb

The electrical resistivity of solid Nb was measured up to ~1900K and 5GPa. The expected resistivity decrease with P and increase with T was observed. However, at fixed P, an electronic transition from the 'minus group' to 'plus group' was observed in the T-dependence of resistivity at high T. The transition was discussed in terms of the effects of P and T on the electronic band structure of Nb. It is likely that P causes a metal-stable state in the spin sub-bands of Nb by increasing separation of the *s* and *d* bands relative to the Fermi level. At fixed P and with increasing

T, the meta-stability increases and eventually leads to redistribution of electrons in an attempt to achieve a stable chemical potential. The position of the Fermi level changes from its initial position in a region of high density of states to a position in a region of low density of states as electrons are redistributed. With P effect also causing anisotropy in the Fermi surface of Nb due to the differences in the compressibility of Fermi surface components combined with the new position of the Fermi level in the region of low density of density, the conditions allow for Nb to transition to a similar electronic structure at ambient conditions of the 'plus group' metals. Hence, at high P and T, Nb behaves like the 'plus group' metals with a concave T- dependence of electrical resistivity at 1atm.

6.4 Implications for the Thermal Conductivity of the Earth's Inner Core Boundary

From the T-dependence of electrical resistivity of liquid state Co at fixed P range up to 5GPa from this study, the results demonstrate invariance in the electrical resistivity along the Co melting boundary. Since Fe is an electronic analog of Co, this could imply that the k_{total} of the ICB may be similar to k_{Fe} at 1 atm at the melting point of ~33 $Wm^{-1}K^{-1}$ [3, 4]. This agrees with the result of direct measurement of solid Fe by Konôpková et al. [5] which placed the k_{total} of the Earth's core near the low end of previous estimates at (18-44)$Wm^{-1}K^{-1}$. A low value of k_{core} implies that the age of the inner core may be old and that the geodynamo may have had an energy source from compositionally-induced convection since the birth of the inner core. In addition, thermal convection may have played a role in sustaining the geodynamo before the birth of the inner core.

6.5 Future Work

The electronic structure of Ag and Au are similar to that of Cu with a neck feature on their individual Fermi surfaces making contact with the Brillouin Zone boundary. Previous experimental work demonstrated that with increasing P, E_{fd} increases in Ag similar to that of Cu

[6]. No such experiment was found in literature for the case of Au. However, considering the similarity in the electronic structure of Cu, Ag and Au, it is expected that the Fermi surface of Au would be similar. Hence, the electrical resistivity of Ag and Au along their melting boundaries should be investigated, for comparison with the results of Cu. This will help in the classification of the electrical resistivity of these metals on their melting boundary in relation to their electronic character.

Zn and Cd have similar electronic structure whose Fermi surfaces extend beyond the first Brillouin Zone. Investigation of the electrical resistivity of Cd along its P-dependent melting boundary would also be helpful in classification of the electrical resistivity of these metals on their melting boundary in relation to their electronic character.

Ultimately, the electrical resistivity of Fe along its P-dependent melting boundary should be investigated which will help in the estimation of the k_{total} of the ICB of the Earth.

Finally, the electrical resistivity of the 'minus' and 'plus group' paramagnetic metals should be investigated at high P and T conditions to further characterize their electron-electron, phonon-electron relationship and the phase state of these metals. Specifically, the prediction in the current work that Nb will behave as a 'plus group' metal at P higher than 27GPa should be tested.

6.6 References

[1] Stacey, F. D., and Anderson, O. L. (2001). Electrical and thermal conductivities of Fe–Ni–Si alloy under core conditions. *Physics of the Earth and Planetary Interiors*, *124*(3), 153-162.

[2] Stacey, F. D., and Loper, D. E. (2007). A revised estimate of the conductivity of iron alloy at high pressure and implications for the core energy balance. *Physics of the Earth and Planetary Interiors*, *161*(1), 13-18.

[3] Zinov'yev, V. E., Polev, V. F., Taluts, S. G., Zinov'yeva, G. P., and Il'inykh, S. (1986). Diffusivity and Thermal Conductivity of 3 d-Transition Metals in Solid and Liquid States. *Phys. Met. Metallogr.(USSR)*, *61*(6), 85-9.

[4] Nishi, T., Shibata, H., Waseda, Y., and Ohta, H. (2003). Thermal conductivities of molten iron, cobalt, and nickel by laser flash method. *Metallurgical and Materials Transactions A*, *34*(12), 2801-2807.

[5] Konôpková, Z., McWilliams, R. S., Gómez-Pérez, N., and Goncharov, A. F. (2016). Direct measurement of thermal conductivity in solid iron at planetary core conditions. *Nature*, *534*(7605), 99-101.

[6] Zallen, R. (1966). The effect of pressure on optical properties of the noble metals. *optical properties and electronic structure of metals and alloys: Proceedings of the International Colloquim*, 164.

Appendix 1– Cell Design

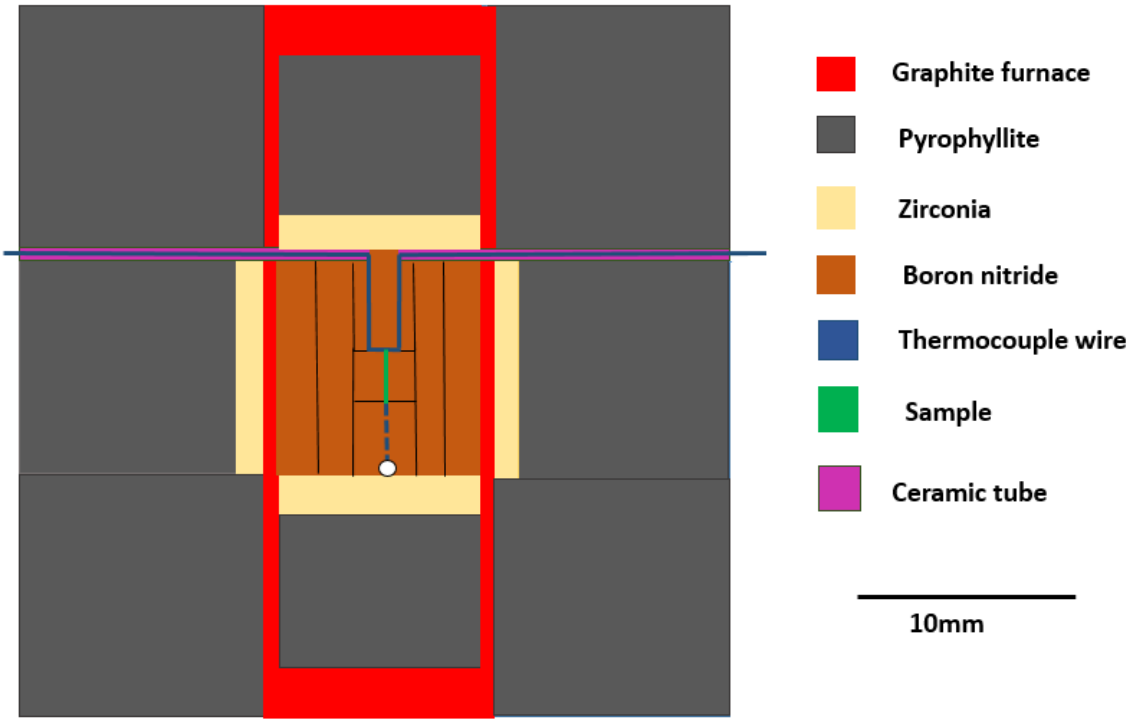

A1.1 Schematic drawing of cube section with components parts.

Appendix 2– Microprobe Results

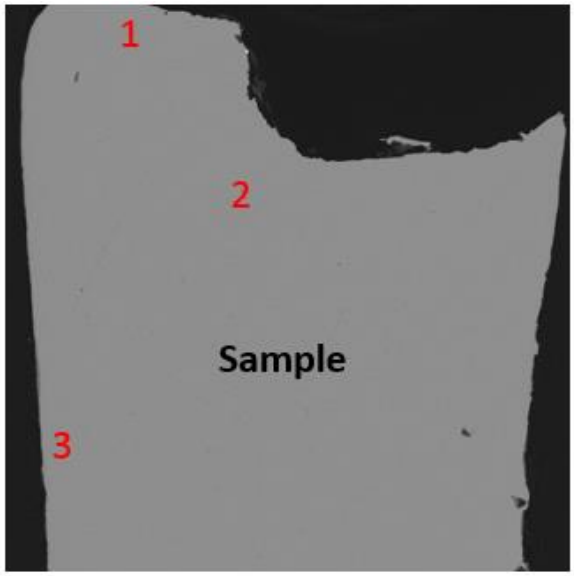

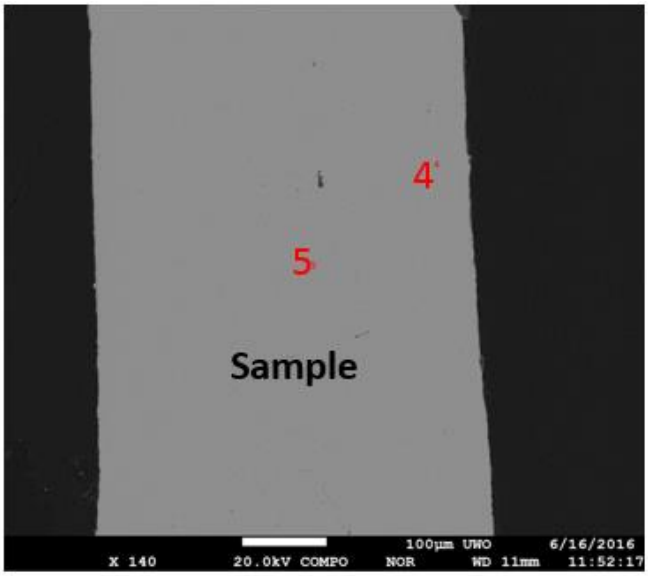

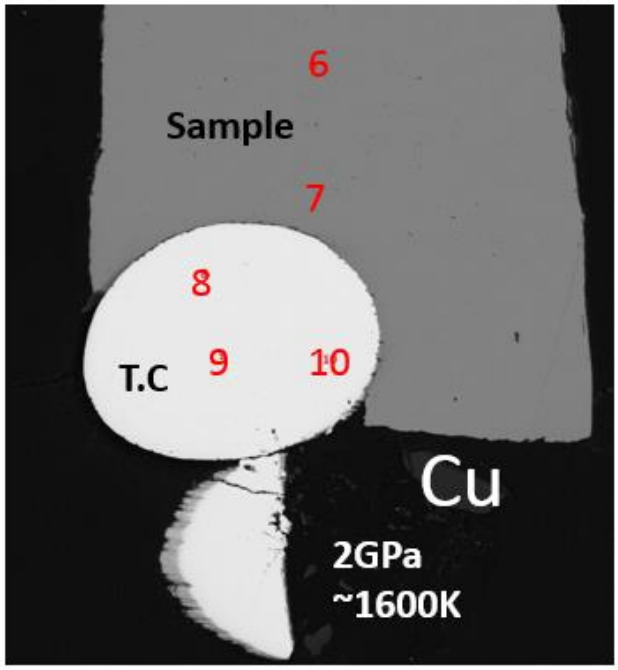

Points	Comments	W (Mass %)	Cu (Mass %)	Re (Mass %)	Total (Mass %)
1	Cu_2GPa-01	0.017	99.192	ND	99.209
2	Cu_2GPa-02	0.074	101.252	ND	101.326
3	Cu_2GPa-03	0.068	98.929	0.007	99.004
4	Cu-2GPa-04	0.101	99.413	ND	99.514
5	Cu-2GPa-05	0.034	101.173	0.034	101.241
6	Cu-2GPa-06	0.078	99.853	ND	99.931
7	Cu-2GPa-07	0.087	100.027	0.022	100.136
8	Cu-2GPa-08	73.74	0.008	25.4	99.148
9	Cu-2GPa-09	73.502	-0.006	25.24	98.736
10	Cu-2GPa-10	73.5	ND	25.146	98.646

A2.1. Back scattered electron images of recovered Cu at 2GPa and ~1600K, alongside tabulated microprobe results. T.C. is thermocouple.

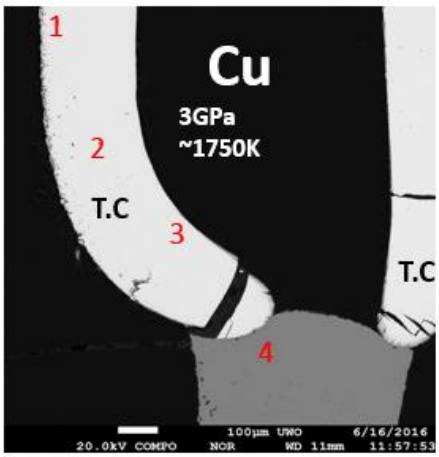

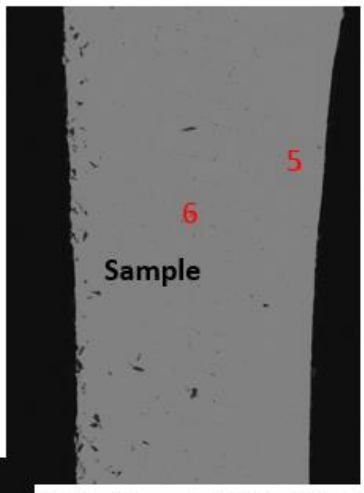

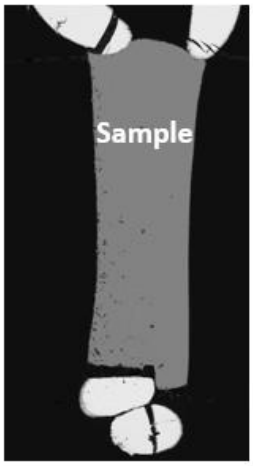

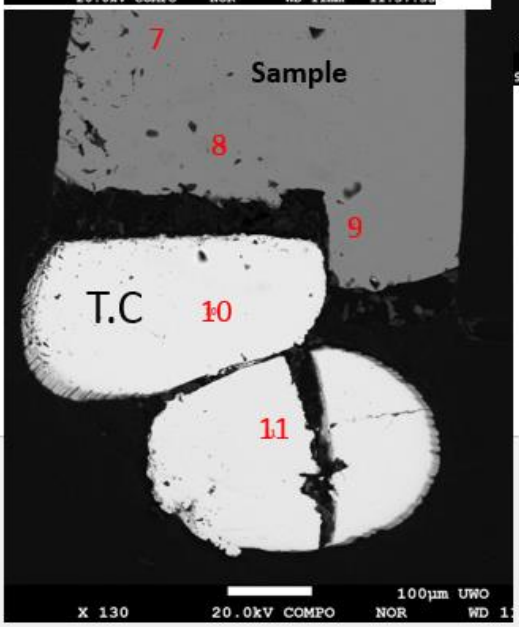

Points	Comments	W (Mass %)	Cu (Mass %)	Re (Mass %)	Total (Mass %)
1	Cu-3GPa-01	92.87	ND	5.809	98.679
2	Cu_3GPa-02	92.996	ND	6.981	99.977
3	Cu_3GPa-03	93.999	0.008	6.616	100.623
4	Cu_3GPa-04	0.065	100.214	ND	100.279
5	Cu_3GPa-05	0.085	99.381	ND	99.466
6	Cu_3GPa-06	0.068	100.654	ND	100.722
7	Cu_3GPa-07	0.086	100.007	ND	100.093
8	Cu_3GPa-08	0.096	100.221	ND	100.323
9	Cu_3GPa-09	0.059	100.221	0.018	100.293
10	Cu_3GPa-10	74.082	ND	25.206	99.288
11	Cu_3GPa-11	93.489	ND	6.491	99.98

A2.2. Back scattered electron images of recovered Cu at 3GPa and ~1750K, alongside tabulated microprobe results.

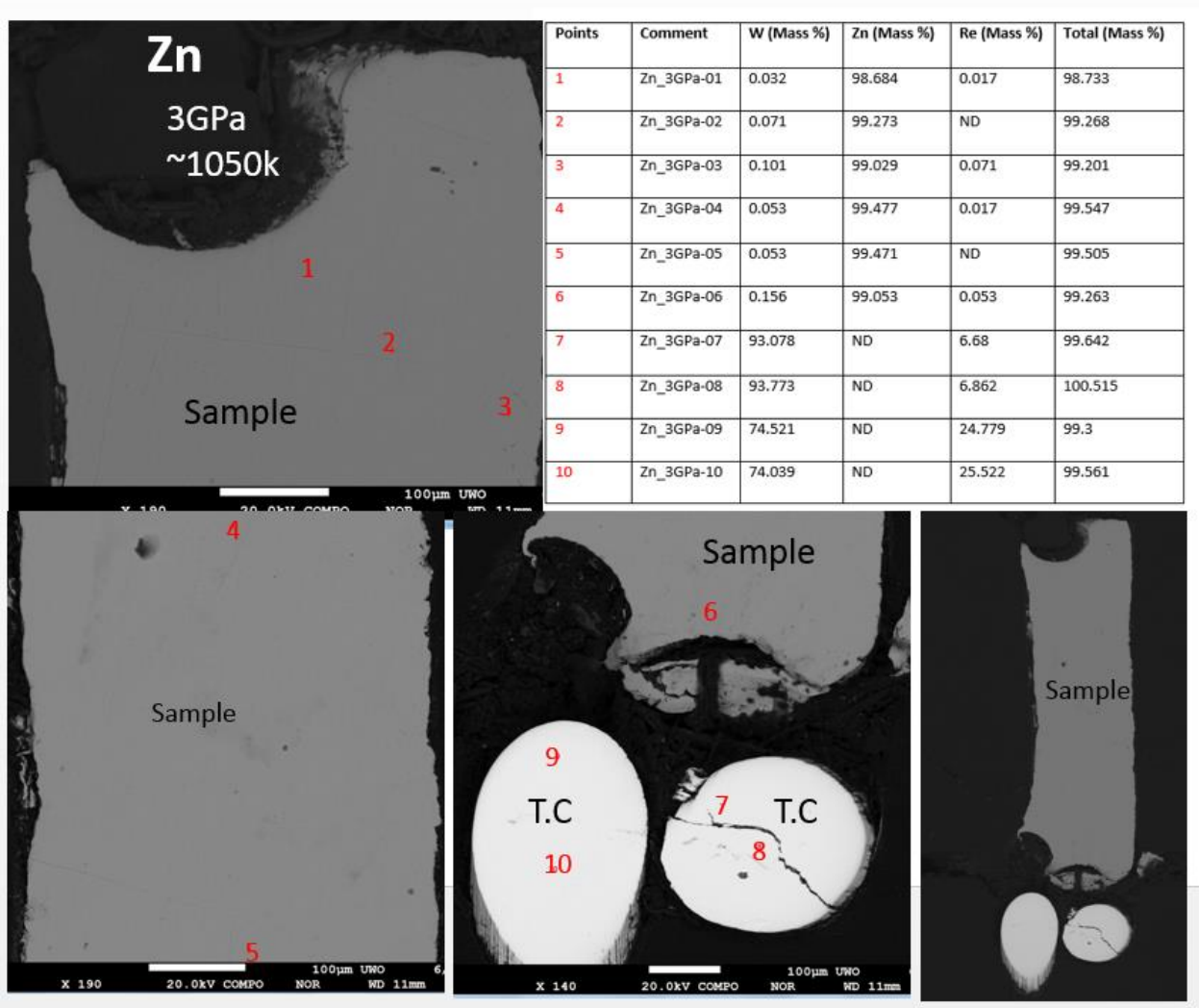

Points	Comment	W (Mass %)	Zn (Mass %)	Re (Mass %)	Total (Mass %)
1	Zn_3GPa-01	0.032	98.684	0.017	98.733
2	Zn_3GPa-02	0.071	99.273	ND	99.268
3	Zn_3GPa-03	0.101	99.029	0.071	99.201
4	Zn_3GPa-04	0.053	99.477	0.017	99.547
5	Zn_3GPa-05	0.053	99.471	ND	99.505
6	Zn_3GPa-06	0.156	99.053	0.053	99.263
7	Zn_3GPa-07	93.078	ND	6.68	99.642
8	Zn_3GPa-08	93.773	ND	6.862	100.515
9	Zn_3GPa-09	74.521	ND	24.779	99.3
10	Zn_3GPa-10	74.039	ND	25.522	99.561

A2.3. Back scattered electron images of recovered Zn at 3GPa and ~1050K, alongside tabulated microprobe results.

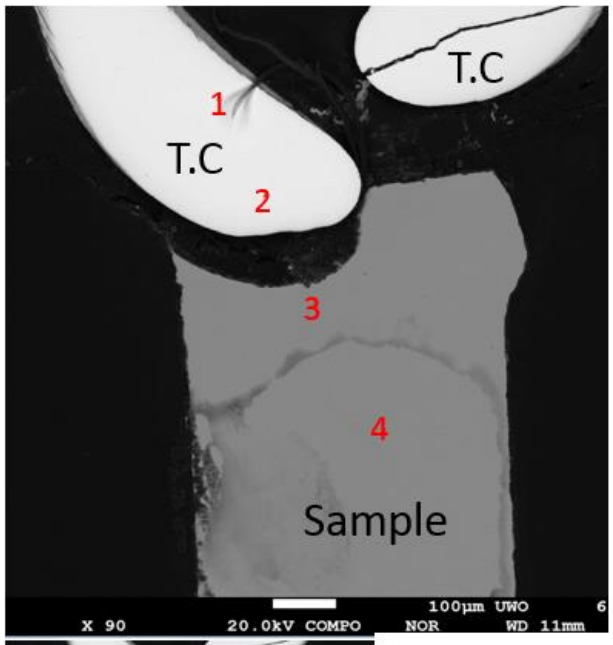

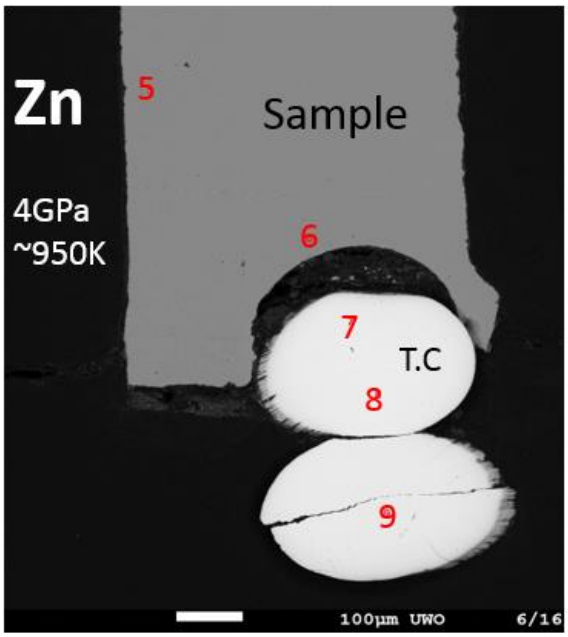

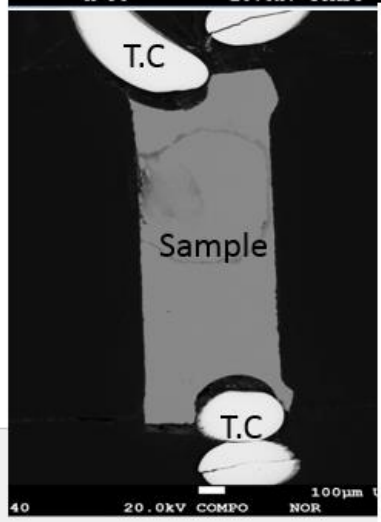

Points	Comment	W (Mass %)	Zn (Mass %)	Re (Mass %)	Total (Mass %)
1	Zn_4GPa_01	74.015	ND	25.087	99.102
2	Zn_4GPa_02	73.501	ND	25.812	99.313
3	Zn_4GPa_03	0.071	99.298	0.029	99.398
4	Zn_4GPa_04	0.085	99.153	ND	99.23
5	Zn_4GPa_05	0.072	100.043	0.012	100.127
6	Zn_4GPa_06	0.119	99.452	0.028	99.599
7	Zn_4GPa_07	74.607	ND	25.618	100.225
8	Zn_4GPa_08	73.17	ND	26.14	99.31
9	Zn_4GPa_09	93.317	ND	6.494	99.698

A2.4. Back scattered electron images of recovered Zn at 4GPa and ~950K, alongside tabulated microprobe results.

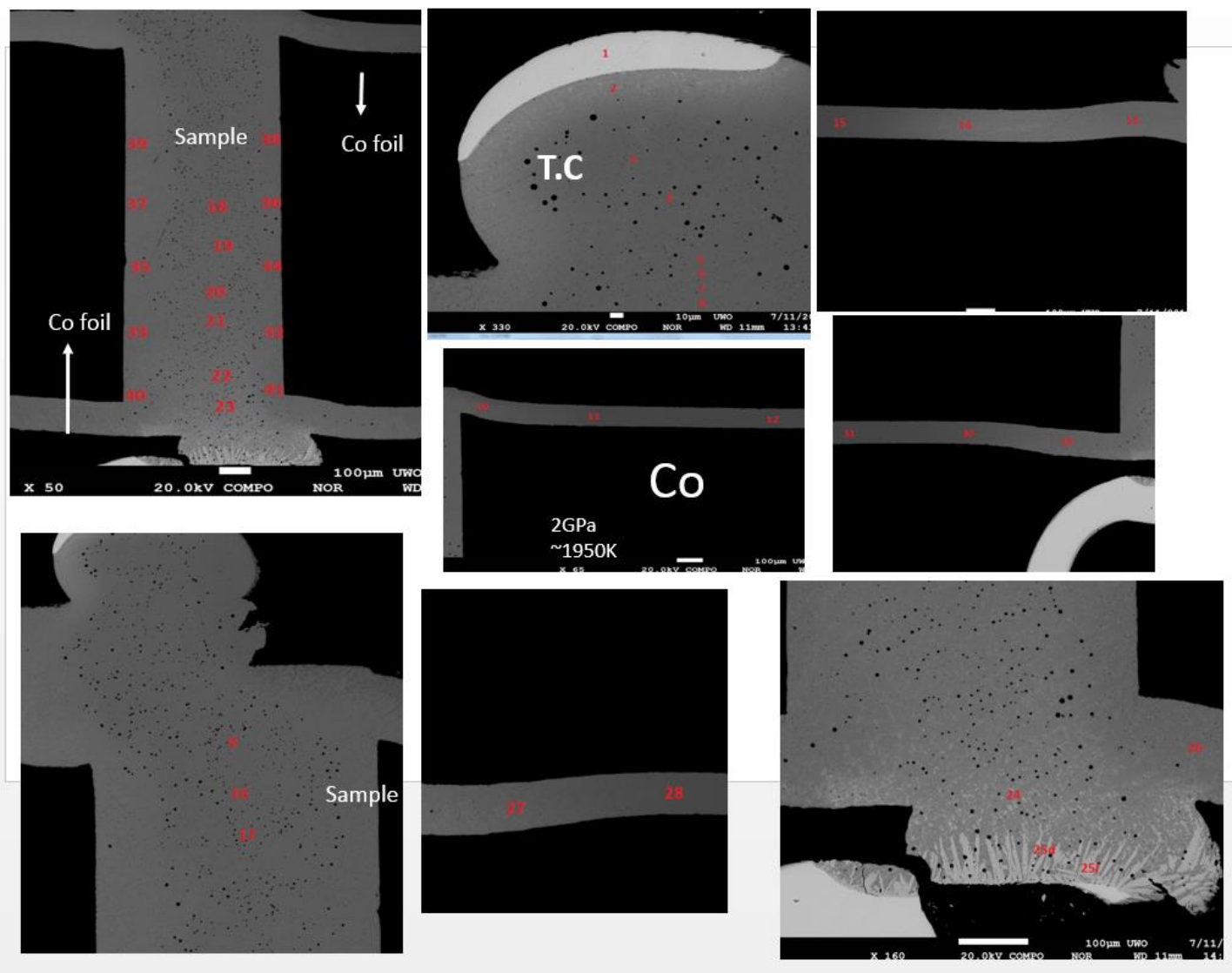

A2.5. Back scattered electron images of recovered Co at 2GPa and ~1950K. T.C position is located at the center above the top end of the sample.

Results of Microprobe Co: 2GPa, 1950K

Point	Comment	W(Mass%)	Co(Mass%)	Re(Mass%)	Total(Mass%)
1	Co_2GPa_05-07-16_01	73.022	0.016	23.489	96.527
2	Co_2GPa_05-07-16_02	31.833	60.096	7.856	99.785
3	Co_2GPa_05-07-16_03	11.728	86.206	1.439	99.373
4	Co_2GPa_05-07-16_04	13.961	84.243	0.792	98.996
5	Co_2GPa_05-07-16_05	12.518	86.544	1.404	100.466
6	Co_2GPa_05-07-16_06	11.891	85.79	1.722	99.403
7	Co_2GPa_05-07-16_07	12.204	84.918	1.673	98.795
8	Co_2GPa_05-07-16_08	12.29	85.471	1.685	99.446
9	Co_2GPa_05-07-16_09	12.514	84.805	2.166	99.485
10	Co_2GPa_05-07-16_10	12.593	85.633	1.388	99.614
11	Co_2GPa_05-07-16_11	2.169	92.644	0.07	94.883
12	Co_2GPa_05-07-16_12	ND	99.942	ND	99.889
13	Co_2GPa_05-07-16_13	19.665	78.401	1.647	99.713
14	Co_2GPa_05-07-16_14	20.028	77.321	1.642	98.991
15	Co_2GPa_05-07-16_15	1.483	98.678	0.097	100.258
16	Co_2GPa_05-07-16_16	12.463	84.681	2.071	99.215
17	Co_2GPa_05-07-16_17	12.615	84.299	2.188	99.102
18	Co_2GPa_05-07-16_18	14.188	82.955	2.653	99.796
19	Co_2GPa_05-07-16_19	14.883	81.802	2.775	99.46
20	Co_2GPa_05-07-16_20	14.991	81.754	3.179	99.924
21	Co_2GPa_05-07-16_21	15.007	81.433	3.317	99.757
22	Co_2GPa_05-07-16_22	20.939	75.939	2.37	99.248
23	Co_2GPa_05-07-16_23	24.769	70.772	3.235	98.776
24	Co_2GPa_05-07-16_24	31.579	63.19	4.465	99.234
25	Co_2GPa_05-07-16_25	35.281	59.589	4.015	98.885
26	Co_2GPa_05-07-16_26	18.538	79.349	1.229	99.116
27	Co_2GPa_05-07-16_27	11.849	87.339	0.727	99.915
28	Co_2GPa_05-07-16_28	4.163	90.847	0.047	95.057
29	Co_2GPa_05-07-16_29	16.693	82.24	1.177	100.11
30	Co_2GPa_05-07-16_30	4.484	94.051	0.09	98.625
31	Co_2GPa_05-07-16_31	0.123	99.305	ND	99.425
32	Co_2GPa_05-07-16_32	16.703	81.71	1.08	99.493
25	Co_2GPa_05-07-16_33	15.531	80.351	3.478	99.36
26	Co_2GPa_05-07-16_26	18.538	79.349	1.229	99.116
27	Co_2GPa_05-07-16_27	11.849	87.339	0.727	99.915
28	Co_2GPa_05-07-16_28	4.163	90.847	0.047	95.057
29	Co_2GPa_05-07-16_29	16.693	82.24	1.177	100.11
30	Co_2GPa_05-07-16_30	4.484	94.051	0.09	98.625
31	Co_2GPa_05-07-16_31	0.123	99.305	ND	99.425
32	Co_2GPa_05-07-16_32	16.703	81.71	1.08	99.493
33	Co_2GPa_05-07-16_33	15.531	80.351	3.478	99.36
34	Co_2GPa_05-07-16_34	14.755	82.126	1.78	98.661
35	Co_2GPa_05-07-16_35	15.584	79.997	3.585	99.166
36	Co_2GPa_05-07-16_36	13.687	83.956	2.102	99.745
37	Co_2GPa_05-07-16_37	15.947	79.265	4.229	99.441
38	Co_2GPa_05-07-16_38	13.889	83.8	1.731	99.42
39	Co_2GPa_05-07-16_39	18.987	77.48	2.148	98.615
40	Co_2GPa_05-07-16_40	20.365	77.477	1.313	99.155

A2.6. Tabulated microprobe results for Co recovered at 2GPa and ~1950, back scattered image is shown in appendix 5.

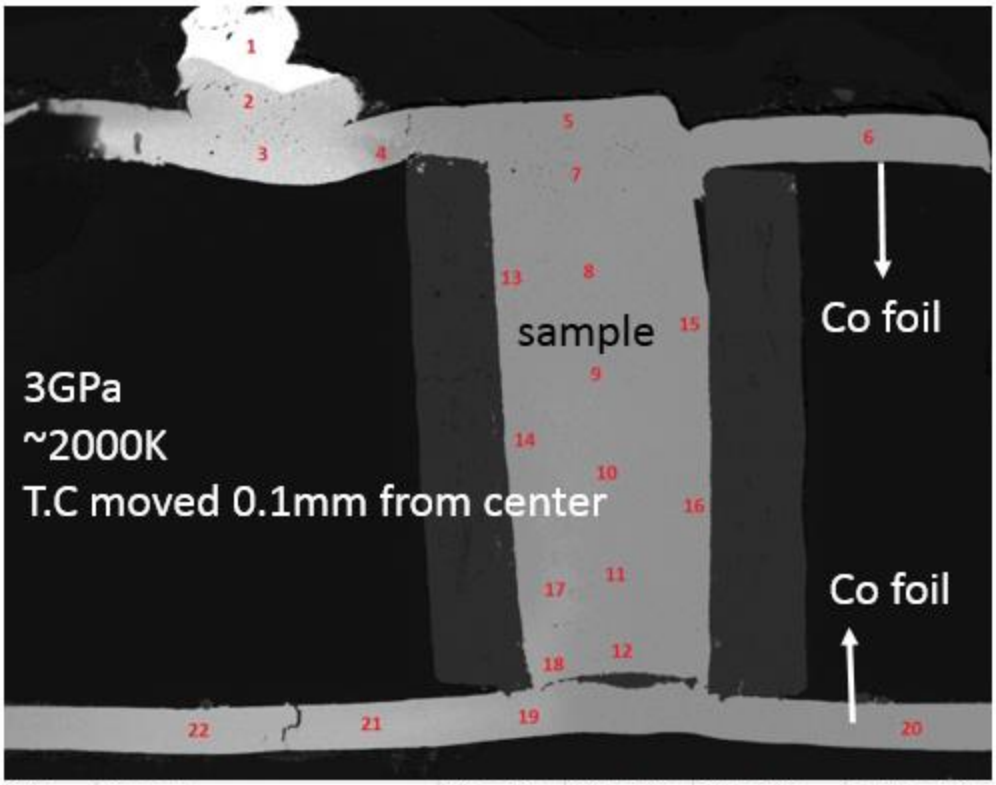

Point	Comment	W(Mass%)	Co(Mass%)	Re(Mass%)	Total(Mass%)
1	Co-3GPA_25-08-2016_spot_01	95.14	nd	4.032	99.172
2	Co-3GPA_25-08-2016_spot_02	29.878	59.538	10.083	99.499
3	Co-3GPA_25-08-2016_spot_03	29.723	57.843	10.994	98.56
4	Co-3GPA_25-08-2016_spot_04	5.937	92.588	0.536	99.061
5	Co-3GPA_25-08-2016_spot_05	0.05	98.569	nd	98.619
6	Co-3GPA_25-08-2016_spot_06	nd	99.347	nd	99.347
7	Co-3GPA_25-08-2016_spot_07	0.121	98.827	0.009	98.957
8	Co-3GPA_25-08-2016_spot_08	0.572	98.302	0.2	99.074
9	Co-3GPA_25-08-2016_spot_09	0.252	98.886	0.107	99.245
10	Co-3GPA_25-08-2016_spot_10	2.99	94.11	1.742	98.842
11	Co-3GPA_25-08-2016_spot_11	1.15	97.655	0.076	98.881
12	Co-3GPA_25-08-2016_spot_12	0.354	98.217	0.218	98.789
13	Co-3GPA_25-08-2016_spot_13	0.497	98.001	0.203	98.701
14	Co-3GPA_25-08-2016_spot_14	0.023	98.69	0.012	98.725
15	Co-3GPA_25-08-2016_spot_15	0.086	98.926	0.011	99.023
16	Co-3GPA_25-08-2016_spot_16	nd	98.352	nd	98.352
17	Co-3GPA_25-08-2016_spot_17	2.508	94.825	1.265	98.598
18	Co-3GPA_25-08-2016_spot_18	5.519	90.583	2.646	98.748
19	Co-3GPA_25-08-2016_spot_19	7.723	86.713	3.787	98.223
20	Co-3GPA_25-08-2016_spot_20	nd	98.857	0.013	98.87
21	Co-3GPA_25-08-2016_spot_21	18.323	77.123	3.707	99.153
22	Co-3GPA_25-08-2016_spot_22	13.609	79.813	6.409	99.831

A2.7. Back scattered electron images of recovered Co at 3GPa and ~2000K, alongside tabulated microprobe results. T.C is located 0.1mm away from the center above the top end of the sample.

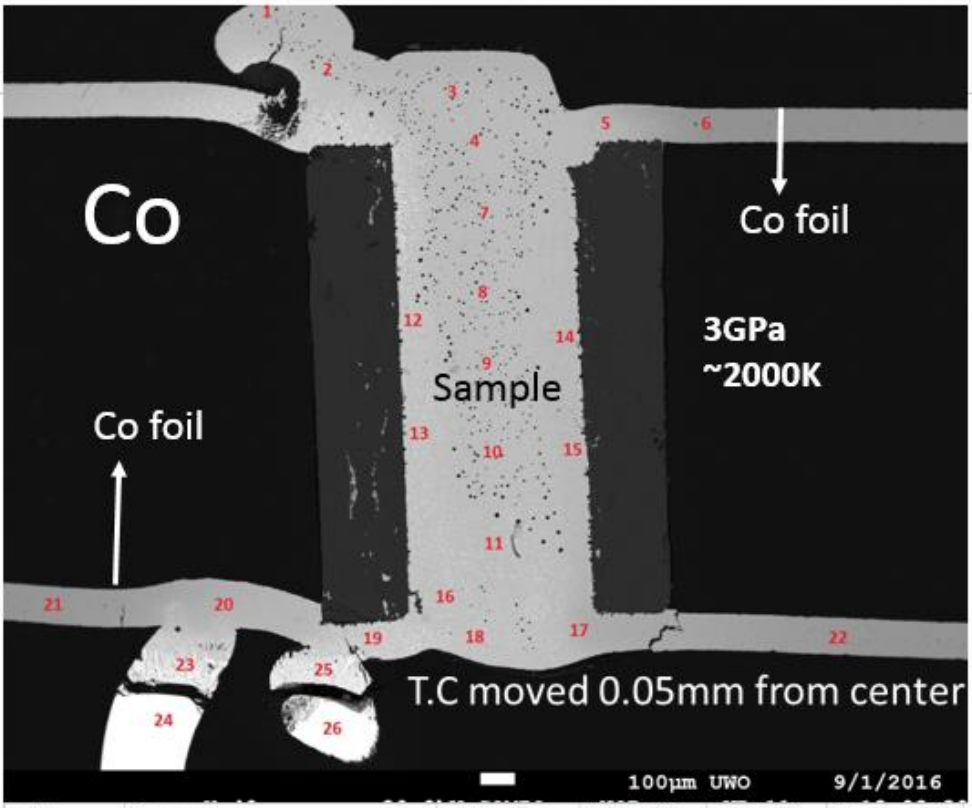

Point	Comment	W(Mass%)	Co(Mass%)	Re(Mass%)	Total(Mass%)
1	Co-3GPA_29-08-2016_spot_01	20.686	73.735	3.894	98.315
2	Co-3GPA_29-08-2016_spot_02	25.659	69.534	3.657	98.85
3	Co-3GPA_29-08-2016_spot_03	22.152	71.639	5.276	99.067
4	Co-3GPA_29-08-2016_spot_04	26.905	68.294	3.707	98.906
5	Co-3GPA_29-08-2016_spot_05	20.797	73.087	5.282	99.166
6	Co-3GPA_29-08-2016_spot_06	1.865	96.479	0.375	98.719
7	Co-3GPA_29-08-2016_spot_07	24.607	69.238	4.696	98.541
8	Co-3GPA_29-08-2016_spot_08	23.541	70.026	5.784	99.351
9	Co-3GPA_29-08-2016_spot_09	24.644	68.26	6.174	99.078
10	Co-3GPA_29-08-2016_spot_10	24.72	68.024	6.216	98.96
11	Co-3GPA_29-08-2016_spot_11	24.396	68.208	5.999	98.603
12	Co-3GPA_29-08-2016_spot_12	30.079	63.151	5.953	99.183
13	Co-3GPA_29-08-2016_spot_13	31.74	62.544	4.689	98.973
14	Co-3GPA_29-08-2016_spot_14	22.286	70.337	6.006	98.629
15	Co-3GPA_29-08-2016_spot_15	21.759	71.772	5.621	99.152
16	Co-3GPA_29-08-2016_spot_16	28.517	64.231	5.693	98.441
17	Co-3GPA_29-08-2016_spot_17	19.477	76.972	2.391	98.84
18	Co-3GPA_29-08-2016_spot_18	35.68	58.733	4.572	98.985
19	Co-3GPA_29-08-2016_spot_19	49.26	46.702	3.219	99.181
20	Co-3GPA_29-08-2016_spot_20	14.687	79.223	4.491	98.401
21	Co-3GPA_29-08-2016_spot_21	2.798	94.974	1.072	98.844
22	Co-3GPA_29-08-2016_spot_22	3.195	94.717	1.06	98.972
23	Co-3GPA_29-08-2016_spot_23	51.247	27.107	21.093	99.447
24	Co-3GPA_29-08-2016_spot_24	75.401	nd	23.891	99.292
25	Co-3GPA_29-08-2016_spot_25	62.633	28.808	7.513	98.954
26	Co-3GPA_29-08-2016_spot_26	94.785	0.002	3.973	98.76

A2.8. Back scattered electron image of recovered Co at 3GPa and ~2000K, alongside tabulated microprobe results. T.C is located 0.05mm away from the center above the top end of the sampl

Innocent Chinwe Ezenwa

Education and Qualifications

University of Western Ontario, Canada June, 2017
PhD Geophysics
(Thesis: Investigating Invariance in Electrical Resistivity of Cu, Zn and Co: Implication for the Heat Flux in Earth's Core)

University of Western Ontario, Canada 2011
MSc Geophysics
(Thesis: Design of Data Acquisition, Analysis and Visualization Software, LabVIEW: Application for High Pressure and Temperature Experiments)

University of Plymouth, United Kingdom 2008
MSc Network System Engineering
(Thesis: Budget Satellite Link Analysis Design and Implementation)

University of Nigeria Nsukka, Nigeria 2004
Bsc Hon Physics and Astronomy
Nig Sat1 Design and implementation: A Review Study

Journal Publications

Ezenwa, I .C, Secco R.A and Wenjun Yong (2017). Electrical Resistivity Measurements of Solid and Liquid Cu up to 5 GPa: Decrease Along the Melting Boundary *(to be submitted to Journal of Condensed Matter Physics)*

Ezenwa, I .C and Secco R.A. (2017) Constant Electrical Resistivity of Zn on the Pressure Dependent Melting Boundary *(to be submitted to Journal of Applied Physics)*

Ezenwa, I .C, Secco R.A and Wenjun Yong (2017) Invariance of the Electrical Resistivity of Co along the Pressure Dependent Melting Boundary *(to be submitted to Earth and Planetary Science Letters)*

Ezenwa, I .C and Secco R.A. (2017) Electronic Transition in Solid Nb at High Pressure and Temperature *(to be submitted to Journal of Applied Physics)*

Conference Abstracts and Poster Presentations

I.C Ezenwa, R.A Secco and W.Yong, (2016) Electrical Resistivity of Solid and Liquid Zn along their Pressure Dependent Melting Boundary, American Geophysical Union Meeting, San Francisco, CA, Dec 12-16, 2016

R.A Secco, **I.C Ezenwa**, R.E Sukara, J.A.H Littleton and W.Yong (2016) Is the Electrical Resistivity Constant on the Pressure Dependent Melting Boundary. Eur. High Pressure Res. Grp Mtg, Sept 4-9, 2016, Bayreuth, Germany

R.A Secco, **I.C Ezenwa**, R.E Sukara, J.A.H. Littleton and W.Yong (2016) Resistivity of Liquid Transition Metals on the Pressure Dependent melting Boundary. *COMPRES Ann. Mtg, Santa Fe, NM, June 19-23, 2016*

I.C Ezenwa and R.A Secco, (2015) Investigating the Possibility of Invariance in Electrical Resistivity in Transition Metals along their Pressure Dependent Melting Boundary. American Geophysical Union Mtg, May 2-7, 2015, Montreal, Canada.

R.A Secco, W.Yong, S.Kiarasi and **I.Ezenwa** (2013) Large Volume High Pressure Facilities at Western, Can. Geophys. Union Mtg, Saskatoon, SK , May 25-30,2013

Relevant Work Experience

Teaching and Research Assistant (University of Western Ontario).
Course presentation and lab sessions (ES1023a Planet Earth: Shaken and Stirred; ES2123b The Dynamic Earth).

ClearView Geophysics Inc. (Field Geophysicist), Canada
Running pole-dipole IP, Magnetic and Bore-hole IP survey lines: Northern Canada

Awards

The Canadian Exploration Geophysical Society (KEGS) award: $750 for each of 2011 and 2012